Towards measurement of the $W \to \tau\nu$ cross section at $\sqrt{s} = 7$ TeV using the ATLAS detector

Zhaoxia Meng

School of Physics

Shandong University

A thesis submitted for the degree of

Philosophy Doctor (PhD)

2011 May

1. Reviewer: Anonymous

2. Reviewer: Anonymous

Day of the defense: May 28^{th}, 2011

Abstract

The discovery of the neutron and the nuclear model based on the Rutherford scattering experiment leads to the conclusion that matter is constituted with fundamental particles. It was thought initially that they were only nucleus and electrons. However, with the development of particle accelerators, the fundamental structure of the matter is being explored through higher and higher energy particle beams. Now we know that the matter we know is composed of 28 elementary particles (including particles and anti-particles) interacting with each others through four fundamental forces. On the other hand, many theoretical models were established to explain the universe according to the experimental results. The standard model (SM) is found to be the most mature theory as it explains how the elementary particles interact with each others. However, it also has predicted the Higgs boson which has yet to be discovered.

The Large Hadron Collider (LHC) has been built at the European laboratory for particle physics (CERN) with the aim of searching the SM Higgs boson, as well as new particles that might manifest itself. It is designed to collide proton-proton (p-p) at a center-of-mass energy of $\sqrt{s} = 14$ TeV, with a peak instantaneous luminosity of 10^{34} cm^{-2}s^{-1}. A Toroidal LHC ApparatuS (ATLAS) is one of the general purpose experiments designed for the LHC. It detects particles produced in p-p collisions and would be able to detect any new ones which were not found by previous experiments. It is composed of several sub-detectors including trackers used to reconstruct the tracks of charged particles, calorimeters used to measure the energies of the particles and finally muon chambers used to detect muons and measure their momentum.

One of the interesting particles described by the SM is the tau (τ) lepton. Its physical properties (mass, lifetime, decays, etc.) allow it to be part of many processes within or beyond the predictions of the SM. For example, the SM Higgs boson decays to $\tau^+\tau^-$ final states with branching ratio significant enough to make this channel primordial for a discovery within the mass range 115 < m_H <140 GeV. However, the challenge at the hadron collider is the background understanding and measurement, which is the first and indispensable work to discover any new particle. Especially for the channel with the τ lepton decaying hadronically, the signal suffer from overwhelming background from QCD multi-jets which has the largest production cross section in p-p collisions at the LHC. Therefore, understanding the performance of τ lepton reconstruction and identification is essential for all the channels related to τ leptons. To understand its performance, selecting pure signal samples is important. One of the largest sources of τ leptons is $W \rightarrow \tau\nu$ process. So getting the $W \rightarrow \tau\nu$ signal and measuring its cross section is an essential issue.

The aim of this thesis is to cover some of the topics related to the ATLAS detector performance as well as studies of τ lepton identification and its first application to the $W \rightarrow \tau\nu$ cross section measurement.

After a brief introduction in chapter 1, the SM of elementary particles is described in chapter 2, as well as the theoretical motivation behind the interests in τ lepton final states physics.

Chapter 3 describes the LHC and the ATLAS detector with performance of the liquid argon calorimeter (LAr) as it is an important part of the calorimeter system. It consists of the electromagnetic calorimeter (EM), the end-caps of hadron calorimeter (HEC) and forward calorimeter (FCAL). The LAr calorimeter plays a crucial role in hadronic τ decay identification as it measures some of the physical quantities, combined with the tracking information, provide a powerful tool in separating its signal (i.e. τ lepton) from QCD jet background (see chapter 5). Several studies using the collected data from cosmic rays, 900 GeV and p-p 7 TeV collisions have shown good LAr calorimeter performance that is in accordance with expectations in order to achieve the optimal measurements necessary to physics studies of complicated processes such as $W \to \tau\nu$.

Chapter 4 shows the calorimeter response and energy resolution to pions using data collected during the 2004 test beam. During these tests a segment of the full ATLAS calorimeter system, as well as other sub-detectors, has been studied in order to understand its performance in a more realistic environment. First, random trigger has been used to measure the electronic noise for each cell of the calorimeter segment. The results show that the average noise is 12 MeV in the presampler, 12 MeV in the first layer, 28 MeV in the second layer and 22 MeV in the third layer of the LAr calorimeter, 30 MeV in the first layer, 30 MeV in the second layer and 25 MeV in the third layer of the tile calorimeter. Low energy (injection beam momentum < 10 GeV) and high energy ((injection beam momentum < 20 GeV) pion beams have been used to measure the LAr calorimeter response and resolution, as well as its dependance on beam energy and the position with respect to the incoming particles (η dependence). The LAr calorimeter cell-time to trigger-time (timing) has been estimated with the requirement that the cell energy is higher than 2.5 GeV and has been proved to be within 5 ns for good runs. The results have shown that the calorimeter response increases with the pion energy and is slightly dependent on the η position of the incoming pions. The energy resolution has also been studied and found to be linear with respect to $\frac{1}{\sqrt{E_{beam}}}$, which is in agreement with the assumption that it is dominated by fluctuations inherent in the development of electromagnetic and hadronic showers.

Chapter 5 describes the hadronically decaying τ lepton reconstruction and identification performance in the 900 GeV and 7 TeV collision data. This is achieved by comparing and optimizing the reconstruction algorithms using Monte Carlo (MC) events from hadronically decaying τ lepton final states ($W \to \tau\nu$) as well as background processes such as QCD multi-jets. Distributions of the variables used in the identification methods show good consistency between data and MC, and provide a good separation between hadronic decay τ lepton from QCD jets. Three identification methods are developed and studied with data and MC events: the cut-based method, boosted decision tree (BDT) and likelihood (LLH) method. The cut-based method gives an identification efficiencies about 70% for loose level, 50% for medium level and 30% for tight level. These three levels of identification have been defined according to acceptable background contribution for different physics analysis. The BDT and LLH method give higher efficiencies compared to the cut-based one.

Chapter 6 presents the selection of $W \to \tau\nu$ signal events, where the τ lepton decays haronically and the methods to estimated the cross section of this process at the LHC. This analysis shows the performance of the track-based missing transverse momentum (p_T^{miss}) and the use of its correlation to the calorimeter-based missing transverse energy (E_T^{miss}) in order to reject QCD multi-jets background. For signal events, where there are neutrinos in the final states, produce a real E_T^{miss} while QCD multi-jets background events have an E_T^{miss} mainly from mis-measurements of jets energy. Therefore, independent measurements from calorimeters (E_T^{miss}) and trackers (p_T^{miss}) are strong correlated for the signal events. Using this property, 60% of QCD multi-jets background events can be rejected. A new quantity, called missing energy significance ($S_{E_T^{miss}}^{new}$) has been defined and used for suppressing QCD multi-jets background as well as estimating its contamination to the selected signal events directly from data. $S_{E_T^{miss}}^{new}$ is defined as $\frac{E_T^{miss}[GeV]}{(0.5 \cdot \sqrt{\sum p_T[GeV]})}$, where $\sum p_T$ is the total transverse momentum of the event measured from all reconstructed good quality tracks from the primary vertex. $S_{E_T^{miss}}^{new}$ has proved to be less sensitive to pile-up events when the LHC instantaneous luminosity increases and hence shows more stable measurements of the $W \to \tau\nu$ cross section. This is due to the fact that $\sum p_T$ from one vertex is not effected by others vertices. In the analysis, 1545 ± 76 (stat) signal events are selected with an estimated QCD multi-jets background events of 642 ± 45 (stat). Based on these numbers, a very preliminary measurement of the cross section ($W \to \tau\nu \to \tau_{had}\nu$) 5.96 ± 0.26 nb is obtained with statistic uncertainty shown only.

Contents

List of Figures

List of Tables

Glossary

GeV	An energy unit in the natural unit system, equal to 10^9 eV
TeV	An energy unit in the natural unit system, equal to 10^{12} eV
ns	A time unit, equal to 10^{-9} s
QCD	Quantum chromodynamics, a theory describing the strong interaction which is one of the four fundamental interactions occurring between quarks and gluons
b	Barn, an area unit, denotes a cross section of a process in particle physics. Usually used sub-units include femtobarn (fb, 10^{-15} b), picobarn(pb, 10^{-12} b), nanobarn (nb, 10^{-9} b), microbarn (μb, 10^{-6} b) and millibarn (mb, 10^{-3} b)
TDAQ	The ATLAS Trigger and Data Acquisition System
COOL	A kind of conditions data storage tool
EW	Electroweak

1

Introduction

τ lepton (usually denoted as τ^-) is one of the third generation leptonic particles, with negative electric charge and spin 1/2. Along with its corresponding neutrino (ν_τ), the other two generations of leptons and three generations of quarks, as well as four force media particles, elementary particles discovered until now are composed. Leptons and quarks with spin 1/2 are fermions while the force media particles with spin 1 are known as bosons. All charged fermions have their corresponding anti-particles in SM with opposite charge sign but the same mass and spin. The four bosons are gluon, γ, W and Z. Gluon propagates strong interaction between quarks and itself, γ transits electromagnetic interaction between charged particles and W/Z bosons mediate weak interaction between fermions.

τ is the heaviest lepton and the only one that can decay into hadrons through weak interaction. The main source of τ leptons in high energy hadron colliders is from electroweak interaction, i.e. W/Z decay and Drell-Yan process. Because of its relatively high mass comparing to its brothers e and μ, it is expected to have larger coupling to heavy particles. τ lepton is pursued by theorists especially in the supersymmetry (SUSY) theory. Even in the SM, the only undiscovered particle, Higgs boson, has a relatively high decay branching ratio to a τ-pair ($\tau^+\tau^-$) in low mass region, where τ^+ is τ^-'s anti-particle (anti-tau) [1].

W boson can be produced in particle collisions when the center-of-mass energy is high enough. Due to its short lifetime, the W boson decays almost immediately into leptons and quarks. W boson includes W^+ and W^- taking a unit positive and negative

[1]In this paper, τ denotes τ^- and τ^+ leptons without specific explanation.

electric charge, respectively [1]. It can decay into two quarks (hadronic decay modes) or two leptons (leptonic decay modes). In the leptonic decay modes, one charged lepton and the same generation neutrino must be produced at the same time because of the lepton number conservation. W^+ decays into charged anti-lepton and neutrino, while W^- decays into charged lepton and anti-neutrino. In the SM, the branching ratios of $W \to e\nu$, $W \to \mu\nu$ and $W \to \tau\nu$ are the same, which is around 11% [1].

ATLAS [2] is one of the general purpose detectors at the LHC [3, 4] at CERN. The main objectives of the experiment are to hunt for the Higgs boson and search for the new physics. In the LHC, protons are accelerated in opposite directions and collided in several points. ATLAS detector is built on one of the points and detects the material-interacting particles produced after p-p collisions. According to the SM theory calculation, W bosons is produced with a cross section of an order of 10^3 pb at center-of-mass energy of 7 TeV that was achieve by LHC on March 30, 2010.

Even W boson and τ lepton have been discovered since many years ago and studied carefully by many other collider experiments, such as LEP [5, 6] and Tevatron [7, 8], it is still important and can not be ignored at such a high center-of-mass energy. Since $W \to \tau\nu$ process provides τ leptons with relatively high cross section at the LHC, its selection and measurement is crucial for the new particles searches related τ lepton in the final states. After selecting of the signal, the next aim is to measure its cross section. What's more, $W \to \tau\nu$ is an important background to many other processes, like $H^+ \to \tau\nu$ in Minimal Supersymmetry Standard Model (MSSM). Understanding the behavior of $W \to \tau\nu$ events would be the first step towards the new physics.

This paper describes how to select the $W \to \tau\nu$ signal against the large QCD mulitjets background, where τ lepton decays hadronically. This analysis is based on a data sample collected by ATLAS experiment with an integrated luminosity of $\sim 36.8\ pb^{-1}$. In the following chapters, we will discuss the theoretical purpose in chapter 2. Atlas detector will be described in chapter 3. In chapter 4 we are going to illustrate some ATLAS combined test beam studies on pions considering we are researching the hadronic decaying τs. In chapter 5, hadronically decaying τ reconstruction and identification will be shown. The signal selection and a preliminary cross section without full systematic studies of $W \to \tau\nu$, where τ lepton decays hadronically, will be discussed in chapter 6.

[1] In this paper, W boson denotes W^- and W^+ bosons without specific explanation.

2

Theoretical motivation

Particle physics is to understand what is the world, how the world is formed. Through experiments, we know we have 28 elementary particles and antiparticles that, through 4 different interactions, constitute the material we can see and we cannot see directly by eye. Theoretical models are established to describe the interactions between elementary particles. SM is the model correct examined by experiments, but it still has problems such as CP violation [20] and neutrino oscillations [21]. In the model, 1 yet discovered Higgs boson is important for people to understand where the mass of particles come from. The LHC accelerator and its experiments is constructed to search for the Higgs and new physics.

The LHC and its experiments are very large and complex that many detailed work need to be done before we can achieve our final purposes, including cross section measurements for the well known particles which are important for understanding new phenomena at a new experiment.

$W \to \tau\nu$ process is well known since experiences have been gained from previous colliders, like Tevatron at Fermilab in USA [18]. However, with different type of particles collision at LHC (proton-proton collision, while previous are proton-antiproton or e^+e^- collision) and unprecedented high energy, $W \to \tau\nu$ need to be measured again. Also, $W \to \tau\nu$ is an important background to new processes that are the final purposes of constructing LHC and ATLAS. Besides, precise measurement of its cross section will prove or reject the lepton universality theory in SM [19]. τ is important at ATLAS because of its strong coupling to many new particles beyond the SM. Therefore, tuning τ performance is necessary and the tune through $W \to \tau\nu$ process is a main means.

2.1 Theoretical models

To explain the phenomena we found in experiments and understand the problems we have not solved yet, different physics models are constructed. The physics modes aim to have a fundamental frame that all the phenomena can be explained by being treated in specific cases, like the momentum in the classic physics is the special case (limit) of the theory of relativity when the velocity of the object is much smaller than the light speed. At present, SM, whose formulation was finalized in the middle of 1970s, explains almost all the particle experiments results except several phenomena, such as the CP violation [20] and neutrino oscillations [21]. At the same time, theorists construct many other models to address fundamental problems within the SM.

2.1.1 Standard model

SM is a theory describing the interactions between elementary particles. It is a model based on quantum field theory that describes the behavior of particles. In this section, briefly description of the SM is shown.

2.1.1.1 Elementary particles and fundamental interactions

Elementary particles involved in the model are all the ones discovered until present and the one predicted but not been found yet (Higgs boson). The discovered elementary particles include 12 fermions and 12 corresponding anti-fermions, which take spin $\frac{1}{2}$, and 4 gauge bosons, which take spin 1 [23]. Each elementary particle owns a unique flavor that defines this kind of particle.

Interactions (also called forces due to history) are defined as the manners of one particle affecting the other particle. Four fundamental interactions are found until now: electromagnetic, weak, strong and gravitation, where electromagnetic and weak are unified together to be treated as one interaction: electroweak. In the SM only electroweak and strong interactions are involved. **Electromagnetic** interaction happens between particles carrying electrical charge. It is a kind of bidirectional force that particles taking the same sign of the electrical charge repel each other, while they attach each other when electrical charge signs are different. It not only occurs between elementary particles but also between materials taking electrical charges that are because the charges taking by the elementary particles not neutralized. It is a long distance interaction that it can happen between particles with infinite distance, but the strength decreases with square of the distance. **Weak** interaction happens between particles taking weak isospin which can be understood similarly as the electrical charge. Weak interaction changes particles' flavor. It is the shortest distance interaction happening within 10^{-18} m. Decay is always weak interaction because flavors of the interacting particles are changed. **Strong** interaction happens between particles taking so-called color charge. It is a short distance interaction occurs within 10^{-15} m. **Gravitation** is not described by the SM. It is a long distance interaction happens between particles or materials carrying mass. Similar as electromagnetic interaction, its strength decreases with square of the distance until infinite distance.

- **Fermions and anti-fermions** taking fractional intrinsic spins obey Pauli exclusion principle. For simple, fermions will be illustrated detailed while the anti-fermions are known as behaving the same only with opposite electrical charge values. The fermions are categorized according to what kinds of interactions they can participate. The fermions being able to participate strong interaction are called quarks, while the others are called leptons.

  Quarks are found to take fractional electrical charge with three of them taking $\frac{2}{3}$ being called up-type quarks and the other three taking $-\frac{1}{3}$ being called down-type quarks. The six quarks are up, charm, top, down, strange and bottom quarks, where the former three quarks are up-type and the latter three are down-type.

  Leptons take integer electrical charge with three of them take electrical charge - 1 and the other three take no electrical charge (i.e. 0). They include electron (e), muon (μ) and tau (τ), and their corresponding neutrinos called electron-neutrino (ν_e), muon-neutrino (ν_μ) and tau-neutrino (ν_τ). Traditionally, neutrinos are defined as up-type leptons and charged leptons are down-type. In the SM, all the three neutrinos are expected to be mass less while actually neutrinos oscillations found in experiments that denote neutrinos take mass.

  These fermions are divided into three generations (or called families), that particles in higher generations can decay to particles in lower generations while within one generation the decay occurs rarely. Therefore, materials in the world are constituted of the particles in the lowest generation except the neutrinos that interact with nuclear material with very tiny cross section. One generation contains one up-type quark, one down-type quark, one up-type lepton and one down-type lepton, which particles in higher generation is massive than the corresponding particle in the lower generation. It is known as the hierarchy problem. Figure 2.1, which is a famous table, shows the quantum numbers of the elementary particles.

What kinds of interactions that the fermions can participate are determined by what kinds of charges they are taking. Quarks take charge so-called color so that they can take part in the strong interaction. The color charges are defined as red (R), green (G) and blue (B), where the colors are not the ones in the traditional concept. Besides the color charge, quarks are taking electrical charge and weak isospin that they can be involved into electromagnetic and weak interactions. Charged leptons carry electrical charge and weak spin. Therefore they are able to participate electromagnetic and weak interactions. Neutrinos do not carry electrical charge that they only take part in the weak interaction. Leptons do not take color charge, so they never appear in the strong interaction.

- **The four bosons** in the SM are photon, $W^{\pm}$, Z and gluon with intrinsic spin 1 and are not constrained by the Pauli exclusion principle. They are known as the mediate particles of the interactions.

  Photon is the media particle of the electromagnetic interaction. Once the electromagnetic interaction happens, a photon must be propagated between the interacting particles. The propagated photons can be on-shell that obey the energy-momentum relation as shown in equation 2.1 or off-shell that the mass of the propagated particle is arbitrary and not constrained by the energy-momentum relation.

$$E^2 - p^2/c^2 = m^2c^2 \tag{2.1}$$

where E, p, m and c are the energy, momentum, mass of the particle and the light speed.

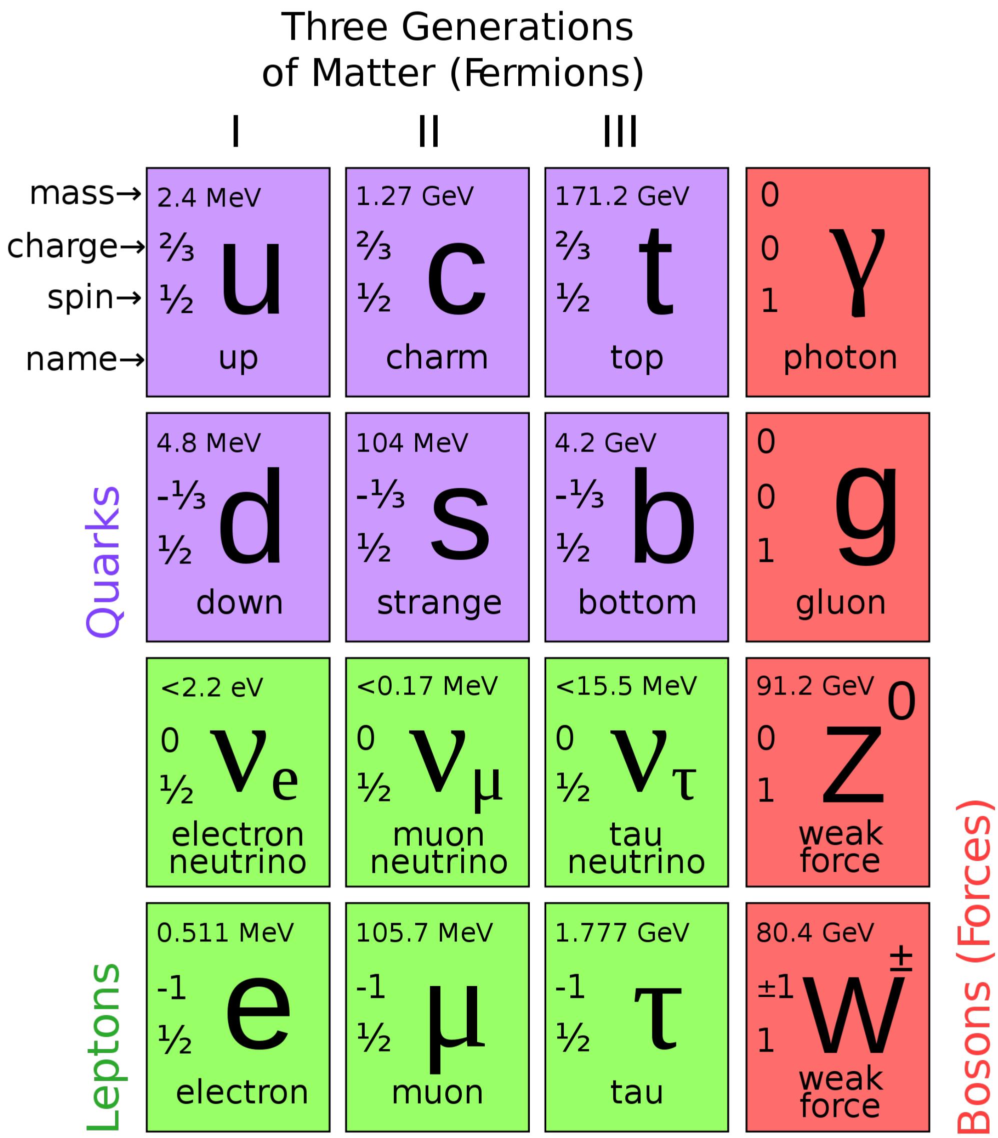

Figure 2.1: Elementary particles in the SM with their corresponding quantum numbers.

$W^{\pm}$ and Z are media particles of the weak interaction. Weak interaction changes particles flavor that the outgoing particles are different from the incoming particles not only on the 4-momentum but also the type, e.g. τ lepton decays to electron and two neutrinos.

Gluon mediates strong interactions [25] by combining the color charges carried by the interacting particles and gluon itself. Gluons' color charges are expected to combine two of color charges from red, green, blue, anti-red ($\bar{R}$), anti-green ($\bar{G}$) and anti-blue ($\bar{B}$) without making the charge cancelled each other, i.e. gluons do not take color $R\bar{R}$, $G\bar{G}$ and $B\bar{B}$. Since gluon carries color charge as well, strong interaction happens among gluons without quarks participation. The color charge is conserved in the strong interaction. Quarks and gluons cannot be detected directly by the detector since the strong force strength is proportional to the square of the distance between the two interacting particles that all the quarks and gluons are constrained in a small space, which is called "quark confinement". The particles being composed of quarks like proton and neutron are colorless that we call them white color particles. Actually, the quantum numbers of the proton and neutron that constitute the nuclear are determined by the so-called valence quarks, while gluons constrained in the proton or neutron split into to quarks forming the "sea quarks". The "sea quarks" are not stable as the valence quarks, but they maybe excited when the collision energy between quarks or neutrons are large enough. The strong interaction are described by a theory so-called Quantum ChromoDynamics (QCD) based on the perturbation theory.

A convenience tool, Feynman diagram, is used to make the interactions presented visually. Figure 2.2 shows an example of the production of W boson in proton-proton collision with the first order in the perturbation theory, then the W decays into τ and tau-neutrino. Since protons are accelerated to a very high energy that they are broken when the collisions happen and the interactions happen between quarks or gluons in the protons.

- **Higgs boson** is the only particle predicted by the SM but not discovered yet. It is a scalar boson with intrinsic spin 0 [26, 27, 28, 29, 30].

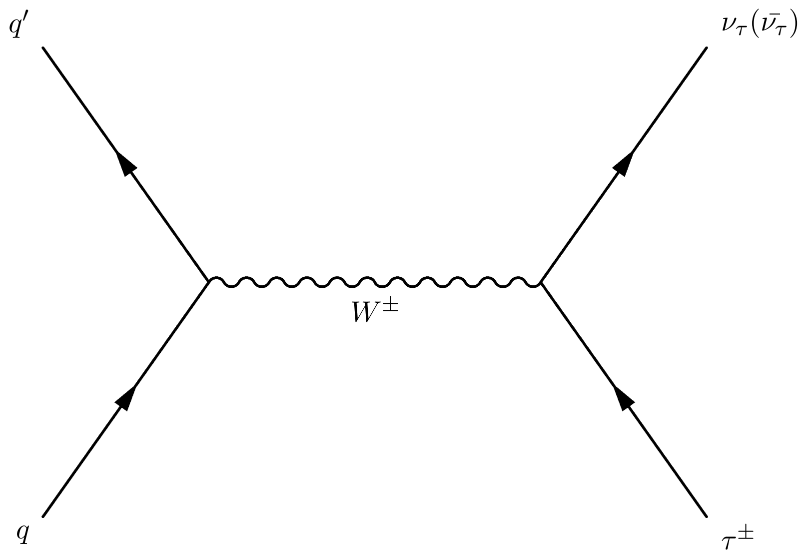

Figure 2.2: Feynman diagram for production of W bosons in proton-proton collision, where W decays to τ and tau-neutrino.

2.1.1.2 Mathematical form of the SM

SM is a theory about interactions between elementary particles. First, it is a gauge field theory using symmetry groups to describe the interactions in terms of mathematics. To be simple, SM describing the interactions by symmetry group $U(1) \times SU(2) \times SU(3)$ [24] with each group owns corresponding generators denoting the fields of the bosons. The fermions are described with vectors with each element denoting a quantum number, e.g. the momentum, energy, mass and spin, etc. One particle influencing another particle through propagating a boson described mathematically is the vector describing the status of the particle being transformed to another vector through the generators of the symmetry group. Actually, the status of the particles is the representation of the groups.

- The symmetry group U(1) represents the electromagnetic interaction which has one gauge field resulting one vector boson photon. It transfers the representations of the incoming to outgoing particles through changing the so-called hypercharge [9].

- The symmetry group SU(2) represents the weak interaction which has three gauge fields resulting three vector bosons W^+, W^- and Z. It transfers the representations of the incoming to outgoing particles through changing the so-called weak isospin.

- The symmetry group SU(3) represents the strong interaction which has eight gauge fields resulting eight gluons with eight different colors for the strong interaction mediation. It transfers the representations of the incoming and outgoing particles through changing the so-called color charge. It is found that, strong interaction exists only between quarks and gluons.

Second, it is a chiral theory by treating the two helicities of the fermions differently. The fermion chirality can be projected out from Dirac fermions with the fifth gamma matrix:

$$\psi_L = \frac{1}{2}(1 - \gamma_5)\psi \tag{2.2}$$

$$\psi_R = \frac{1}{2}(1 + \gamma_5)\psi \tag{2.3}$$

where ψ is the column matrix denoting fermions status with mostly the cases being the spin status that is called spinors, ψ_L is the left-handed fermions, ψ_R is the right-handed fermions and γ_5 is the fifth gamma matrix.

The helicity is defined as the projection of spin to the particles motion direction. If the projection direction is the same as (opposite to) the particles momentum direction, the helicity is positive (negative) or left-handed (right-handed). It is dependent on the selection of the observation frame while chirality is not. Why the left-handed fermions and right-handed fermions are treated differently is because in the weak interaction the chirality is asymmetry. The parity symmetry P breaking in the weak interaction was found in 1950s and then the CP symmetry that combines the parity and charge conjugation C was found also to be broken in 1960s. A new theory to describe the asymmetry is needed. At last, the vector minus axial vector (V-A) is utilized by assuming weak interaction only occurs on left-handed fermions (and right-handed anti-fermions). But chirality is symmetry in the electromagnetic, strong interactions and maybe gravitation.

2.1.1.3 Higgs boson

Higgs boson is introduced to explain the symmetry breaking in the electroweak interaction, and during the breaking, the vector bosons $W^{\pm}$ and Z gain the mass and fermions gain their masses by interacting with the Higgs fields.

The Lagrange is constructed for a system to describe its dynamics. As soon as we know the Lagrange of the system, we know everything including its motion. Therefore, theorists try to establish the Lagrange for the elementary particle system to describe their motion under different kinds of interactions. Based on the U(1) × SU(2) × SU(3), the Lagrange for the three fundamental interactions is:

$$\mathcal{L}_{SM} = \int -\frac{1}{4}B_{\mu\nu}B^{\mu\nu} - \frac{1}{4}trW_{\mu\nu}W^{\mu\nu} - \frac{1}{4}trG_{\mu\nu}G^{\mu\nu} \tag{2.4}$$

where $\mathcal{L}_{SM}$ is the notion of the Lagrange for SM, $B_{\mu\nu}$ and $B^{\mu\nu}$ are the elements of gauge field U(1), $W_{\mu\nu}$ and $W^{\mu\nu}$ are the elements of gauge field SU(2), $G_{\mu\nu}$ and $G^{\mu\nu}$ are the elements of gauge field SU(3) and trace (tr) runs over the diagonal elements of SU(2) and SU(3).

The SU(2) part of the Lagrange refers to the weak interaction where CP symmetry violation was found. The Higgs gauge group is SU(2) with U(1) of charge -1 and the field is the complex vector spinor:

$$\varphi = \frac{1}{\sqrt{2}}\begin{pmatrix} \varphi^{+} \\ \varphi^{0} \end{pmatrix} \tag{2.5}$$

where φ is the Higgs field and φ^{+} (φ^{0}) is the component of the field with positive (0) electrical charge.

Its Lagrange is written as:

$$\mathcal{L}_{H} = |\partial_{\mu} + \frac{i}{2}(g'Y_{W}B_{\mu} + g\vec{\tau}\vec{W}_{\mu})|^{2} - \frac{\lambda^{2}}{4}(\varphi^{\dagger}\varphi - v^{2})^{2} \tag{2.6}$$

where $\mathcal{L}_{H}$ is the notion of the Lagrange of Higgs field, g' is the electromagnetic coupling, g is the weak coupling, λ is the Higgs boson coupling strength and v is the vacuum expectation value that is non-vanishing and gives mass to bosons by setting $\varphi^{+} = 0$ and φ^{0} real quantity.

The $W^{\pm}$ and Z bosons masses are predicted as:

$$M_W = \frac{v|g|}{2} \tag{2.7}$$

$$M_Z = \frac{v\sqrt{g^2 + g'^2}}{2} \tag{2.8}$$

where M_W and M_Z has been measured with experiments, g and g' will be determined after the Higgs boson is found and the mass of the Higgs boson is measured.

2.1.2 Beyond the standard model

Although the SM has been extensively tested by experiments, there are still some fundamental problems within the model. For example,

- Originally, SM predicts neutrinos to be massless. However, experimental results show this not be the case [21, 22]. Even the SM can be modified to accommodate this observation, the changes are not natural.
- The SM cannot explain the hierarchy problem found in experiments.
- The gravitation is not involved in the model and the dark matter and dark energy in the cosmological experiments cannot be explained.

Based on this, theorists try to establish other models by extending the SM or constructing non-Higgs models. The most popular extension is the Minimal Supersymmetric SM (MSSM) [13]. In this extension, two Higgs doublets with five particle states are predicted. The five particle states include three neutral Higgs bosons (denoted as h, H and A) and two charged Higgs bosons (denoted as $H^{\pm}$) [16]. The three neutral Higgs bosons contain two CP-even (h and H) and one CP-odd (A) states [10]. Their masses are correlated to the ratio of the Higgs vacuum expectation values (denoted as $tan(\beta)$). At tree level radiative corrections, the five Higgs bosons masses follow the order: $m_h < (M_Z, m_A) < m_H$ and $M_{W^{\pm}} < m_{H^{\pm}}$ [11]. Some of these Higgs bosons are expected to couple to τ lepton with a non-negligible branching ratio under some conditions [12, 14], e.g. at large $tan(\beta)$ value (= 40) [12], the branching ratio of h to $\tau^{\pm}$ pair is $\sim 10\%$.

2.2 W boson

The W boson is predicted in the SM and was first discovered in 1983. It has been studied by several experiments after its discovery, including the mass and branching ratios to different final states, etc. The W boson decays through electroweak interaction. It can decay into a lepton and a neutrino with the same flavor, and can also decay into a pair of up- and a down-type quarks. The branching ratios of W decay obtained from other experiments are listed in table 2.1. Only W^+ decay modes are shown in the table. W^- has the same decay modes but with the products of their charge conjugated.

The challenge of the W boson studies at hadronic collider in the leptonic decay channels is the missing energy caused by the neutrino produced along with the charged lepton. Especially in the $W \rightarrow \tau\nu$ channel where one or two additional neutrinos produced when τ lepton decays hadronically or leptonically. The mass distribution cannot be measured directly. But the transverse mass can be measured instead. The transverse mass of W boson in the experiment is defined as [15]:

$$M_T^W = \sqrt{2p_T^l p_T^\nu (1 - \cos\varphi_{l\nu})} \tag{2.9}$$

where T denotes the transverse plane perpendicular to the collision axis, p denotes the momentum and $\varphi_{l\nu}$ is the angle between the lepton and neutrino in the transverse plane. In the language of experiment, the transverse momentum of the neutrino is replaced by the missing transverse energy measured in the detector.

The transverse mass of W boson is 80.399 ± 0.023 GeV measured by previous experiments, with the full width of the mass around 2.085 ± 0.042 GeV.

All though W boson has been studied detailed in other experiment, it is still very important at the LHC because of its large cross section (in the lepton decay modes the

Modes	Branching ratio (%)	Remarks
$W^+ \rightarrow e^+\nu$	10.75 ± 0.13	Leptonic decay modes
$W^+ \rightarrow \mu^+\nu$	10.57 ± 0.15	
$W^+ \rightarrow \tau^+\nu$	11.25 ± 0.20	
$W^+ \rightarrow qq'$	67.60 ± 0.27	Hadronic decays modes

Table 2.1: Decay modes of W^+ boson

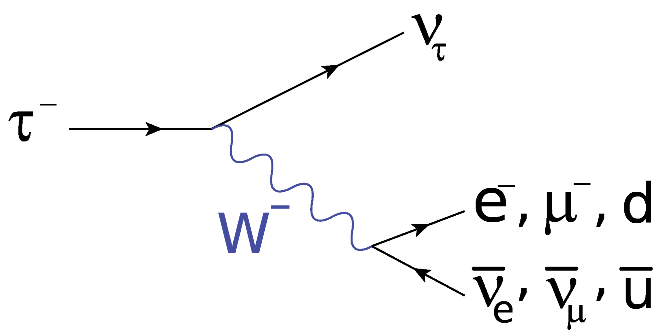

Figure 2.3: Feynman digram for the τ lepton decay, including leptonic and hadronic decay modes.

$\sigma \times BR$ is $\sim$ 10.46 np at the Next-to-Next Leading Order (NNLO) theoretical calculation [17]). It is an important background to many new particles decaying to τ final states. And its precise measurement is crucial for the τ lepton efficiency performance at ATLAS, which is important for every τ related channels.

2.3 τ lepton

τ lepton is in the third generation of the elementary particles in the SM, which is the most massive lepton being able to decay hadronically and taking electrical charge (τ^- takes negative charge, while τ^+ takes positive electrical charge). Figure 2.3 shows the τ leptonic and hadronic decay modes. Decay is weak interaction, therefore the decay modes of τ leptons are all through W boson. Because τ lepton mass is large enough ($\sim$ 1.78 GeV), it can decay into light hadrons like pions or koans.

At hadron collider, it is difficult to identify the original leptons and the ones from τ lepton decay [2, 32], therefore hadronic τ lepton decay modes are especially important. The most used decay modes and their branching ratio will be illustrated in section 5.1.

Why experiments love τ lepton even it may suffer large background from QCD jets? That is because τ lepton appears frequently in the new particles (including SM Higgs boson and other particles in the models beyond SM [31]) decay final states as in the theory prediction. As an example, figure 2.4 shows the branching ratios of the SM Higgs boson decaying to difference final states. In the low Higgs boson mass region ($<$ 140 GeV), the branching ratio into τ-pair is around 9%.

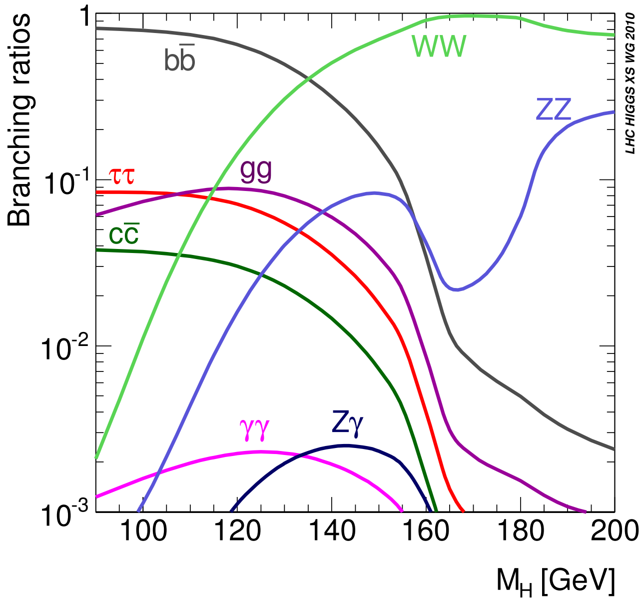

Figure 2.4: SM Higgs boson decay branching ratios to different final states, which is predicted by the theory.

3

ATLAS experiment

3.1 LHC

The LHC [3] is a large orbicular hadron collider, installed underground about 100 m with perimeter ~ 27 kilometers at the European Organization for Nuclear Research (CERN), crossing the border between France and Switzerland with a part in Switzerland near to Geneva and another part in France crossing several small towns. It is a proton-proton collider with designed center-of-mass energy 14 TeV and luminosity 10^{34} $cm^{-2}s^{-1}$. It also provides pb-pb collision with designed center-of-mass energy at 5.5 TeV and luminosity 10^{27} $cm^{-2}s^{-1}$. Six experiments are located on it to utilize the beams for collision: ATLAS [2], CMS (the Compact Muon Solenoid Experiment) [34], ALICE (A Large Ion Collider Experiment) [35], LHCb (the Large Hadronic Collider beauty experiment) [36], LHCf (the LHC forward experiment) [37] and TOTEM (Total Cross Section, Elastic Scattering and Diffraction Dissociation) [38]. Figure 3.1 shows the sketch map for LHC and six experiments.

One proton-proton beam contains 39 bunch trains with each bunch train consisting of 72 bunches. Therefore, 2808 bunches are needed to full fill the whole ring in one direction. Figure 3.2 shows the bunches scheme from Proton Synchrotron Booster (PSB) to LHC through Proton Synchrotron (PS) and Super Proton Synchrotron (SPS). It needs ~ 3 *minutes* to full fill the whole ring in LHC [3].

LHC started to provide beams since end of November in 2009. The center-of-mass energy was improved from 900 GeV in 2009 to 7 TeV since end of March in 2010. The peak instantaneous luminosity was $\sim 2.07 \times 10^{32}$ $cm^{-2}s^{-1}$. The goal for LHC in 2011

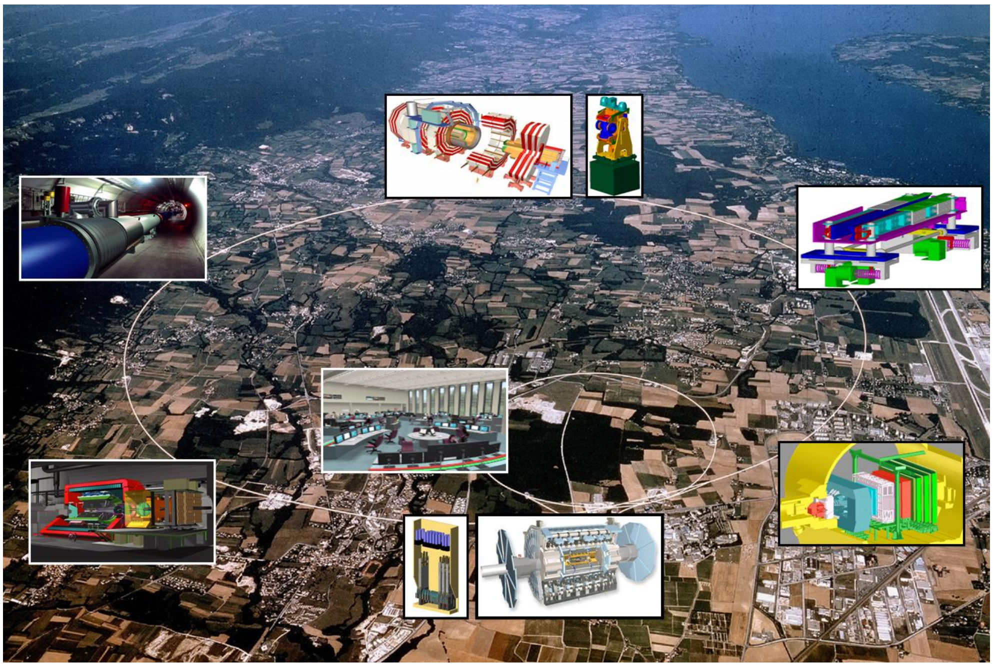

Figure 3.1: Sketch map for LHC and experiments located on it.

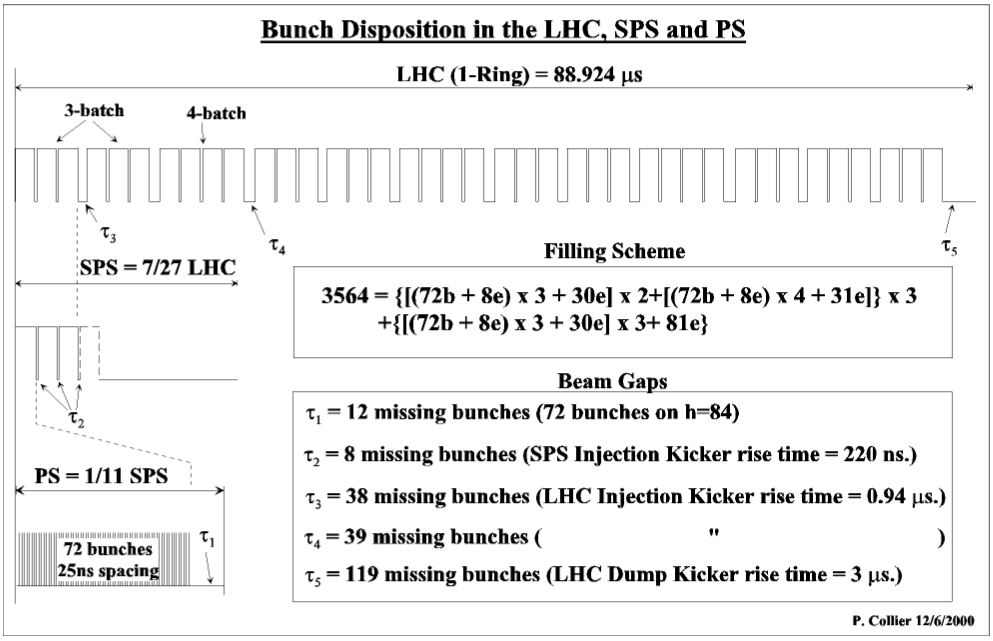

Figure 3.2: Sketch map for LHC designed bunch scheme.

is to provide 1 fb^{-1} integrated luminosity data at center-of-mass energy of 7 TeV by increasing the instantaneous luminosity stably.

3.2 ATLAS experiment

3.2.1 ATLAS overview

ATLAS [32] is a general-purpose experiment consists of several sub-detectors that are using for detecting different kinds of particles. The sub-detectors include inner detector (ID) [39], calorimeter [46] and muon spectrometer (MS). Solenoid is located between the electromagnetic calorimeter (EM calorimeter) and the inner detector to provide 2 T magnetic field for the inner detector with peak value 2.6 T inside of the solenoid, while Toroid is consists of eight air-core loops and two end-caps located inside of the muon spectrometer and outside of hadronic calorimeter, providing 4 T magnetic field for the muon spectrometer. Figure 3.3 shows the overview of the ATLAS detector. It is a cylinder taking the beam line as the center axis. The sequence of the sub-detectors installation from inner to outer is ID, solenoid, EM calorimeter, hadronic calorimeter and then toroid with muon spectrometer inside of it. All the sub detectors are divided into central and end-cap parts to get an almost full coverage of the geometry. The length of the ATLAS is 25 m from one of the most outside end-cap of muon spectrometer to the other one. The radius of the atlas detector is 11 m which is the most outer of the central part radius of the muon spectrometer. The total weight of the detector is $\sim$ 7000 tons with the calorimeters taking about 4000 tons.

The ATLAS detector is mirror symmetrical along the beam, with all the sub-detectors installed coaxially around the beam line. The ATLAS coordinate system is defined as: the origin is the center of symmetry, the *x-axis* points to the LHC center, the *y-axis* points up to sky perpendicular to *x-axis* and the *z-axis* is the beam line with positive direction pointing left when standing at the center of LHC and facing to the ATLAS detector (e.g. from west to east). The three axes of the ATLAS coordinate system obey to the right hand low. The detector is divided into A-side and C-side along *z-axis* with the origin as the demarcation point, where A-side is at the positive *z-axis* and C-side is at the negative *z-axis*. Described as spherical coordinate system: R is the distance of the point to the origin, the azimuthal angle is the angle starting from positive *x-axis* in the *x-y* plane (Rz plane) around the *z-axis* (beam line) and the

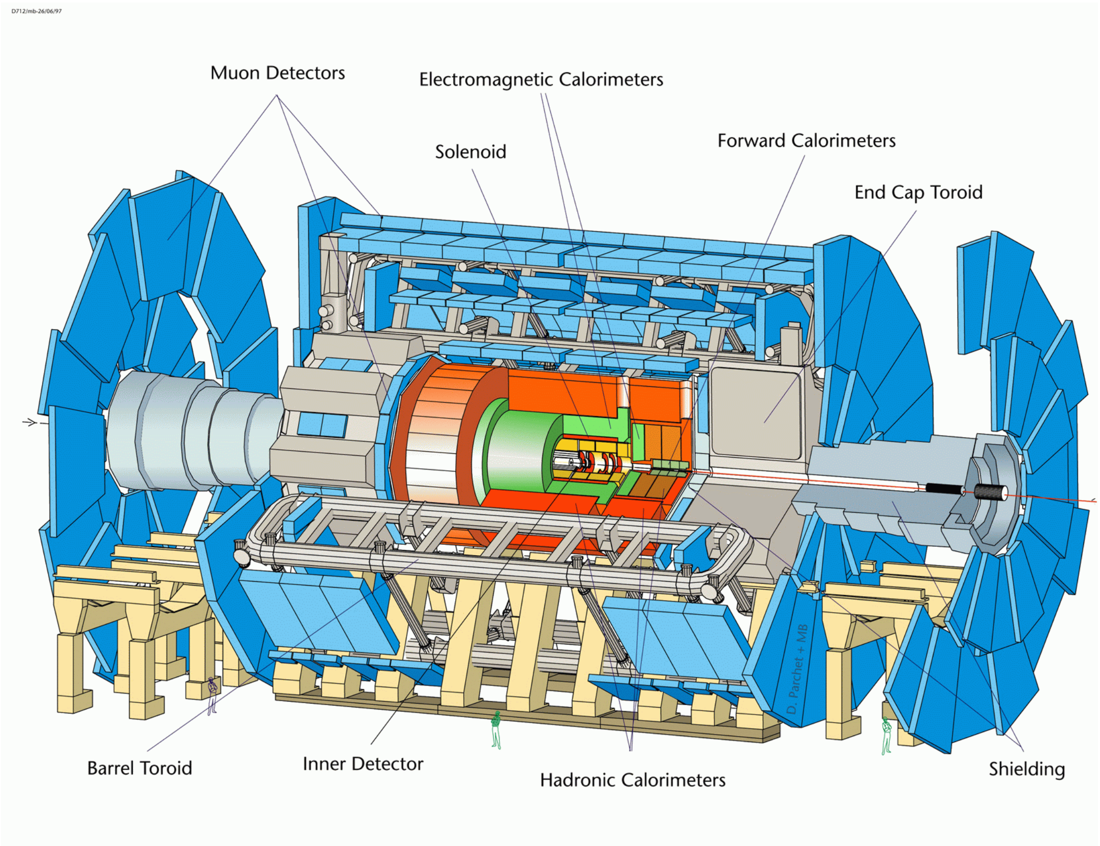

Figure 3.3: Sketch of the ATLAS detector.

polar angle starts from the positive *z-axis* in the $R\phi$ plane. Plane perpendicular to the beam line (e.g *x-y* plane or also called $R\phi$ plane) is defined as *transverse plane.* Momentum projected to transverse plane is called transverse momentum, denoted as p_T and obtained according to $\sqrt{(p_x)^2 + (p_y)^2}$ where p_x and p_y are the scalar sum of the momentum in the x and y directions, respectively. Transverse energy has the same definition as transverse momentum. For analysis convenience, pseudorapidity η is defined as:

$$\eta = -\log \tan \frac{\theta}{2}, \tag{3.1}$$

where θ is the polar angle ranging from 0 to π in the unit of radian.

Distance from an axis along R in the $\eta - \phi$ plane is:

$$\Delta R = \sqrt{(\Delta\eta)^2 + (\Delta\phi)^2}, \tag{3.2}$$

where $\Delta\eta$ and $\Delta\phi$ are the distance from the axis in the η and ϕ directions, respectively. Usually, ΔR is used to denote the shower size and distance of objects reconstructed in the ATLAS detector in the $\eta - \phi$ plane.

To get an excellent performance of ATLAS, sub-detectors are required to satisfy at least the basic design performance: robust and efficient tracking and vertexing of the inner detector; very good discrimination power and precise energy measurement of electron and photon of the electromagnetic calorimeter; compensated hadronic calorimeter for jet energy measurement and E_T^{miss} calibration; precise momentum measurement of muons in muon spectrometer; almost full coverage of the geometry that large acceptance in η and almost full acceptance in ϕ; and excellent trigger system providing high efficient acceptance of interesting physics processes.

3.2.2 Inner Detector

Inner Detector is to measure the charged particles momentum and to reconstruct the vertex with high precision. It is comprised of three sub-detectors: Pixel Detector, Semi-Conduct Tracker (SCT) and Transition Radiation Tracker (TRT), and solenoid that provides magnetic field for the trackers. Pixel is the most inner detector, while SCT is in between Pixel and TRT. Pixel and SCT are referred to as Precision Tracker, and they are called silicon detectors together as well. All the sub-detectors are composed of barrel and end-caps to get the maximum geometry coverage. The total η coverage of the whole inner detector is 2.5, where TRT covers up to $\eta = 2.0$ and silicon detectors cover up to $\eta = 2.5$. The outer radius is 115 cm with the inner radius 4 cm, while the length is 7 m. The inner dimension of the cryostat that contains the LAr EM calorimeter fixes the inner detector at fixed position. Pixel and SCT are made of semi-conductor that provides a very good resolution. TRT is made of straw tubes that give bad resolutions, however, the straw tubes can provide continuous hits of tracks to compensate the bad resolution from as single straw tube and then output good resolutions. Figure 3.4 shows the sketch of the longitudinal (a) and the lateral (b) view of the Inner Detector to give an idea of its structure.

3.2.2.1 Pixel Detector

Pixel detector [41] is the most inner sub-detector containing three barrel layers with the radius of the first layer 4 cm (surrounding the beam pipe), the second layer 10 cm and the third layer radius 13 cm, and 5 end-cap disks on each side. The first layer, called B-layer, covers the η range up to 2.5, while the second and third barrel layers η coverage is 1.7 compensated the end-caps up to 2.5. Figure 3.5 shows the sketch of the pixel detector.

The semi-conductor pixel is the smallest element in the Pixel detector. The size of a single pixel is 50 μm $\times$ 300 μm in $R\phi$ and z, respectively. 61440 pixels, arranged in an array of 24 by 160 and readout by 16 chips, compose of one module whose size is 62.4 mm long and 21.4 mm width. The size of the barrel and end-caps modules is designed to be the same. The barrel contains 1500 modules while the end-caps contain 700 disk modules. The modules are fastened using one type of support structure in the barrel and two types in the end-caps. Therefore, 140 million pixel elements compose the whole pixel detection. With such high-granularity, the resolution is expected to be 12 μm in direction $R\phi$ and 66 μm in direction z for the barrel layers, while the end-cap disks are designed to provide resolution 12 μm in direction $R\phi$ and 77 μm in direction R. In addition, the choice of the material is strict that it is able to withstand over 300kGy of ionizing radiation and thin enough to reduce the material before calorimeter. At last, the thickness is designed to be 17% radiation length for each layer.

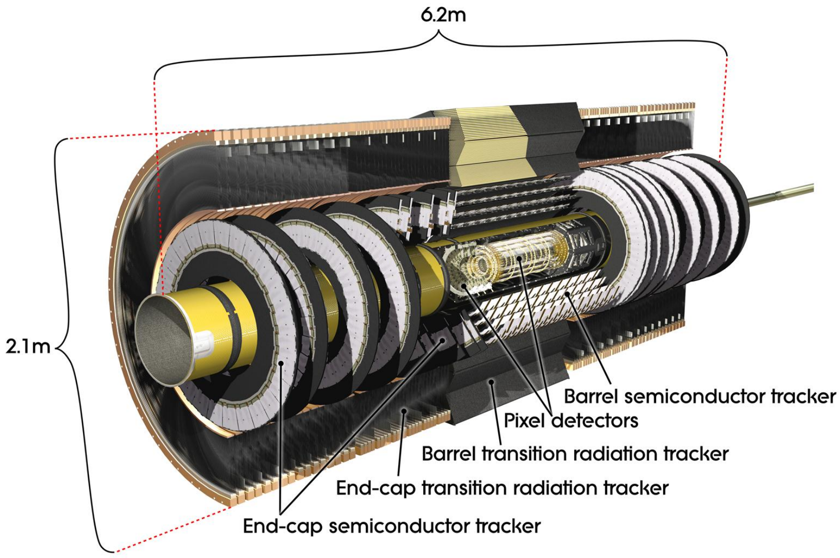

(a)

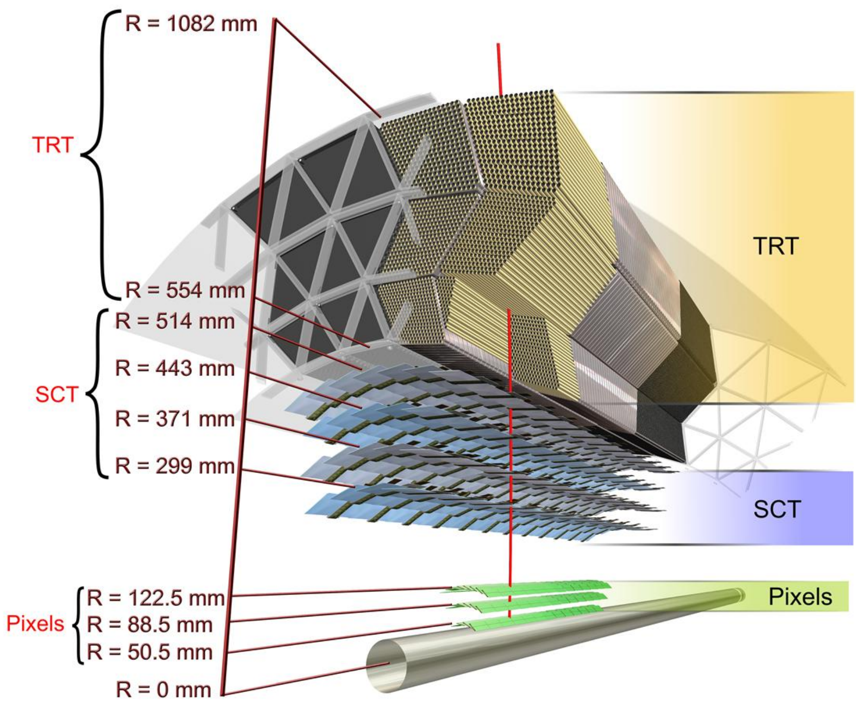

(b)

Figure 3.4: a) Longitudinal and b) lateral sketch of the Inner Detector.

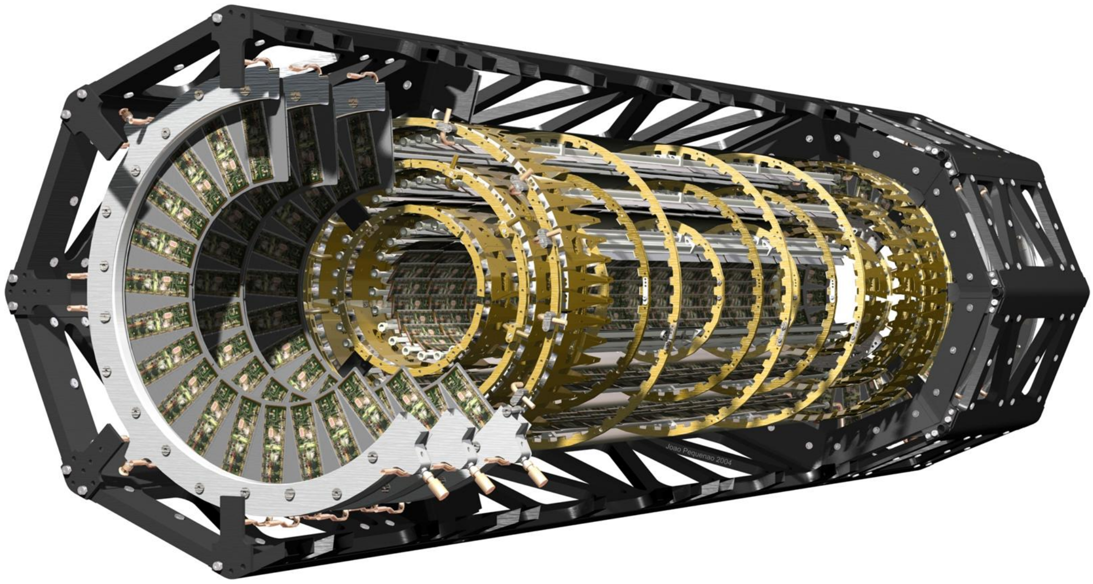

Figure 3.5: Sketch of the Pixel detector.

3.2.2.2 SCT

SCT [40] is installed out side of the Pixel detector with eight barrel layers and nine end-cap disks on each side. The coverage of the barrel part is up to 1.4 in η direction, while the end-caps covers the rest region up to $\eta = 2.5$. The barrel layers radii are 30.0, 37.3, 44.7 and 52.0 cm from inner to outer.

The smallest element of the SCT detector is readout strip with 6.4 cm long. 768 readout strips of 80 μm pitch compose a silicon detector with 6.40 cm long and 6.36 cm width. Two silicon detectors are wire-bonded together forming a 12.8 cm long strips array. A pair of the two wire-bonded silicon detectors are glued back-to-back at a 40 mrad angle to constitute a module. Figure 3.6 shows a picture of one of the SCT modules in the second layer. The modules are arranged on carbon-fibre cylinders in the barrel, while the carbon-fibre cylinders carry cooling system. The end-caps modules are assembled to disks with the rounds number up to 3. Nine disks in each side are interconnected by a space-frame.

SCT provides 6.2 million readout channels with about 61 m^2 silicon detectors. The resolution of the SCT detector is designed to be 16 μm in $R\phi$ for both barrel and end-caps regions and 580 μm in z (R) for the barrel (end-caps) region.

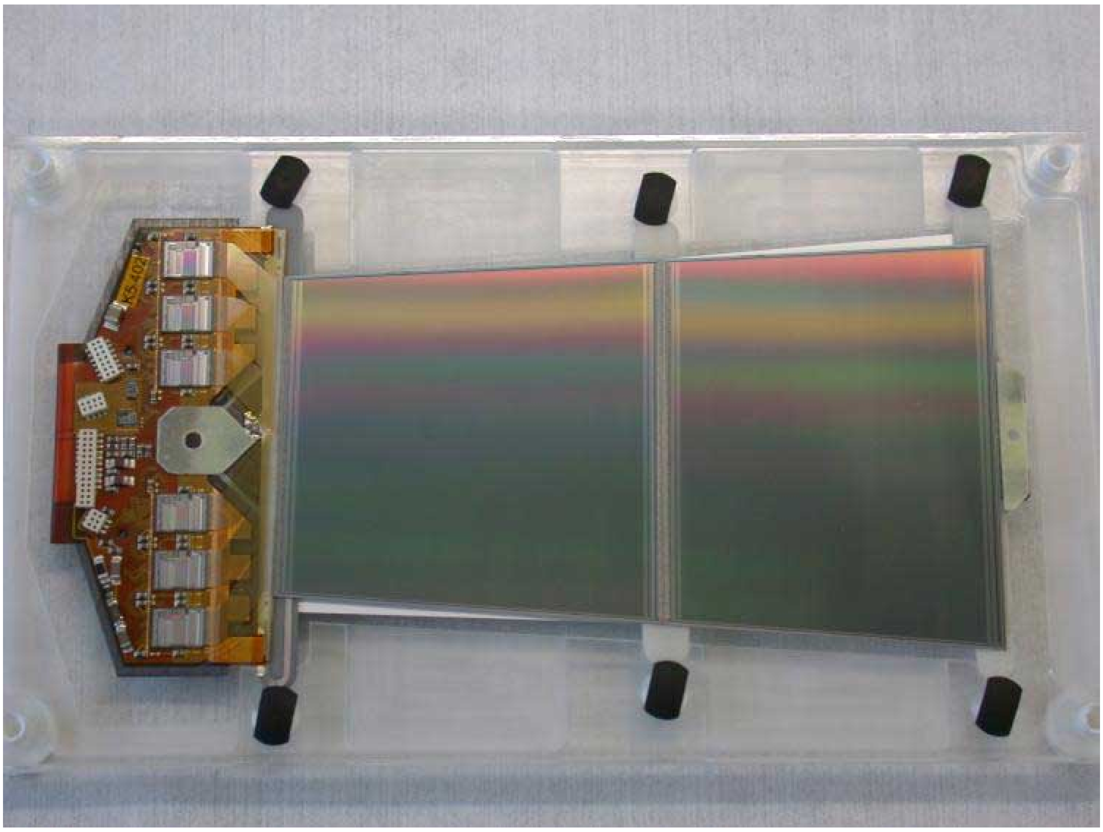

Figure 3.6: Picture of a module from the second layer of SCT barrel region.

3.2.2.3 TRT

TRT [40] is the most outer ID sub-detector made up of 298304 radial straws with barrel (end-caps) part takes 52544 (245760) and providing typically 36 continuous hits of the tracks. The barrel region covers up to $\eta = 0.7$ while the end-caps supply the rest coverage up to $\eta = 2.0$.

Radial straw is the smallest element with a diameter of 4 mm and the maximum length 144 cm which is in the barrel part [42]. To get a fast response, straws are equipped with a 30 μm diameter W-Re wire which is gold-plated. Mixed gas with 70% Xe, 20% CO_2 and 10% CF_4 are designed to fill the straws. But at last the mixed gas ingredients are changed to 70% Xe, 27% CO_2 and 3% O_2, N_2 taking 0.5% typically. Two kinds of individual modules covering the radii from 56 to 107 cm are designed with 329 and 793 straws in each. The end-caps modules covers the radii from 64 to 103 cm.

The resolution of an individual straw is 170 μm on average. Its resolution is worse than the silicon detector, but by combining a continuos measurements, a $\sim$ 50 μm position resolution is achieved.

3.2.2.4 Solenoid

The central solenoid (CS) [43] is installed outside of the TRT detector to provide magnetic fields for the inner detector using super-conducting technology. It is 5.238 m long, 1.247 m radii and 1154 turns [44], as shown in figure 3.7. It provides 2 T magnetic field in the trackers while the peak value is within itself that is 2.6 T. To minimize the upstream material before the calorimeter, it is required to be designed as thin as possible without effect on the stability. Doped aluminum is chosen as the stabilizer with flat superconducting cables located in the center. It provides magnetic fields along the z direction. Therefore, tracks in the inner detector are bended in the azimuthal direction that the position resolution provided by inner detector is worse along the beam line comparing the transverse plane.

3.2.3 Colorimeters

Calorimeters are installed outside of the inner detector to measure particles energy produced in the p-p collision [45]. They contain electromagnetic calorimeter and hadronic calorimeter. Electromagnetic calorimeter is a lead/liquid-argon (LAr) detector, while

Figure 3.7: A picture of the solenoid overview.

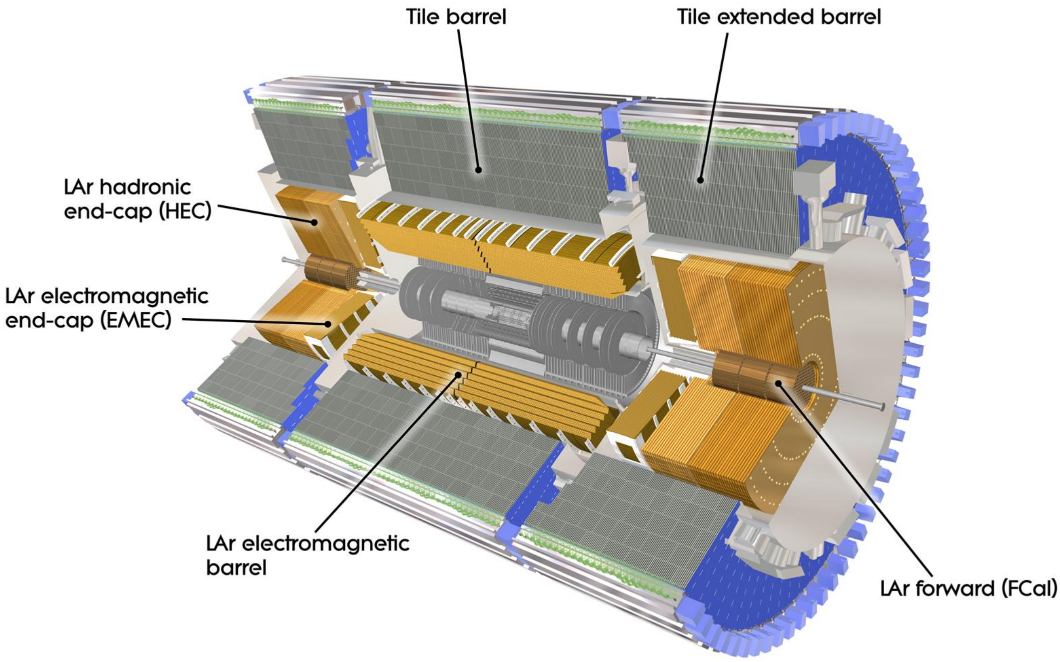

Figure 3.8: Sketch of the calorimeter detectors.

hadronic calorimeter consists of tile calorimeter in the barrel and LAr detectors in the end-caps and forward region. The whole calorimeter covers up to $\eta = 4.9$ and almost full azimuthal coverage to provide an all-directions measurement of the energy for the jet and E_T^{miss} reconstruction and calibration. Figure 3.8 shows the sketch of the calorimeters at ATLAS.

3.2.3.1 Electromagnetic calorimeter

Electromagnetic calorimeter (EM) [47] is installed outside of the inner detector but before the hadronic calorimeter. It is composed of barrel (EMB) and end-caps (EMEC), that EMB covers region $\eta < 1.475$ and EMEC covers $1.375 < \eta < 3.2$, housed on cryostats (one for barrel and two for end-caps). The barrel part installed on the A-side of the ATLAS is called EMBA, while the one installed on the C-side is called EMBC. Similarly, the end-cap calorimeter installed on the A-side is called EMECA, while the one installed on the C-side is called EMECC. The two barrel parts are separated with a gap about 6 mm at $z = 0$.

The electromagnetic calorimeter is a lead/liquid-argon sampling calorimeter, using lead as the absorber, liquid argon as the active calorimeter. Stainless steel and copper are used as the readout electrodes. The advantage of using the liquid-argon as the active material is to address the issues like fining granularity, easy calibration, radiation suffering and stability. At LHC, the time space between two collisions is typically 25 ns, which is challenge of the fast readout in the EM calorimeter. Accordion geometry is designed to reduce the capacitance between the two electrons and therefore faster signal readout is obtained [49]. The arrangement of the absorber, active material and readout electrodes is shown in the left plot of the figure 3.9. Two copper layers are glued on a kapton layer as the positive electrodes. The copper layer glued on one side of the kapton is called outer layer, while on the other side is called inner layer. The gap between the copper and the negative electrode is for the liquid-argon. The LAr gap size is constant in the barrel section (2.09 mm), while it changes to smaller value at larger η region in the end-cap sections [53]. The negative electrodes are stainless steels that are glued on the absorber lead. The thickness of the absorber is slightly different with respect to η to the best energy resolution of the EM [32]. The lead and stainless steel, together with the copper electrodes are made into accordion geometry, as shown in the picture in the right plot of figure 3.9.

Figure 3.10 shows a sketch of a module from the EM calorimeter with the accordion geometry [49]. The EM is divided into three layers in the direction perpendicular to the beam line. The three layers are called, successively, front layer (or strip layer or first layer), middle layer (or second layer) and back layer (or third layer or last layer). The front layer with a constant radiation length $\sim 6X_0$ is designed to be a very fine granularity section in the η direction that is $\Delta\eta = 0.003$ for the purpose of reconstructing the objects shower shape. The middle layer, with the thickest material, is to produce showers of the electromagnetic particles for stopping and measuring their energy. The back layer, with the radiation length varying from 2 X_0 to 12 X_0 with η [32], is to prevent the leakage of the energy to the hadronic calorimeter. To correct the energy lost before the EM calorimeter, a presampler before the strip layer is used. The presampler covers $|\eta| < 1.8$ consisting of an LAr layer with thickness of 1.1 cm in the barrel and 0.5 cm in the end-caps. In the region $1.0 < |\eta| < 1.6$, the transition region between barrel and end-caps, the presampler is supplied by a scintillator slab [32]. It is not recommended to use region $1.37 < |\eta| < 1.52$ in the physics analysis involving

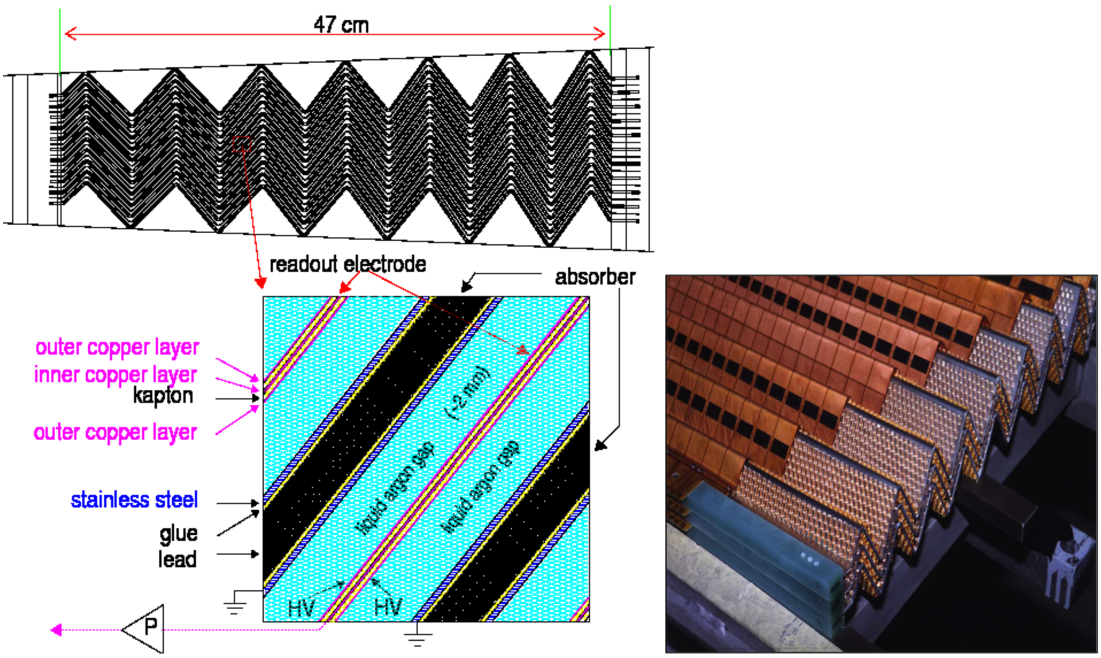

(a) (b)

Figure 3.9: The arrangement of the material in the EM calorimeter (left) and the picture for the accordion struction (right).

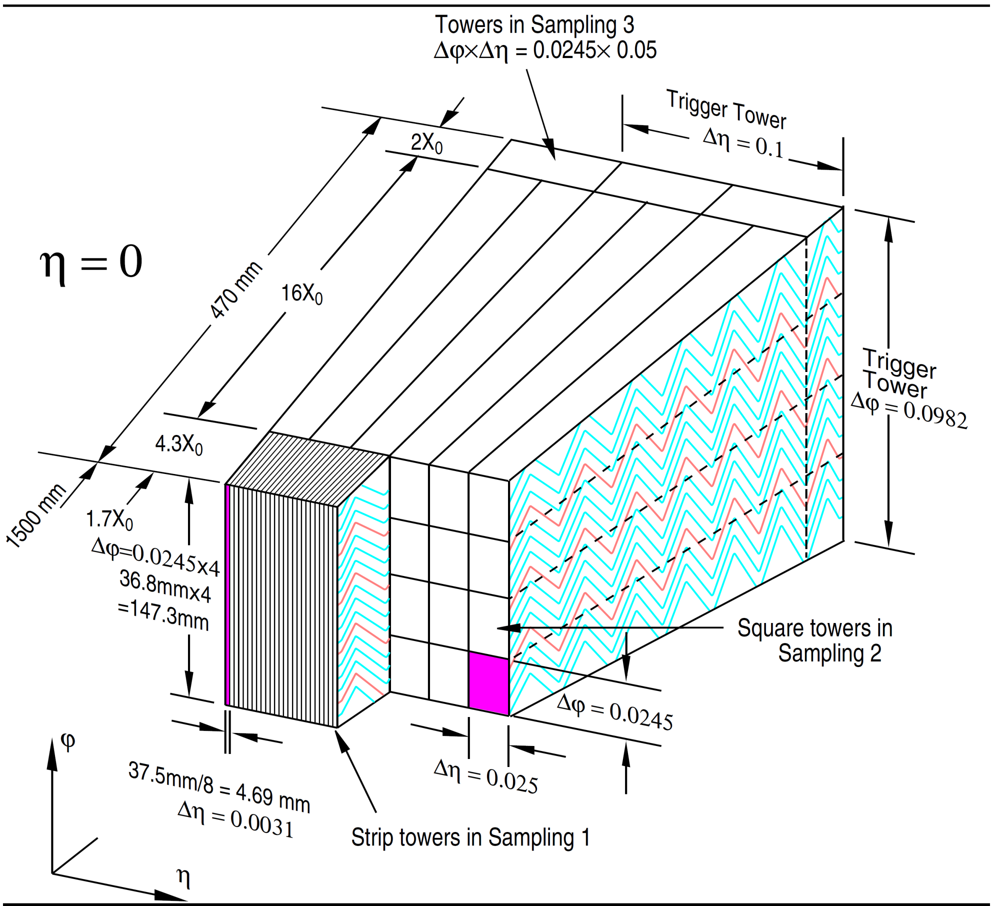

Figure 3.10: Sketch of a module in the EM calorimeter with the diameters quantities.

photons. To illustrate the complicated structure of the EM, table 3.1 granularity and coverage of different layers. All the sub-sections provide a full coverage in the azimuthal direction.

The energy reconstruction in the EM calorimeter is illustrated in section 4.2.4. Figure 3.11 shows the signal shape for one of the cell in the second layer of EMB (left). The measured shape agrees to the predicted one within 4% [52]. The performance studies of the LAr with cosmic runs and collision data have been implemented. The right plot of the figure 3.11 shows the energy reconstructed in the end-cap using 900 GeV collision data. Clearly seeing that MC predicts data very well both for noise events (from random trigger) and real energy.

	Layers	Granularity ($\Delta\eta \times \Delta\phi$)	Coverage ($|\eta|$)
Barrel	Presampler	0.025×0.1	$|\eta| < 1.52$
	Strip layer	0.003×0.1	$|\eta| < 1.475$
	Middle layer	0.025×0.025	$|\eta| < 1.475$
	Back layer	0.05×0.025	$|\eta| < 1.475$
End-cap	Presampler	0.025×0.1	$1.5 < |\eta| < 1.8$
	Strip layer	0.025×0.1	$1.375 < |\eta| < 1.5$
		0.005×0.1	$1.5 < |\eta| < 1.8$
		0.004×0.1	$1.8 < |\eta| < 2.0$
		0.006×0.1	$2.0 < |\eta| < 2.5$
		0.1×0.1	$2.5 < |\eta| < 3.2$
	Middle layer	0.025×0.025	$1.375 < |\eta| < 2.5$
		0.1×0.1	$2.5 < |\eta| < 3.2$
	Back layer	0.05×0.025	1.5¡$|\eta| < 2.5$

Table 3.1: The granularity and geometry coverage of different layers of EM calorimeter in the barrel and end-caps parts, including presampler as well. All the sub-sections covers the full azimuthal direction.

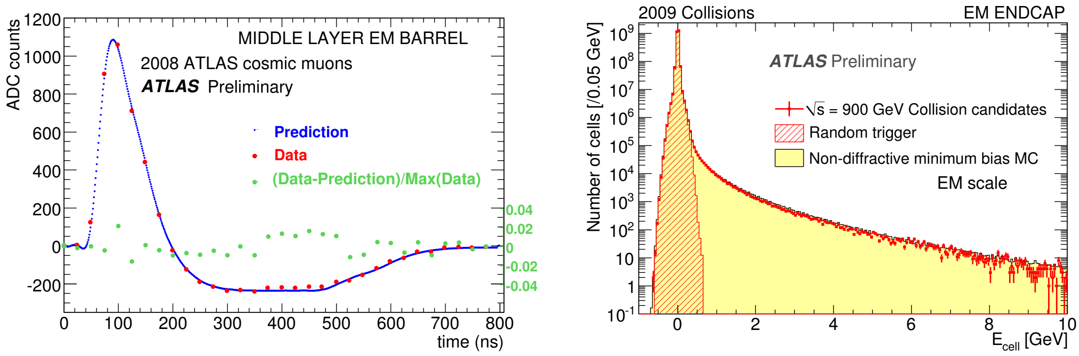

(a) (b)

Figure 3.11: The pulse shape obtained from cosmic run comparing to the predicted one obtained from calibration run (left) and the data/MC comparison of the reconstructed energy in the end-caps overlaid with the noise events from random trigger (right).

3.2.3.2 Hadronic calorimeters

The hadronic calorimeter is installed outside of the EM calorimeter with the scintillator-iron technical (tile) calorimeter in the barrel region covering $|\eta| < 1.7$ and LAr technical similar as the EM in the end-cap and forward regions covering $|\eta|$ up to 4.9.

- **Tile calorimeter**

  Tile calorimeter [55] consists of barrel (longitudinal barrel denoted as LB) and extended barrel (EB) parts. The part of LB (EB) installed on the A-side of the ATLAS is called LBA (EBA), while the part on the C-side is called LBC (EBC). In the azimuthal direction, the tile calorimeter is divided into 64 equal modules with a 1.5 mm gap between each two [59], while in the η direction, the readout cells are 'pseudo-projective' to the center of the ATLAS detector [60]. The coverage of LB in $|\eta|$ is up to 1.0, while EB covers $0.8 < |\eta| < 1.7$. Similar as EM calorimeter, the tile calorimeter is divided into three layers perpendicular to the beam line with interaction length (λ) 1.4, 4.0 and 1.8, respectively. They are called layer-A (or first layer), layer-BC (or second layer) and layer-D (or third layer). The radii of the tile calorimeter is from 2.28 m to 4.5 m with total weight about 2630 tons [59].The granularity is much simpler than EM calorimeter that layer A and B are 0.1×0.1 and layer C is 0.2×0.1 in $\Delta\eta \times \Delta\phi$.

  It is a scintillator-iron sampling calorimeter with iron and scintillator-tile periodically arranged along the direction z, with 3 mm tile and 14 mm iron plates in one period, as shown in figure 3.12 [55]. Scintillator-tile is the active material while iron is used as absorber. The readout system, which is fast for the signal processing, are wavelength shifting fibers on both sides of the scintillator to readout signal to two photomultipliers separately.

- **Hadronic LAr**

  Hadronic LAr [47] are the end-caps of the hadronic calorimeter (Hadronic End-Cap: HEC) utilizing the similar techniques as the electromagnetic calorimeter but with different geometry and absorber. It consists of two wheels on each side with the ones near to the collision point constructed with copper plates of thickness 25 mm and the ones further to the collision point built with 50 mm copper plates. The copper is used as the constructer and absorber. In each

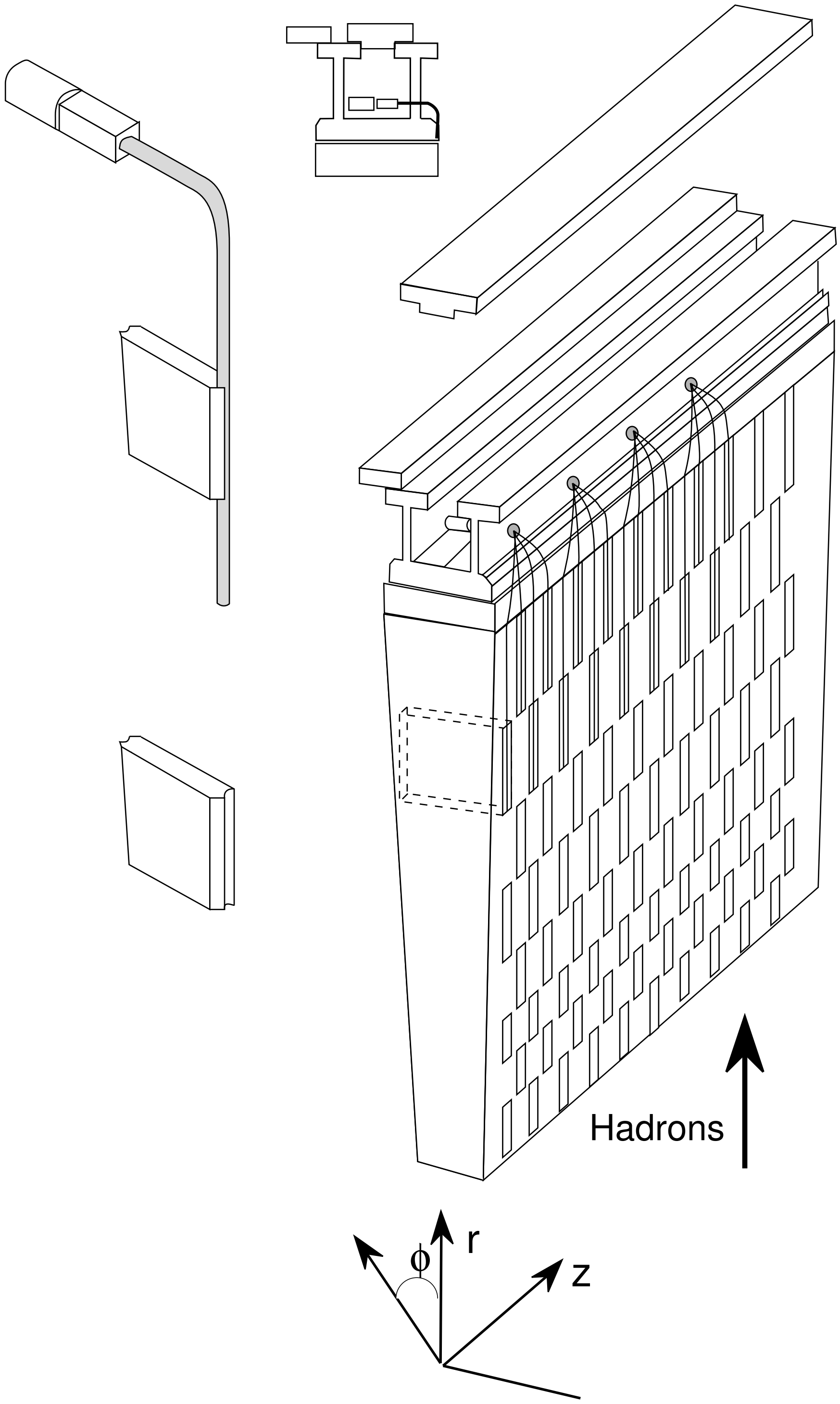

(a)

Figure 3.12: Sketch of the tile calorimeter module. The tile and iron plates are arranged periodically along the z direction.

wheel, 8.5 mm gaps between the two copper plates are divided into four equal drift spaces ($\sim$ 1.8 mm) by three parallel electrodes with the middle one for the signal readout. The coverage of the HEC in $|\eta|$ is up to 3.2 with granularity in $\Delta\eta \times \Delta\phi$ of 0.1×0.1 within region $1.5 < |\eta| < 2.5$ and 0.2×0.2 within region $2.5 < |\eta| < 3.2$.

- **Forward calorimeter**

  Forward calorimeter (FCAL) [47] is installed in the forward region ($3.1 < |\eta| < 4.9$) trying to cover as near as possible to the pipe line to measure the jets produced in soft collision. In that region, material standing with large radiation is needed. It is installed 4.7 m far from the interaction point for the reduction of radiation consideration.

  Three sections constitute the forward calorimeter housed on the end-cap cryostat and an external tube that is to carries the FCAL weight and withstands the end-cap cryostat wall. The first section utilizes copper as absorber while the second and third sections use tungsten as absorber.

  The geometry of the FCAL is built out with metal matrix filled with rods and tubes in the longitudinal channels, that rods are at high voltage while matrix and tube are grounded [32].

Tile calorimeter, HEC together with FCAL provide almost full coverage of the space to measure the jets produced in the collision, there for E_T^{miss} will be reconstructed well under this geometry.

3.2.4 Muon spectrometer

Three parts with different purposes constitute the muon chamber: The toroid providing the magnetic field to bend the muon tracks, the trigger instrumented and the momentum measurement chamber.

The toroid is composted of eight large air-core coil installed symmetrically around the beam line outside of the hadronic calorimeter (the barrel toroid) and two end-caps installed at the ends of the barrel toroid. The barrel toroid covers $|\eta|$¡1.0 while the end-caps cover $1.4 < |\eta| < 2.7$. In the transition region $1.0 < |\eta| < 1.4$, no precise measurement is provided due to the multi-scattering. The toroid provides 4.1 T (3.9 T) magnetic field in the barrel (end-caps) for the muon chamber in the direction of the azimuthal angle, therefore, the muon tracks resolution in R-z direction is good.

The trigger instruments consists of Resistive Plate Chambers (RPCs) covering the barrel region and Thin Gap Chambers (TGCs) providing trigger system for the end-cap regions. The trigger system coverage is $|\eta| < 2.4$ with high time resolution, fine granularity (1 cm) and high position resolution of muon tracks.

The precise readout system includes Monitored Drift Tubes (MDTs) covering $|\eta| < 2$ and Cathode Strip Chambers (CSCs) to withstand the high radiation covering $2 < |\eta| < 2.7$. They provide a precision measurement parallel to the bending direction that is R-z direction, where R refers to the end-cap and transition regions and z refers to the barrel region. The resolution of the MDTs is at accuracy of ~ 30 μm.

3.3 Data taking structure at ATLAS

LHC provides beams to every experiment apparatus and makes the beams collision in the center of every detector. Beams and collisions are controlled by LHC while each experiment manages their own data taking. To control the data well, several scales on time are defined.

- LHC Filling, period when beams are filled in the machine.

- Run, a run is defined as the period of data taking of a detector, e.g period between the detector starting and stopping to readout data. A run is called calibration run if it is taken for calibration purpose. Usually, calibration runs are taken with sub-detectors independently. A run is defined as a physics run when it is taken for physics analysis. Mostly, physics runs require all the sub-detectors combined together and synchronized to LHC clock. Usually, when there are collisions, physics runs are taken.

  To distinguish runs with each other, a unique number is assigned to this run when it starts, which is called run number. Several successive runs with similar ATALS detector configuration are assembled into a run period.

- Luminosity Block (LB), smaller time scale during a run. Sub-division of a run into luminosity blocks of length 2 minutes is implemented to control the data. LB is the smallest granularity of data taking. If there are problems with detectors in this LB, the LB will be flagged as problematic and not used for analysis.

3.4 Trigger and computing

3.4.1 Trigger

Three levels of trigger are used for the event selection before the events being reconstructed offline. The first level is hardware-based called LVL1, while the second and third levels are software-based called LVL2 and EF respectively. LVL2 and EF are both called High Level Trigger (HLT). Higher levels of triggers process events based on the information provided by the previous level of the trigger, so a trigger chain is formed.

The purpose of the trigger is to reduce the readout rate to reduce the storage of the data. The challenge of the trigger is to select interesting events within a very short time space. The LHC collision rate is 40 MHz and the ATLAS final readout rate at EF level is designed to be 200 Hz. LVL1 trigger is required to make decision within 2.5 μm and reduce the readout rate to 75 kHz(40 kHz in the start stage of the LHC) by discarding the not interesting events. LVL2 trigger is required to reduce readout rate to 2 kHz (1 kHz in the start stage of the LHC). The EF are finally reduce the readout rate to 200 Hz. [61].

3.4.2 Computing

Events in each run passing EF trigger are processed through several stages until to the format useful for analysis. At each process stage, a unique data format is allowed. The data selected by the trigger (raw data) are reconstructed firstly and centrally in the computer farm called teir-0 located at CERN. The reconstructed events are assembled into to a data format called Event Summary Data (ESD), the ESD is reconstructed again to Analysis Object Data (AOD). The ESDs are then assigned to different grid sites by saving only 10% of the total data statistics, while the AODs are duplicated at least in two different sites with full data statistics. At last, flat ntuple data format (D3PD) that can be analyzed using ROOT [62] directly are produced base on AOD. The reconstruction and analysis frame of the ATLAS data is called Athena, which is now developed to release 16 until now. Analysis can be based on AOD and ESD datasets as well.

4

Pion response in calorimeter using combined test beam data collected in 2004

4.1 Introduction

The purpose of test beam is to understand a detector's response to different kinds of particles. Calorimeters are detectors to measure the energy deposited by particles showering in them. Electromagnetic like particles, such as electrons and photons, deposit almost all of their energies in the electromagnetic calorimeter by producing electromagnetic showers. For hadronic particles, like pions and koans that are main part of jets in the proton-proton collision, deposit their energies mostly in the hadronic calorimeter. Test beam set-up in 2004 was to understand the response of single electron and pion response in the ATLAS sub-detectors. The energy of electrons and pions were known in the test beam, unlike the particles produced in the p-p collision. Therefore, the study of particles' response with known energy is the first step for the ATLAS experiment.

4.2 The combined test beam set-up

4.2.1 The beam line set-up

The test beam was produced and accelerated in PSB, PS and SPS. The equipments of test beam were installed at H8 beam line on SPS. Proton beams with constant energy of 450 GeV were produced in SPS and were impacted on a beryllium primary target with thickness up to 30 cm. The secondary particles, including electrons, pions, muons and koans were produced through electroweak and nuclear interactions between protons and target material. The secondary particles were then selected by monitors and passed through different beam lines:

- Particles with energy between 10 GeV and 400 GeV (high energy beams denoted as HE) were selected and collimated along the straight beam line that was the same direction as the input proton beam [63]
- Pions taking energy lower at 80 GeV were directed to another beam line by a magnetic field and were impacted to a polyethylene target with 1 m long installed 45 m before the experiment setup up to produce beams with energy lower than 10 GeV (Very Low Energy beams denoted as VLE). The VLE beams were then re-directed to the HE straight line after collimated [64].

Figure 4.1 shows the beam line set up for the test beam in 2004. The devices on the beam line were to collimate, identify and measure the measure the momentum of the particles. The blue triangles in the figure denote the positions of dipoles; the yellow tangles denote Cherenkov counters which are used to identify pions from electrons; the pink tangles $BC0$, $BC-1$ and $BC-2$ denote the beam wire chamber used to measure the beam momentum by measuring the deflection angle of it; the cyan tangles S0, S1, S2 and S3 denote the trigger scintillators used to trigger events; SMV and SMH denote the muon scintillator used to veto the muon in the HE beam line and beam halo before beam reaching the detector [63]. HE pion beams were produced from 20 to 350 GeV, while VLE pion beams were 2 to 9 GeV.

4.2.2 The detector set-up

Several modules of the barrel region of the ATLAS sub-detectors were install after the beam line set-up for the data taking. All the modules from sub-detectors were installed in a similar way to the real ATLAS detector. The hardware readout and software reconstruction were implemented in a similar way to the real ATLAS as well. Figure 4.2 shows the sub-detectors arrangement.

The inner detector system is composed of six modules of Pixel detector, two modules of SCT and two wedge of TRT, as well as magnet to provide magnetic field for the Pixel

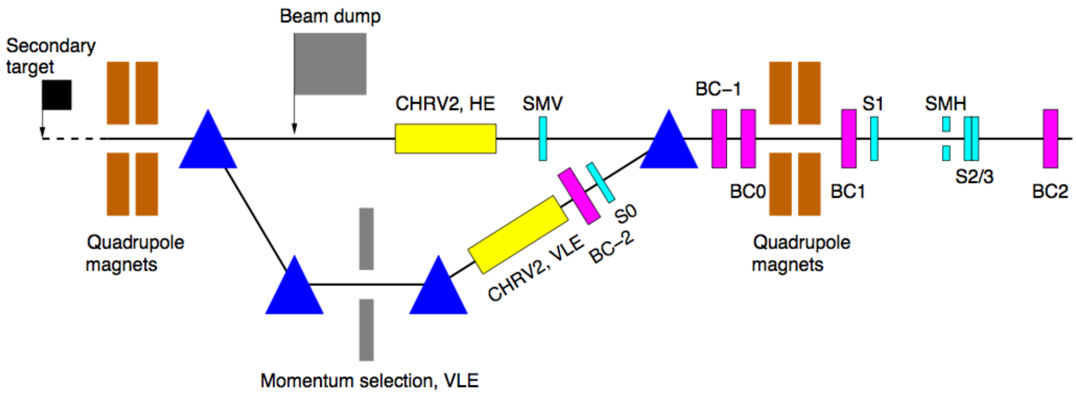

Figure 4.1: The beam line set-up for test beam that is on H8 beam line at SPS in 2004.

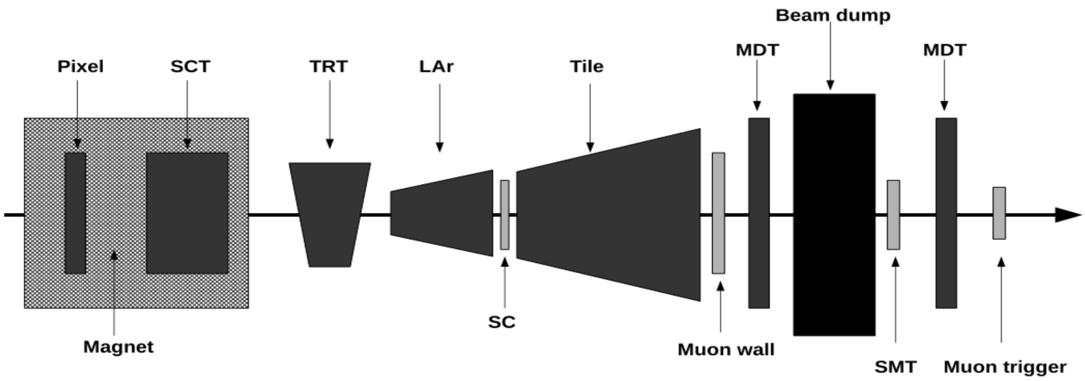

Figure 4.2: The detectors set-up for the data taking of test beam in 2004.

and SCT (different from ATLAS where TRT is install inside the magnetic field). The calorimeter system includes one module of liquid argon calorimeter (LAr), three barrel modules and three extended barrel modules of tile calorimeter, as well as cryostat to house the LAr calorimeter module. Several muon detectors section are installed after the hadronic calorimeter modules, but are not used in the analysis.

The **Pixel detector** consists of six modules arranged as 3 compartments and 2 sectors. It is the first sub-detector the test beam injects into and is positioned at a positive angle with respect to injecting beam direction. The **SCT** consist of two modules installed after the pixel modules and is provided with 2 T magnetic field together with the pixel modules by the magnet. The **TRT** wedges are installed after the SCT at a distance 1114 cm with respect to the last module of SCT and outside of the magnetic field. The **LAr module** is installed after the TRT, with a coverage at $\eta - \phi$ plane of $0 < \eta < 1.4$ and $-0.2 < \phi < 0.2$; the cryostat is made of aluminum and consists of an inner and outer walls with thickness of 4.1 cm and 3.9 cm and is separated by a vacuum gap [63], which is installed surrounding the LAr module to house the LAr; a foam block is stalled between the cryostat and the LAr for excluding the LAr in front of the calorimeter. The **tile calorimeter** is installed after the LAr module and outside of the cryostat; three barrel and three extended barrel modules are used for the analysis with a coverage in $\eta - \phi$ plane of $-1 < \eta < 1$ and $-0.15 < \phi < 0.15$.

4.2.3 Data collection

The pion beams are separated into π^+ and π^- to understand the detector response separately. π^+ beams are produced at energy 20, 50, 100, 150 and 180 GeV, while π^- beams are produced at energy 150, 180, 200, 250, 320 and 350 GeV. All the $\pi^\pm$ beams are injected in several fixed η directions mimicking the η position in the ATLAS. The η directions are 0.20, 0.25, 0.35, 0.45, 0.55 and 0.65.

4.2.4 Energy reconstruction in the LAr

The energy reconstruction in the LAr modules is similar to the one at ATLAS. Charged particles from the beam (produced by collisions at the ATLAS) or the shower in the absorber lead pass through the sensitive material LAr and produce ionized electrons. The ionized electron drift to the electrodes and produce electrical currents proportional to the energy deposited by the charge particles in the cell [53]. The ionized signals are transited to the read-out system through cables. In the test beam set-up, the read-out crates are installed on the cryostat, including the Frond End Boards (FEBs) and calibration boards housed there.

The calibration boards are used to provide signal having exponential shape to the detector with know amplitude. The calibration signal is then reconstructed in the way the same as the physics signal. The purpose of calibration signal is to calibrate the non-uniform response and different capacitance among cells [52].

The ionized signals are amplified on the FEB. Then the amplified signals are shaped and sampled $N_{samples}$ times every 25 ns (the default $N_{samples}$ is five in the physic runs at ATLAS and 32 in the calibration runs) [51]. Each sample is then digitized. The digitized signals are used to reconstruct the cell energy by the formula:

$$E_{cell}^{rec} = F_{\mu A \to MeV} \cdot F_{DAQ \to \mu A} \cdot \frac{1}{\frac{M_{phys}}{M_{cali}}} \cdot \sum_{i=1,2} R_i [\sum_{j=1}^{N} OFC_j (S_j - Ped)]^i, \tag{4.1}$$

where the terms are defined as bellow:

- $\boldsymbol{S_j}$ is the j^{th} sample for the digitized signal in the cell.
- ***Ped*** is the pedestal for each cell. It is obtained from runs taken without any beam or calibration pulse injection [51].
- $\boldsymbol{OFC_j}$ is the coefficient for sample j: given a digitized signal shape, its amplitude is reconstructed using Optimal Filtering (OF) method [66], that the amplitude is a linear weight sum of coefficients (OFC) of the digitized sample with each sample is subtracted by the pedestal [63].
- $\boldsymbol{R_i}$ is the ramp denoting the relation between the injection current on the calibration board in the unit of DAC-counts and the reconstructed output amplitude in the unit of ADC-counts. It is obtained from calibration boards. The injected signals are known in the calibration run. For a fixed channel on the calibration boards, the injected signal is changed step by step then the out signal amplitude is reconstructed at each step. The relation between the injected signal and the out signal amplitude is described by a polynomial. R_i is the i^{th} order of the relation [52]. In the test beam, the highest polynomial order is two as shown in equation 4.1.

- $\frac{1}{\frac{M_{phys}}{M_{cali}}}$ corrects the difference between the signal obtained from calibration board and the one from FEB.

- $\boldsymbol{F_{DAQ\rightarrow\mu A}}$ is to convert current in DAQ unit to μA.

- $\boldsymbol{F_{\mu A\rightarrow MeV}}$ is to convert current to energy.

Detailed description of energy reconstruction for LAr calorimeter is in reference [50].

4.2.5 Energy reconstruction in the tile calorimeter

Tile calorimeter use scintillator as the sensitive material and iron as the absorbing material. Scintillator and iron plated are arranged in a periodical manner: one scintillator with thickness of 3 mm $\rightharpoonup$ one iron plate with thickness of 5 mm (master plate) $\rightharpoonup$ one iron plate with thickness of 4 mm (spacer plate) $\rightharpoonup$ one iron plate with thickness of 5 mm (master plate). They forming a period of a scintillator−iron structure with 18 mm long [56, 57, 58]. The light produced in the scintillators by the passing through particles is transported via wavelength shifting fibres into photo-multipliers (PMT). The signal is amplified by the PMT and converted into electrical signal. The electrical signal is then shaped, sampled every 25 ns, amplified and digitized. The energy for each cell is then reconstructed based on the digitized signal [63].

4.3 Noise and pedestal in the calorimeters

Noise and pedestal for each LAr cell were checked during the test beam experiment. The noise and pedestal are obtained using randomly triggered (random trigger) events. Figure 4.3 shows the noise distribution for cells in each layer of the LAr. The noise shown in the figure is checked in a run with beam momentum 7 GeV and injecting η at 0.2. Data is compared to MC simulated with Geant4 in Athena release 12. MC predicts the noise value well in the middle layer and back layer where the cell size is large (0.025×0.025 and 0.05×0.025 in the $\eta\times\phi$ plane, respectively). In the strip layer the MC gives larger noise value comparing to the data where the cell size is rather small (0.003×0.1in the $\eta\times\phi$). The noise in the presampler (which is used to correct the energy lost of electrons and photons in front of the calorimeter [32]) of data is much smaller comparing to the MC.

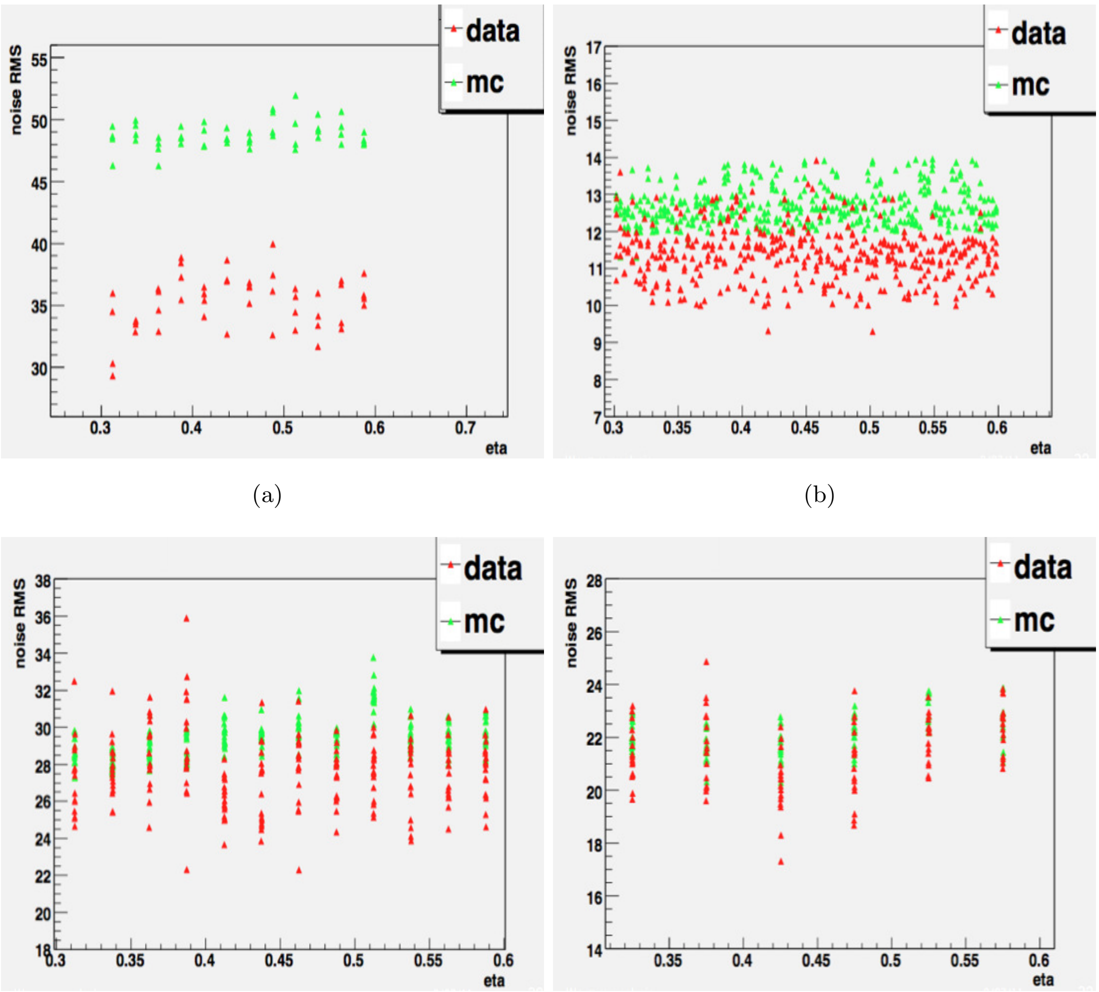

(a) (b) (c) (d)

Figure 4.3: The noise of cells in each layer of LAr obtained in test beam data and corresponding MC with beam momentum 7 GeV and injection at $\eta = 0.2$. The y-axis is the cell energy in unit MeV, x-axis denote the cells η position. a) is for the presampler, b) is for the strip layer, c) is for the middle layer and d) is for the back layer

The typical noise values are 35 MeV, 12 MeV, 28 MeV and 22 MeV for layer persampler, strip, middle and back layer of LAr calorimeter respectively [64].

Figure 4.4 shows the noise of cells in tile calorimeter for each layer. The MC predicts the cell noise of the absolute value but with a smaller spread among cells comparing to the data.

The typical noise values are 30 MeV, 30 MeV and 25 MeV for the first layer, second layer and third layer of tile calorimeter calorimeter respectively [64].

4.4 Timing in the electromagnetic calorimeter

In the ATLAS collision data taken, the readout clock of each calorimeter cell must be synchronized to the LHC clock to get the correct energy for the corresponding event [51]. The recorded signals of the measured particles are delayed due to the readout cable length and particles fly time from the interaction point to the cell [54]. The delay needs to be known for synchronizing all cells to the LHC clock. The delay of the cables can be obtained from calibration run where the input time and output time are all known. The delay due to the particles flight time exists only in collision run, but its difference from event to event is small (assuming all the particles are produced at the original point of the ATLAS. Even the primary vertex is different from the original point, the difference of the flight time from event to events is still negligible). Therefore, it can be calculated for a given cell assuming the particles flying with speed of light. The time offset is the difference of the delay time obtained from collision data and calibration data. It is required that the cell time offset of LAr should be within 1 ns [52]. In the test beam, the clock of calorimeter cell should be synchronized to the trigger time. The time offset is obtained in a similar way as in the ATLAS.

Some problems of LAr cell time offset are found during the analysis of the test beam data. Some runs show two peaks of cell time offset due to the mis-match of trigger to the event counting. As shown in figure 4.5, left plot shows the cells time offset in the LAr of a run for cells that are selected around the beam injection direction within $-0.2 < \eta_{cell} - \eta_{beam} < 0.2$ (no requirement in the ϕ direction). The cell energy is required to be greater than 2.5 GeV. Right plots shows the cells time offset versus the event number of the run. Two peaks appear in the cell time offset, with strange correlation with the event number, which means unknown problems happened during

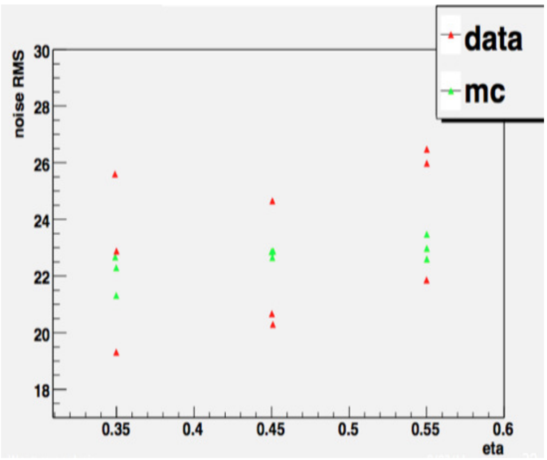

(a)

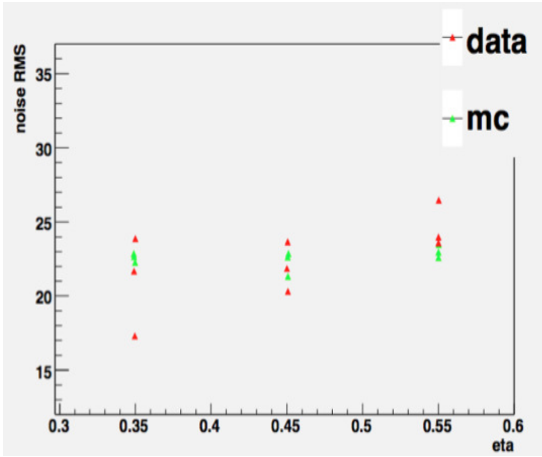

(b)

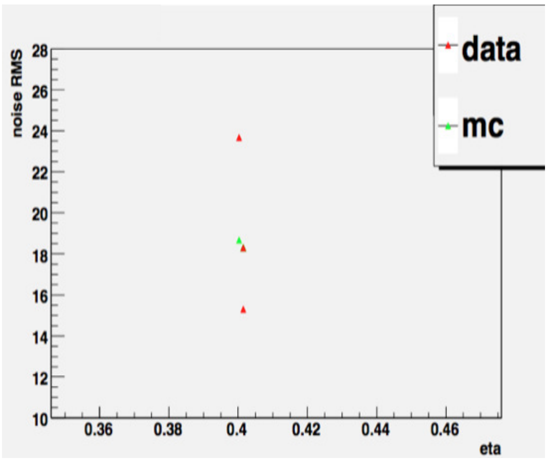

(c)

Figure 4.4: The noise of cells in each layer of tile calorimeter obtained in test beam data and corresponding MC with beam momentum 7 GeV and injection at $\eta = 0.2$. The y-axis is the cell energy in unit MeV, x-axis denote the cells η position. a) if for the first layer, b) is for the second layer and c) is for the third layer

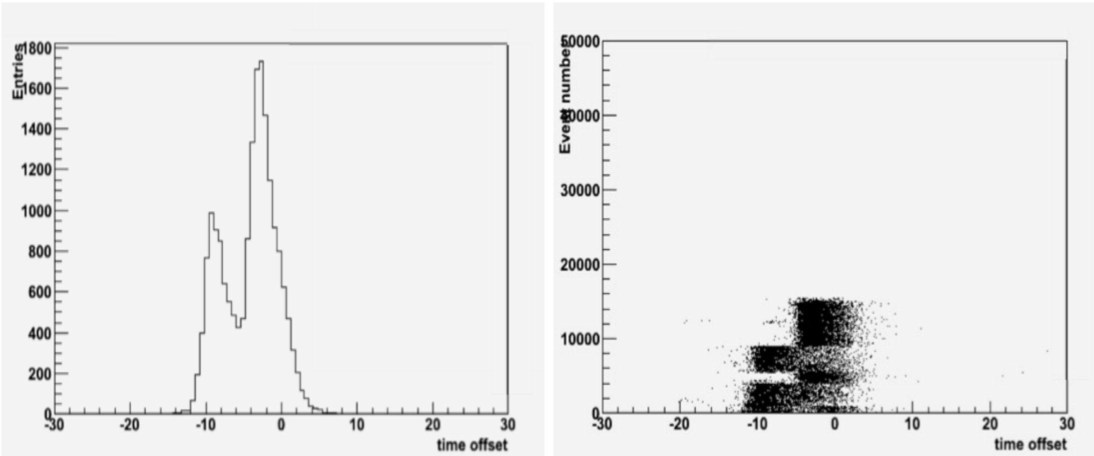

(a) (b)

Figure 4.5: The LAr cells time offset distribution (left) in a run with 200 GeV and $\eta = 0.2$ and the time offset of cells versus event number in the run (right)..

the data taken. We decide to skip these runs with the timing problem that can be repaired with reprocessing.

Figure 4.6 shows the distribution of the cells time offset distribution for a run with out trigger mis-match problem.

4.5 Combined performance of pion response in the electromagnetic and hadronic calorimeter from 20 to 350 GeV

The main issue of pion response study in the test beam is to reject electron and muon backgrounds. To reject the electron background, first and second layer of LAr calorimeter are used, where electron has different response comparing to the pion. To reject the muon background, tile calorimeter is used, where muon is expected to deposit constant energy by passing through the condensed material. Figure 4.7 shows the energy deposited by particles in the middle layer versus in the strip layer of the LAr (from runs with beam energy 180 GeV as an example). Electrons deposit most of the energy in LAr especially in the middle layer. As shown in the figure, the top-right part of the events are from electron. Comparing left and right plot, the beams energy are the same but the injection η positions are different where particles in beam with $\eta = 0.25$ pass through more material than with $\eta = 0.2$. Thus the energy deposit in the strip and

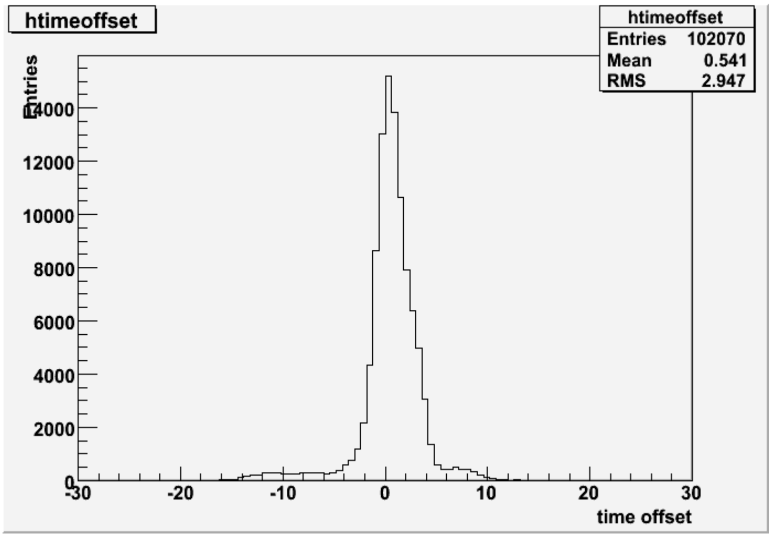

(a)

Figure 4.6: The LAr cells time offset in a run with 150 GeV and $\eta = 0.45$, where the time offset distribution is good.

middle layers for electron are both increased in the run with beam injection at $\eta = 0.25$ comparing to at $\eta = 0.2$ while the energy deposited by the other particles (bottom-left part) is not changed (because the energy deposition is through ionization instead of shower). The red straight line dividing bottom-left and top-right parts in the plots is to separate the electron from other particles. The red horizontal line is to reject π^0 which deposit most of its energy in the middle layer, because it converts to photons in the strip layer and showers in the middle layer. Adding the energy in middle layer and strip layer for electrons candidates gives the total energy near to 180 GeV.

Figure 4.8 shows the non-electron particles energy in the LAr versus in the tile calorimeter. Left plot shows the case for run with beam energy 20 GeV and injection $\eta = 2.5$, while right plot shows the run with beam energy 180 GeV and injection $\eta = 0.25$. The events (actually particles) occupying the bottom-right parts in the plots are the pions showering only in the tile calorimeter. Particles depositing energies both in the LAr and tile calorimeter are the pions starting to shower in the LAr. Particles in the third part of the plots (bottom-left), where the deposited energies in the LAr and tile calorimeters are very small, are supposed to be muons which will be rejected by cut $E_{tile}/E_{beam} > 0.3$, where E_{tile} is the energy in the tile calorimeter and E_{beam} is

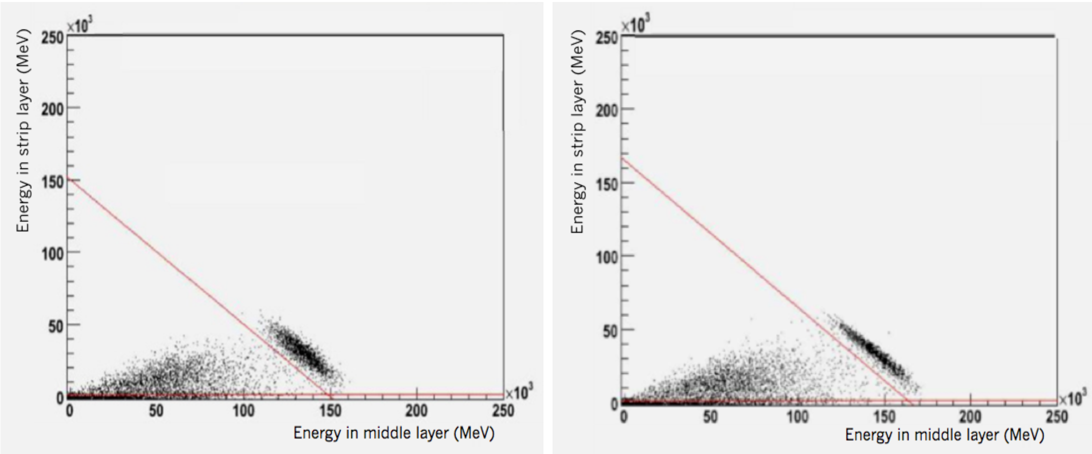

(a) (b)

Figure 4.7: Energy of particles deposit in middle layer versus in strip layer of the LAr. Left plot shows the run with beam energy 180 GeV and injection at $\eta = 0.2$, right plot shows the run with energy 180 GeV and injection at $\eta = 0.25$.

the measured beam momentum.

To get the response of pions in the calorimeter, several criteria for selecting good beams are applied.

- ADC counts in the trigger scintillator S1, S2_down and S3. The requirements for different runs are different according to the distribution of the ADC counts in the scintillators. Distributions of different scintillators in the same run are different. The typical cut value for S1, S2_down, S3_left and S3_right are $<\sim$ 1000, $<\sim$ 1300, $<\sim$ 800 and $<\sim$ 800, respectively.

- Beam position in beam chambers BC0, BC1 and B2 in the x and y directions are required to be within one sigma of the mean position of the beam. Different runs have different beam position cuts according the to particles position recorded by the beam chambers.

- Relative beam position between BC0 and BC1 (and BC1 and BC2) in the x and y direction are required to be within one sigma of the mean relative position. This is realized by getting the distribution of difference in the particle position in BC0 and BC1 (and BC1 and BC2) and then getting the mean and the sigma of the distribution.

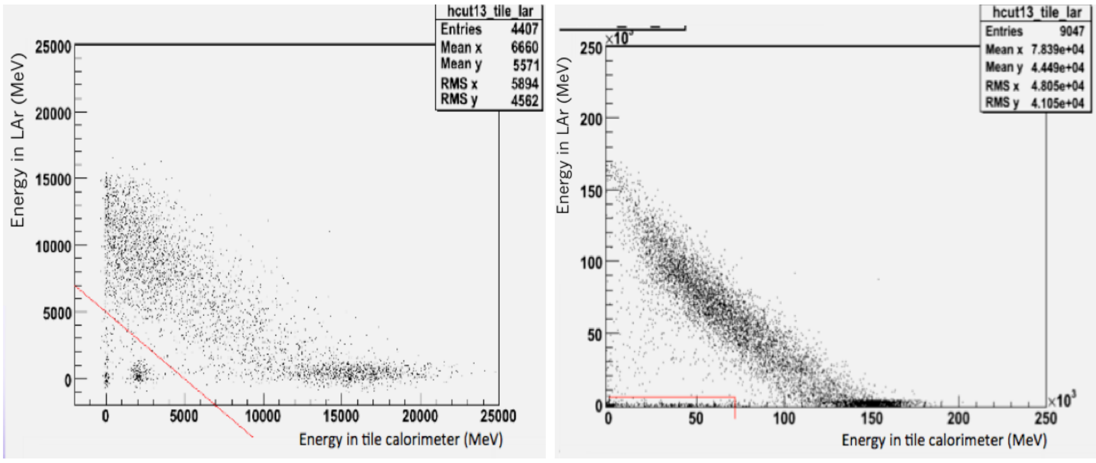

(a) (b)

Figure 4.8: Energy of particles deposit in the LAr versus in the tile calorimeter. Left plot shows the run with beam energy 20 GeV and injection $\eta = 0.25$, right plot shows the run with energy 180 GeV and injection $\eta = 0.25$.

- Muon tag from SMV is used to reject muons.

After the beam quality requirements, cuts are applied to reject electrons and muons and get pure pions. To reject electrons E_{lar}/E_{total} is required to be < 0.98. To reject muons E_{total}/E_{beam} is required to be > 0.3. In addition, number of cells in LAr are required to be > 0 to avoid the timing problem in the event.

Figure 4.9 shows the total energy of pions deposit in the LAr and tile calorimeter, where the beam is positive charged with energy of 150 GeV and injection $\eta = 0.25$. The total energy is fitted with a Gaussian distribution that gives a fit probability around 0.079.

To get the pions response in the calorimeter, runs with the same injection energy and η are combined together. The combined total energy in the LAr and tile calorimeter and its uncertainty are obtained through formula:

$$\mu_{E_{total}} = \frac{1}{w}\sum_{i}^{N} w_i \cdot \rho_i \tag{4.2}$$

$$\delta_{E_{total}} = \frac{1}{\sqrt{w}} \tag{4.3}$$

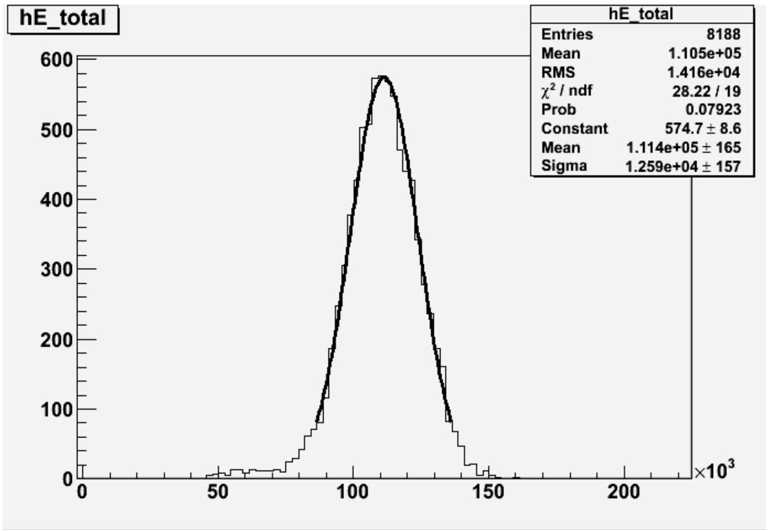

(a)

Figure 4.9: Total energy distribution of pion in the LAr and tile calorimeter. The distribution is fitted with Gaussian that gives a fit probability around 0.079. This is an example, where the run is positive particles run with beam energy 150 GeV and injection $\eta = 0.25$.

where ρ_i and δ_i are the total energy and its uncertainty for the i^{th} run, N is the total number of runs with the same energy and injection η, $w_i = \frac{1}{\delta_i{}^2}$ and $w = \sum_i^N w_i$.

The pion response in the LAr and tile calorimeter with respect to the beam energy are shown in figure 4.10 for the π^+, while figure 4.11 for the π^-. Point at beam energy 150 (250) GeV and η 0.2 (0.45) are missing because these runs have time problem. Points at beam energy 320 GeV are missing due to technical problem. The response for π^+ varies from 62% to 76% with lower response for lower energy, while the response for π^- varies from 75.5% to 78.5%. Comparing the overlapped beam energy from 150 to 180 GeV,π^- shows higher response because π^- beams have no proton contamination which gives lower energy response in the calorimeter.

The resolution of energy response of pions in the LAr and tile calorimeter with respect to the beam energy are shown in figure 4.12 for π^+, while figure 4.13 shows for π^-. Linear relation is shown for the response with respect to the $\sqrt{E}$, where E is the beam momentum measured using beam chambers on the beam line. The resolution for π^+ (π^-) response varies from 0.11 to 0.26 (0.1 to 0.14) for different η direction. Higher

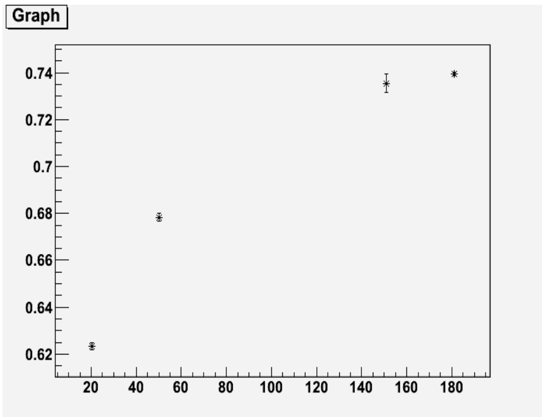

(a)

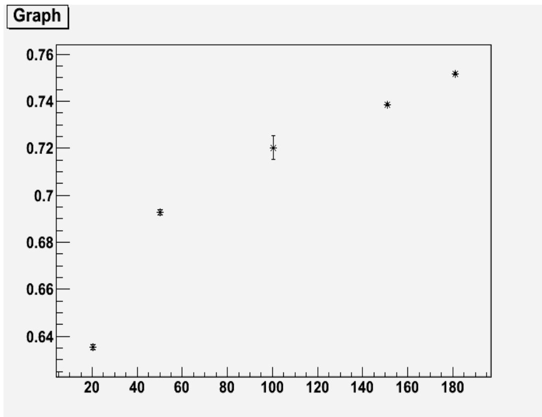

(b)

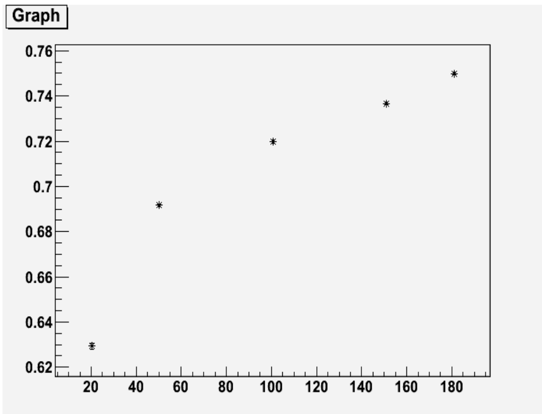

(c)

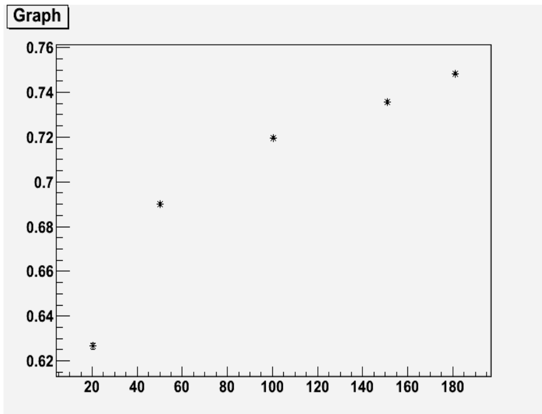

(d)

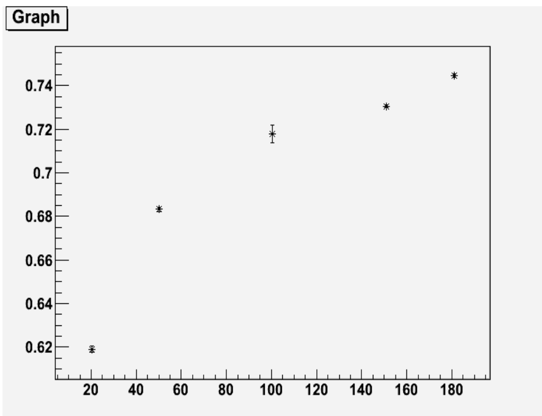

(e)

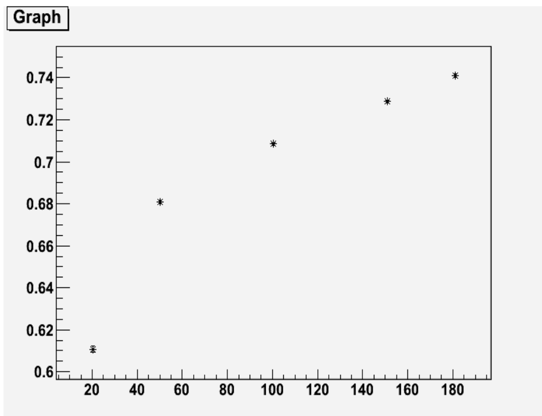

(f)

Figure 4.10: The π^+ energy response in the LAr and tile calorimeter with respect to the beam energy at fixed η. a) $\eta = 0.2$, b) $\eta = 0.25$, c) $\eta = 0.35$, d) $\eta = 0.45$, e) $\eta = 0.55$ and f) $\eta = 0.65$. **The X axis is the nominal beam energy, Y axis is the energy response.**

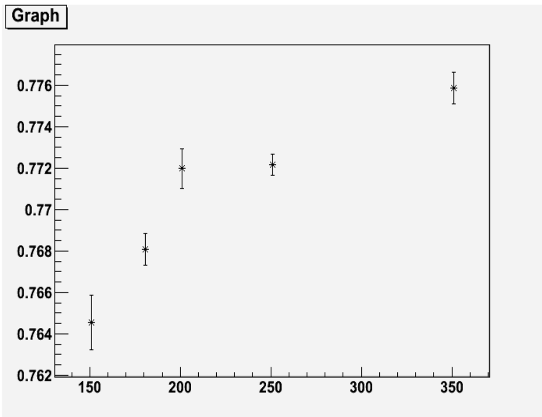

(a)

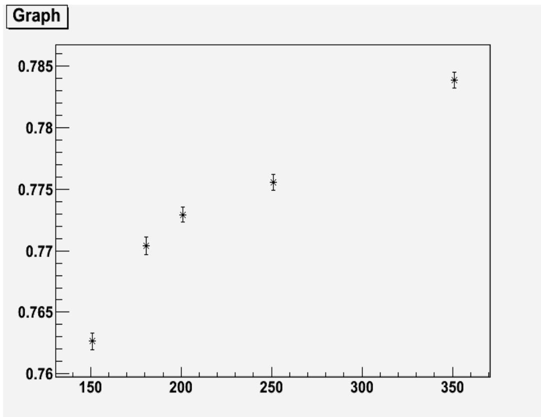

(b)

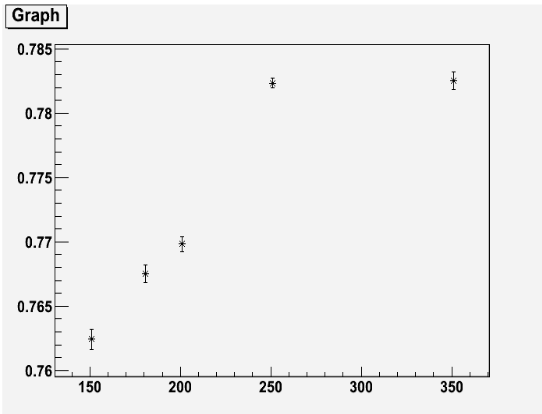

(c)

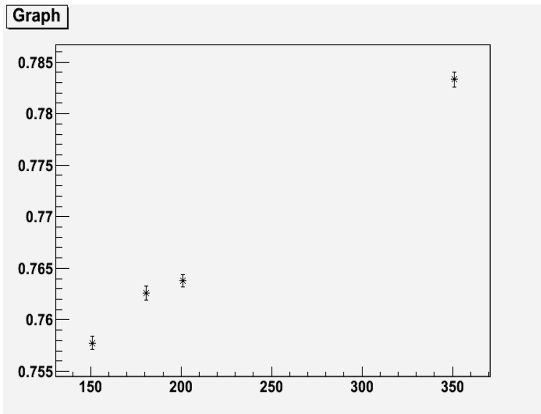

(d)

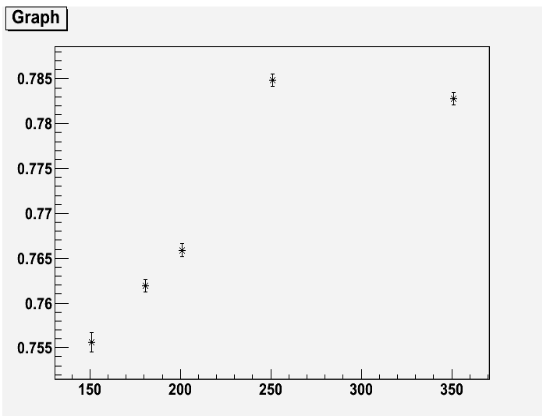

(e)

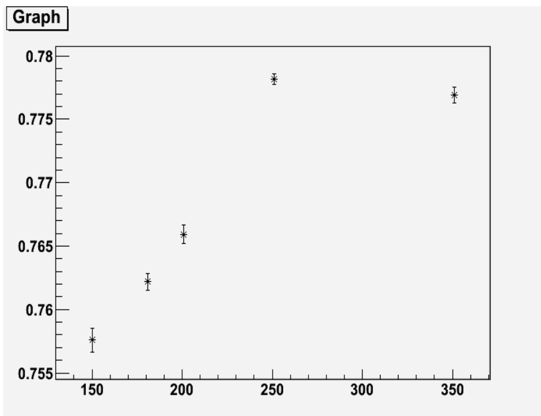

(f)

Figure 4.11: The π^- energy response in the LAr and tile calorimeter with respect to the beam energy at fixed η. a) $\eta = 0.2$, b) $\eta = 0.25$, c) $\eta = 0.35$, d) $\eta = 0.45$, e) $\eta = 0.55$ and f) $\eta = 0.65$. **The X axis is the nominal beam energy, Y axis is the energy response.**

beam energy shows better response resolution.

4.6 Summary

Test beam data collected in 2004 is analyzed. In the VLE analysis work, the noise of every cell has been studied. The noise study for the calorimeter is the first work to get the correct energy of particles. The average noise value of each layer has been found to be: 12 MeV in the presampler, 12 MeV in the first layer, 28 MeV in the second layer and 22 MeV in the third layer of the LAr, 30 MeV in the first layer, 30 MeV in the second layer and 25 MeV in the third layer of the tile calorimeter.

In the HE analysis work, the timing (cell-time to trigger-time offset) of the LAr cells has been obtained by requiring at least 2.5 GeV of energy deposition in the cell and proved to be within 5 ns for good runs. This work is important because the correct energy reconstruction of the LAr is largely dependent on the timing.

The calorimeter response and energy resolution to pions in the EM and hadronic calorimeter is studied. It is the first step to know the hadrons response in the calorimeter with know type of particles and energy. Since hadronically decay τ lepton is important at ATLAS, and the production of hadronically decay τ lepton is mainly pion(s), study of the response and shower shape is important for the τ lepton research. Low energy resolution has been improved using topo-clusters. In addition, calorimeter response to HE pions increases with the injection energy and slightly different from their η positions. The resolution is linear with respect to the $1/\sqrt{E_{beam}}$.

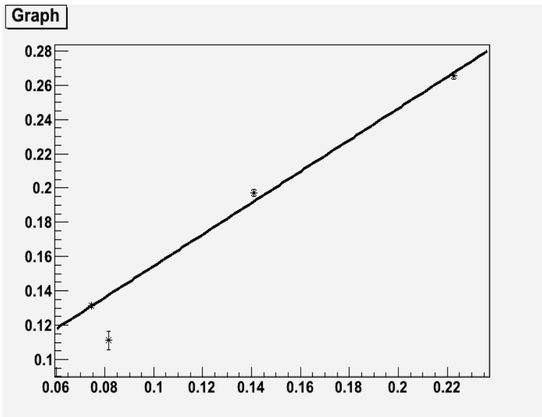

(a)

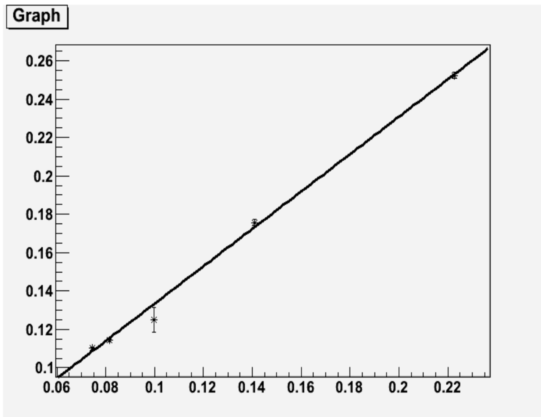

(b)

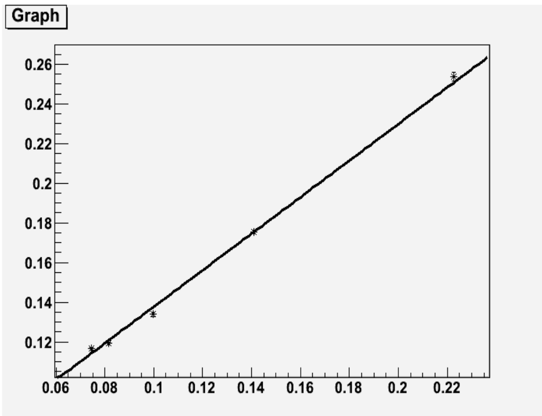

(c)

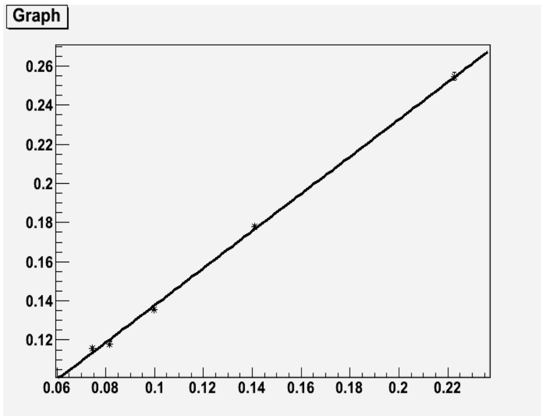

(d)

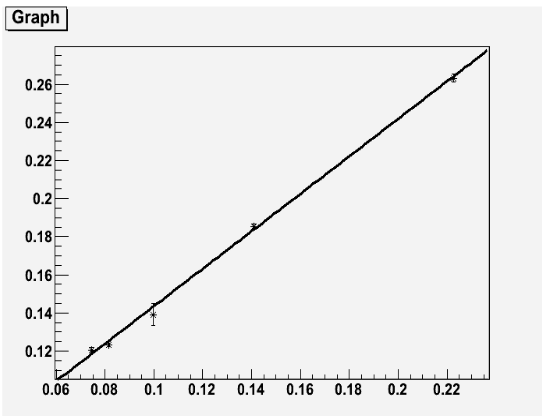

(e)

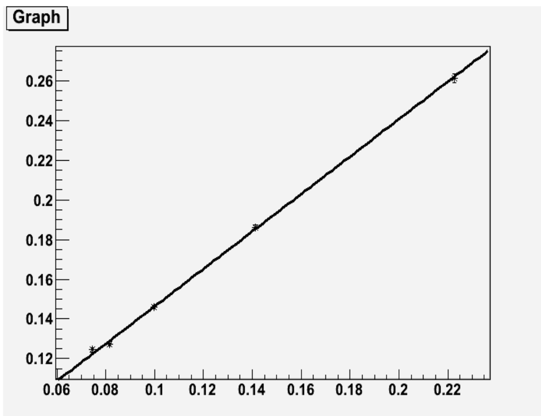

(f)

Figure 4.12: The π^+ energy resolution in the LAr and tile calorimeter with respect to the beam energy at fixed η. a) $\eta = 0.2$, b) $\eta = 0.25$, c) $\eta = 0.35$, d) $\eta = 0.45$, e) $\eta = 0.55$ and f) $\eta = 0.65$. **The X axis is $\sqrt{E}$, where E is the beam momentum measured with beam chambers on the beam line, Y axis is the energy resolution.**

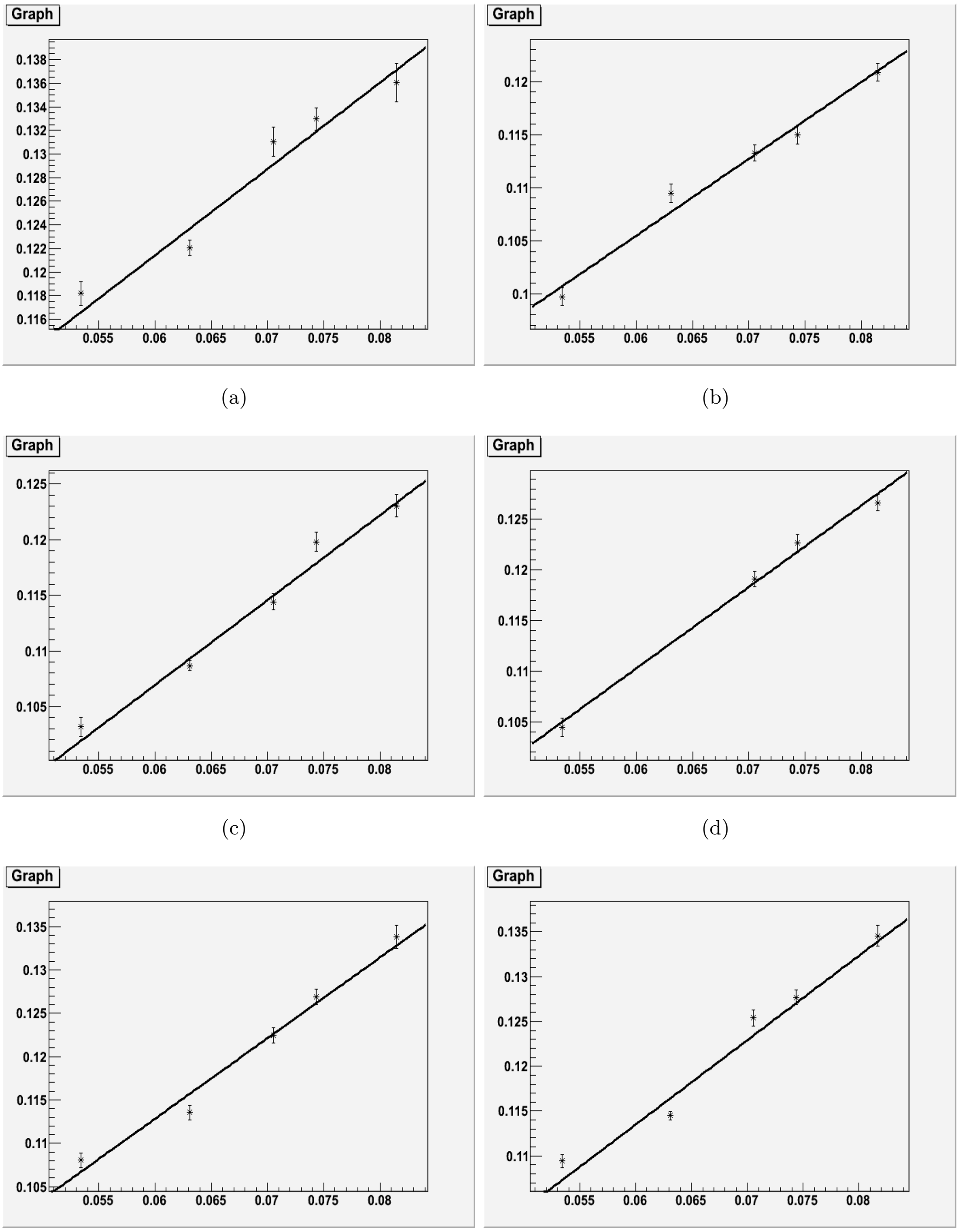

(a) (b) (c) (d) (e) (f)

Figure 4.13: The π^- energy resolution in the LAr and tile calorimeter with respect to the beam energy at fixed η. a) $\eta = 0.2$, b) $\eta = 0.25$, c) $\eta = 0.35$, d) $\eta = 0.45$, e) $\eta = 0.55$ and f) $\eta = 0.65$. **The X axis is $\sqrt{E}$, where E is the beam momentum measured with beam chambers on the beam line, Y axis is the energy resolution.**

5

Reconstruction and identification performance of the hadronic decay τ lepton at ATLAS

5.1 Introduction

As already illustrated in chapter 2, τ lepton is interesting to many processes, such as low mass Higgs boson in the SM, neutral and charged Higgs bosons in the MSSM, as well as the predicted new particles in the SUSY models and massive bosons W' and Z'. Therefore, understanding the reconstruction and identification performance of the τ lepton is very important for the new physics searches at ATLAS.

5.2 τ lepton at ATLAS

To satisfy the large range of interesting physics scenery, τ lepton has to be reconstructed and identified from low transverse energy ($\sim$ 10 GeV) to very high transverse energy ($\sim$ 500 GeV) [33]. Figure 5.1 shows the visible transverse momentum spectrum of the τ leptons under different energy scale depending on the theory models [33].

τ is a lepton with diverse decay modes. Table 5.1 illustrates the dominant decay modes of τ lepton in the analysis. More detailed information, including rare decays, is illustrated in PDG live page [1]. Here only some of the important τ^- decay modes are shown. According to the charge conservation and the lepton number conservation, the number of charged products must be odd and one τ neutrino in the final states

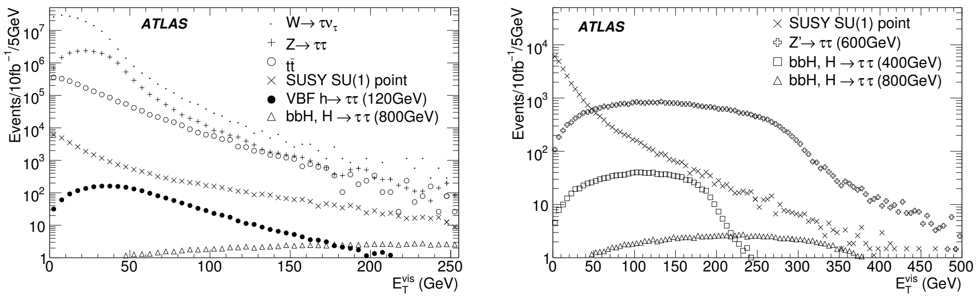

Figure 5.1: The visible transverse energy of τ leptons from different physics processes.

is required. It decays to leptons, including electron plus electron neutrino or muon plus muon neutrino, with $\sim$ 35% probability. The remaining 65% decay probability is hadronical, where $\sim$ 49% is with 1 charged particle (1-prong) and $\sim$ 15% with 3 charged particles (3-prong). In the hadronic decay modes, sometimes, one or more neutral particles are produced where, in most cases, the neutral particles are π^0s as shown in the table. 5-prong or 7-prong decay is less than 1%. Due to larger tracks multiplicity and wider distribution of the shower shape because of less energy assigned to every objets, 5-prong and 7-prong decay will suffer from more QCD background. At ATLAS, only 1-prong and 3-prong decay modes are considered.

Reconstruction and identification of τ leptons is referring hadronically decayed modes. Because its leptonic decay modes are difficult to be distinguished from original electrons and muons. To reconstruct and identify hadronically decaying τ leptons, both inner-detector trackers and calorimeters information are used. We denote the visible part of hadronically decaying τ lepton as τ_{had} to distinguish with τ lepton.

5.3 The ATLAS detector for τ leptons

5.3.1 Tracking performance

As shown in table 5.1, the most important decay modes are the ones with charged pion(s) in the final states. The ATLAS inner-detector is used to reconstruct tracks from charged particles by finding the correlated hits on different layers. To avoid mis-recontruction and mis-identification (fake tracks) from the track reconstruction

Modes with 1 charged particle		
Products	Branching Rario (%)	
$e^-\nu_e\nu_\tau$	17.85 ± 0.05	Leptonic decay modes
$\mu^-\nu_e\nu_\tau$	17.36 ± 0.05	
$h^-\nu_\tau$	11.61 ± 0.06	Hadronic decay modes
$\pi^-\nu_\tau$	10.91 ± 0.07	
$h^-neutral(s)\nu_\tau$	37.06 ± 0.10	
$h^-\pi^0(s)\nu_\tau$	36.54 ± 0.11	
$\pi^-\pi^0\nu_\tau$	25.51 ± 0.09	
$\pi^-2\pi^0\nu_\tau$	9.29 ± 0.11	
$\pi^-3\pi^0\nu_\tau$	1.04 ± 0.07	
Modes with 3 charged particels		
Products	Branching Rario (%)	
$h^-h^-h^+\nu_\tau$	9.80 ± 0.08	Hadronic decay modes
$\pi^-\pi^-\pi^+\nu_\tau$	9.32 ± 0.07	
$h^-h^-h^+neutral(s)\nu_\tau$	5.38 ± 0.07	
$h^-h^-h^+\pi^0(s)\nu_\tau$	5.08 ± 0.06	
$\pi^-\pi^-\pi^+\pi^0\nu_\tau$	4.48 ± 0.06	

Table 5.1: The decays modes of τ leptons

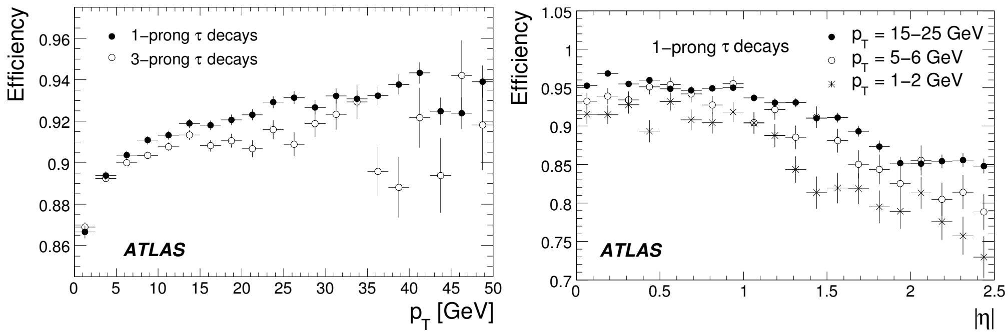

(a) a (b) b

Figure 5.2: Reconstruction efficiency for tracks from charged πs for one- and three-prong hadronic τ decays from $W \to \tau\nu$ and $Z \to \tau\tau$ signal samples as a function of the transverse momentum of the track (left) and of the pseudo-rapidity for three different ranges of track p_T (right).

algorithm, several qualities are applied to select good tracks at the reconstruction level of the τ leptons. These criteria are illustrated in section 5.4.4.

Tracking efficiency for τ_{had} is defined as the probability that a truth track of charged pion is reconstructed as a track and passes the criteria. Figure 5.2 shows the standard track selection efficiency with respect the transverse momentum and pseudo-rapidity from tracking performance work group in 2008. The track criteria for τ_{had} is tighter than the standard ones, so the efficiency is lower as shown in figure 5.2 [33].

5.3.2 Vertex reconstruction

The decay length of τ lepton is long enough ($87.11\mu m$) for producing a secondary vertex, and it is possible to be reconstructed and identified using the ATLAS inner-detector. To distinguish a secondary vertex, beam spot and primary vertex reconstruction is essential. Secondary vertex is identified according to its distance to the primary vertex both in transverse and parallel planes. Primary vertex in principle is the vertex produced by the collision itself. With increasing instantaneous luminosity at the LHC, multi-collisions in a single bunch-crossing cannot be neglected. So several primary vertices can be reconstructed in one event. Primary vertex is defined as the most energetic one, whose $\sum(p_T^2)$ is the largest. The pile up vertices are the remaining primary vertices. Figure 5.3 shows the distance distribution of pile up vertices to the primary vertex in direction x, y and z at the ATLAS coordinate system while the pile up vertex is nearest to the primary vertex comparing to other pile up vertices in the event along beam direction. This is to give an idea about how the pile up vertices distributed around the primary vertex. The distance between in x and y direction is small, that is because pile up vertices are also distributed along beam line. The distance in z direction can be large that is because the pile up collision can be far from the primary collision. The distribution is obtained for different periods of data taking. The distance in direction x and y are smaller at high instantaneous luminosity period (e.g. period I) due to more constraint beam in LHC. Figure 5.4 shows the size of the primary vertex for directions x, y and z, while Figure 5.5 shows the pile up vertices size. The size of primary vertex is at most 0.05 mm in direction x and y, while it is at most 0.3 mm in the z direction. The resolution is worse along the beam as expected. Because the tracks in the trackers are bended in the transverse plane in magnetic field at the ATLAS and the resolutions of the inner detector in the x and y directions are designed to be better than in the z direction. The pile up vertices show worse resolution in all the directions. The primary and pile up vertices are required to have at least four associated tracks.

The secondary vertices performance has been studied by tau work group in 2008 using MC samples. Simulated $Z \to \tau\tau$ and $W \to \tau\nu$ samples are used to study the secondary vertices reconstruction performance. The track-seeded τ_{had} candidates matching to truth τ in the MC samples are separated into two categories. The first one is composed of candidates with all their three tracks passing the criteria and matching to the same true τ lepton. They are denoted as fully-matched candidates. The second category is composed of candidates with at lease two associated tracks passing the criteria and at least one of the tracks matching to a true τ_{had}. They denoted as partially-matched candidates. Figure 5.6 shows the resolution of the secondary vertices for perpendicular and parallel to the τ_{had} flight direction. More detailed study please have a look at the paper [33].

5.3.3 Calorimeter performance

Calorimeters are used to reconstruct objects shapes for their identifications. τ_{had} is a narrow jet with small particle multiplicity comparing to the real QCD jet. Shapes reconstruction in the calorimeter of the particles becomes important for the τ_{had} identification.

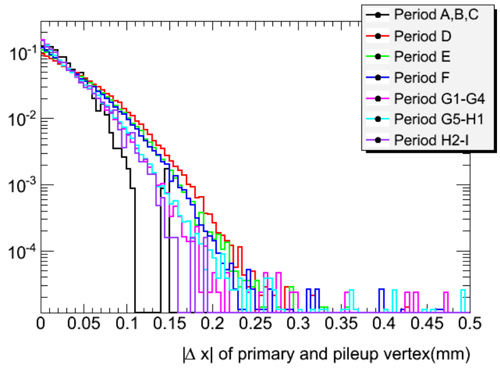

(a)

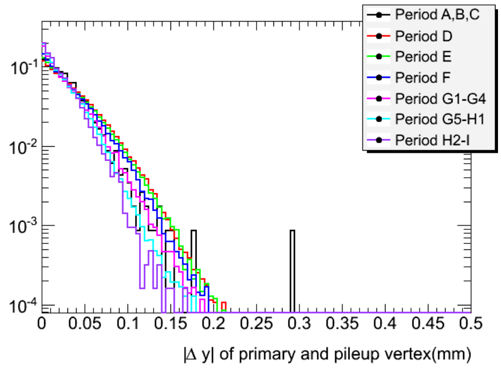

(b)

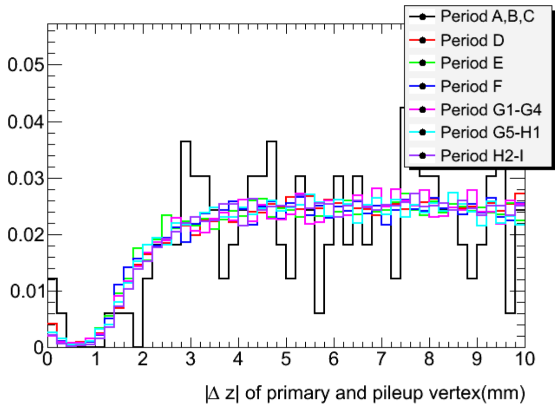

(c)

Figure 5.3: The distance between pile up vertices and primary vertex event by event in direction a) x, b) y and c) z when the pile up vertex is the nearest one to the primary vertex along beam direction in the ATLAS coordinate systerm.

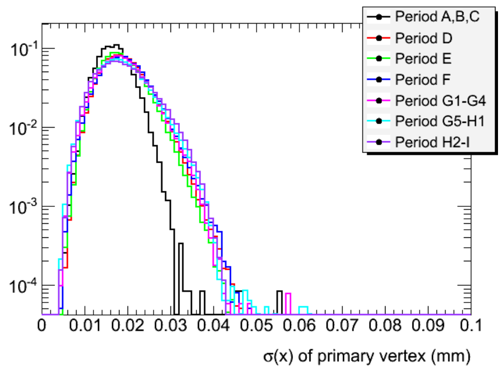

(a)

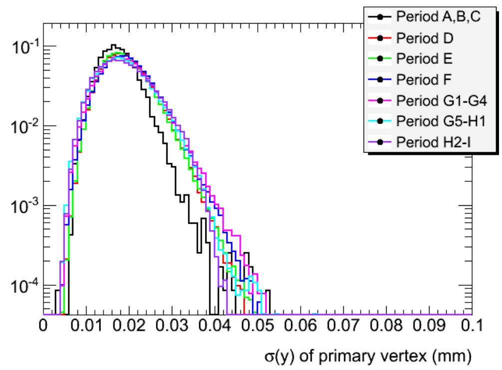

(b)

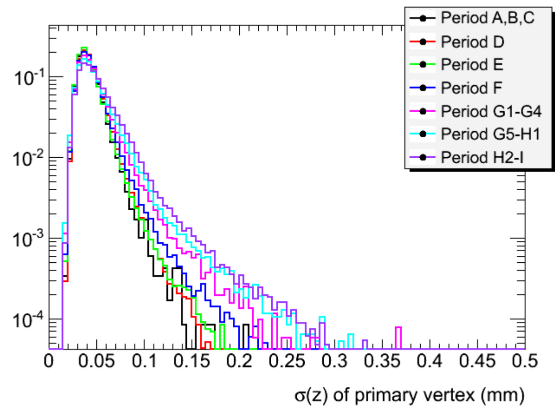

(c)

Figure 5.4: The primary vertex size in direction a) x, b) y and c) z. The vertex size is defined as the vertex fit error.

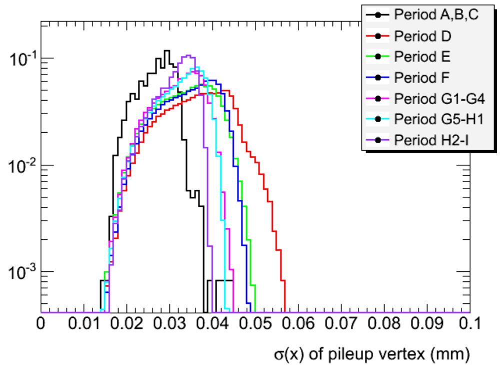

(a)

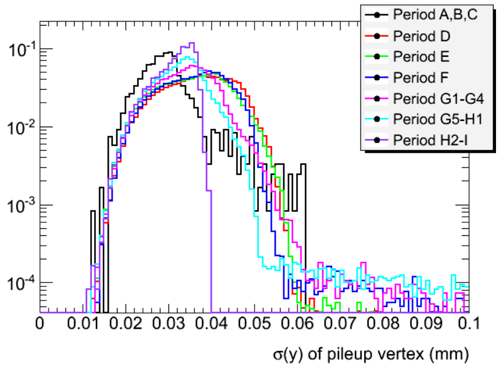

(b)

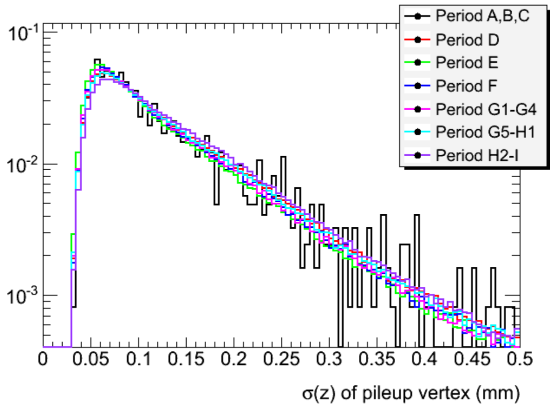

(c)

Figure 5.5: The pile up vertex size in direction a) x, b) y and c) z. The vertex size is defined as the vertex fit error.

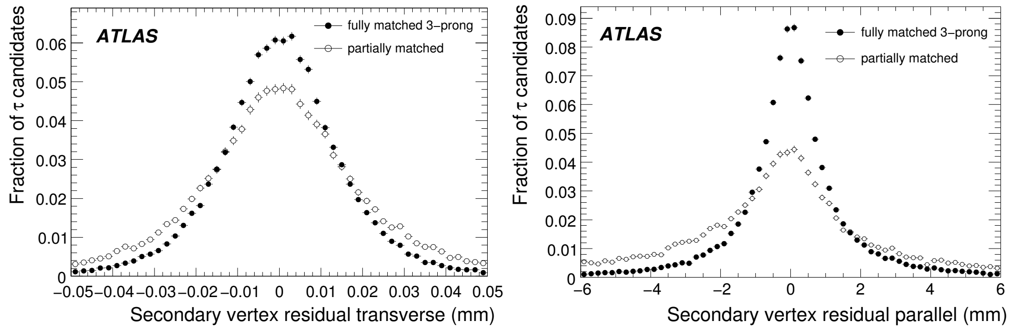

(a) a (b) b

Figure 5.6: Residuals of the secondary vertex position in the transverse plane perpendicular to the beam line (left) and in the direction along the beam line right. They are obtained using MC simulated with center-of-mass at 14 TeV. The main information these plots provide is resolution of secondary vertex along beam direction is worse than the one perpendicular to the beam direction, which is expected because of worse position measurement along beam for vertex. Also, the residuals of vertex with tracks full matched to real τ is smaller than the partially matched ones, because the partially matched vertex can have tracks not from the secondary vertex.

As shown in table 5.1, τ_{had} with π^0 in the final states are not negligible. On average, π^0s carry about 55% energy of the visible part of the τ_{had}. It is possible to reconstruct the π^0 clusters in a narrow cone due to the EM calorimeter's fine granularity, especially in the first layer.

5.3.3.1 π^0 reconstruction in τ candidates

π^0 cluster reconstruction is started from cells around the track direction with $p_T >$ 6 GeV within cone size 0.4 and only clusters within a smaller cone size 0.2 are considered. The clustering is performed through the topological clustering algorithm (The clustering starts from a energetic cell with energy $>$ 4 σ_{noise}. Neighbor cells are included in the cluster if their energy is $>$ 2 σ_{noise}. The cells search in the clustering continues until the cells carrying energy $>$ 0 σ_{noise}. Therefore, a clustering scheme is formed by searching the energetic cells around the most energetic cell with a cell energy step 420 σ_{noise} [63]). During the π^0 reconstruction, to avoid the charged particles effects to the π^0 energy, cells around the charged particle impact point at the calorimeter within cone 0.0375 are not considered. Subtraction of energy is performed until the

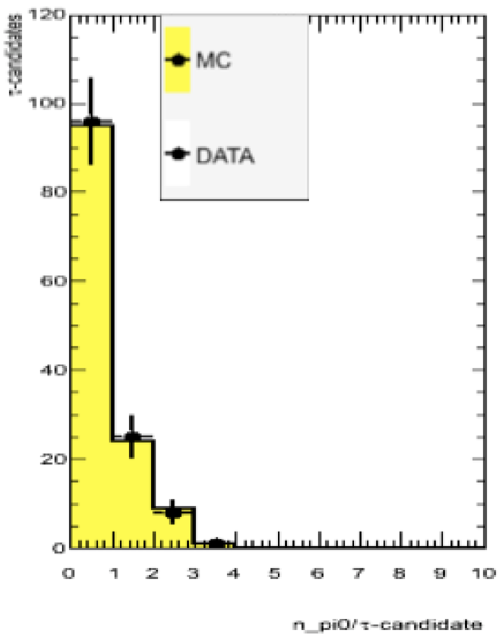

Figure 5.7: Number of the reconstructed π^0 in the τ_{had} candidates. MC agrees data within the statistic uncertainty.

total energy of cells takes 70% of the track momentum. In case track deposits more than 40% of its energy in the hadronic calorimeter and large fraction of energy are found close to the track impact point in the pre-sampler and strip layer, subtraction is performed only in the middle layer and stopped when the remaining cells transverse energy takes $2.5 \cdot E_T$ of the transverse energy collected in pre-sampler + strip layer.

Clusters are accepted if their transverse energies are greater than 1 GeV and are separated from tracks with $\Delta R > 0.0375$. Besides, clusters take more than 10% of their total energy in pre-sampler + strip layer are considered as π^0 clustered as well. Figure 5.7 shows the number of π^0 clusters. The data sample is real data collected in 2009 with center of mass energy 900 GeV.

5.3.4 Electron veto with tracker and calorimeters

Electron veto based on standard electron selection rejects most of the backgrounds from $W \to e\nu$ and $Z \to ee$, $\sim 85\%$ from the MC estimation. To improve the veto efficiency, veto algorithm within τ_{had} reconstruction and identification is implemented. The used variables are: [33, 67]:

- The energy deposited in the hadronic calorimeter (E^{HCAL}).
- The energy not associated with a charged track in the strip layer of the electromagnetic calorimeter (E^{strip}_{max}).
- The ratio in the transverse plane of the associated energy in the electromagnetic calorimeter and the track momentum (E_T/p_T).
- The ratio of the number of high threshold to low threshold hit (including outliers) in the TRT (N_{HT}/N_{LT}).

The algorithm rejects a factor of 60 against electron from $W \to e\nu$ events while keeps 95% of signal from MC $W \to \tau\nu$ sample.

5.4 τ_{had} reconstruction performance at ATLAS

Due to the huge cross-section of QCD multi-jets process in p-p collisions (at an order of barn), distinguishing τ_{had}s from real QCD jets is the most important part both at the reconstruction and identification level. Comparing to QCD jets that come from hadronization of quarks and gluons produced after inelastic collision, τs decay to charged particles are with small particles multiplicity. So τ_{had}s are narrower than QCD jets. Just because they are narrow, electron and muon can also fake as τ_{had} (section 5.3.4). Using information of muon spectrometer, fakes from muons can be decreased very much. To identify τ_{had} from electrons, hadronic calorimeter information is used. Based on these features, τ_{had} reconstruction algorithms calculate shape variables and save them, as well as energy and tracks information, preparing for τ_{had}s$^{'}$ identification.

Two algorithms are developed to reconstruct τ_{had}. The first one is calo-seeded, that uses a jet as the seed. The second one is track-seeded, that uses a track as the seed. If the two seeds are matched within $\Delta R < 0.2$, the τ_{had} candidate is double-seeded. Therefore, τ_{had} candidates can be divided into three categories according to the two algorithms: track-only-seeded candidates, calo-only-seeded candidates and double-seeded candidates.

5.4.1 Calo-seeded reconstruction algorithm

The seed in this algorithm is a jet with cone size 0.4 reconstructed by Anti-Kt algorithm with $p_T > 10\ GeV$ and the jet reconstruction is from topological clusters. Tracks are found around the jet direction, which pass the track criteria (see section 5.4.4). Reconstruction of the shower shapes of the objects is then performed using dedicating algorithms based on calorimeters information. These variables are commissioned both at low center-of-mass energy $\sqrt{s} = 900\ GeV$ and high center-of-mass energy $\sqrt{s} = 7\ TeV$. The commissioning is based on good collisions in the data from the Minimum-Bias stream. The common selections are: good collisions are presented by requiring tracking and calorimeter systems are in good status. In the 900 GeV data samples, at lease one calo-seeded τ_{had} candidate with un-calibrated transverse momentum $p_T > 7\ GeV$ is required, the associated track criteria are: $|d_0| < 1.5\ mm$, $|z_0| \cdot \sin(\theta) < 1.5\ mm$, number of Pixel hits ≥ 1 and number of SCT hits ≥ 6, the tracks are found around candidates within a cone $\Delta R < 0.2$ or $\Delta R < 0.3$ for candidates with or without seed track [67]. In the 7 TeV data samples, further selections are applied by requiring a jet trigger with threshold of 5 GeV, no "bad" jet in the event and at least two back-to-back ($|\Delta\phi| > 2.7$ to select good τ_{had} candidates) and τ_{had} candidates with $p_T > 15\ GeV$; the associated track selection are: $|d_0| < 2\ mm$, $|z_0| \cdot \sin(\theta) < 10\ mm$ and number of Silicon hits (number of Pixel hits plus number of SCT hits) ≥ 7 [68]. MC shapes are normalized to the data in the plots. The MC used in the commissioning are generated with Pythia at 900 GeV and 7 TeV, respectively. They are simulated with Geant4 and reconstructed under Athena release 15. The shower shapes variables that are important for the identification are illustrated below, with some of the plots for 7 TeV overlaid with MC signal τ_{had} from $Z \to \tau\tau$ sample. The variables show discrimination power of τ_{had} from QCD multi-jets according to that signal τ_{had} is narrower than QCD jet.

- **The electromagnetic radius R_{EM}:**

  It is the transverse energy weighted radius defined as:

$$R_{EM} = \frac{E_{T,i} \sum_{i=1}^{\Delta R_i < 0.4} E_{T,i}^{EM}}{\sum_{i=1}^{\Delta R_i < 0.4} E_{T,i}^{EM}}, \tag{5.1}$$

  where i runs over all the cells around the seed direction within distance $\Delta R < 0.4$ in the electromagnetic calorimeter except the last layer, $E_{T,i}$ is the

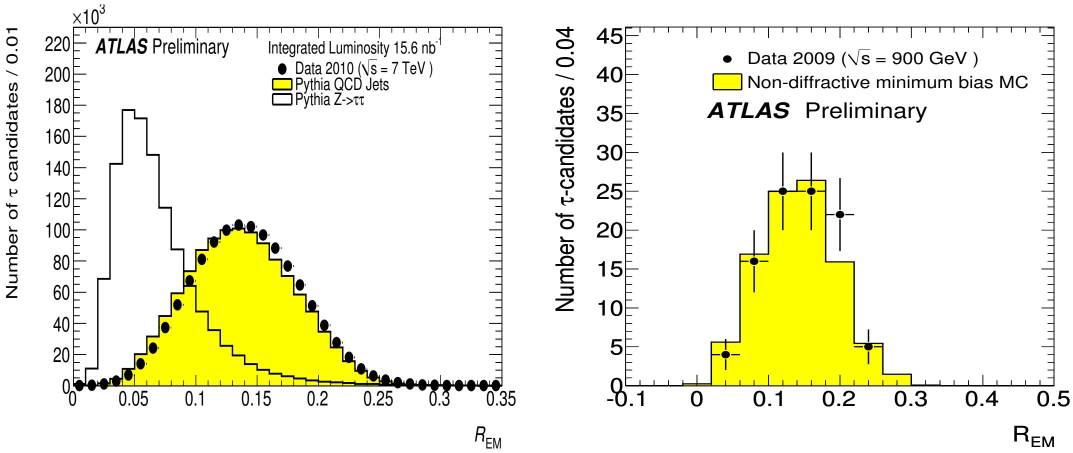

(a) (b)

Figure 5.8: Transverse energy weighted radius in the electromagnetic calorimeter, commissioning with center-of-mass energy at a) 7 TeV and b) 900 GeV collision data.

uncalibrated energy projected to transverse plane for cell i and ΔR_i is the distance of cell i to the seed direction [33].

Most of the cases, τ leptons are boosted to high energy at ATLAS. Therefore, τ_{had}s are well collimated. Due to the small particle multiplicity, τ_{had}s are narrower than QCD jets on average. It is expected that τ_{had} takes most of its energy in the core region ($\Delta R < 0.1$ around the seed direction). Therefore, R_{EM} is smaller for τ_{had} candidates comparing to jets. Since QCD jets become narrower with their transverse momentum, the identification power of this variable will be weakened.

It is a powerful variable to distinguish τ_{had} and QCD jets, because electromagnetic granularity is fine enough to use the width for exacting τ_{had} from QCD jets. Figure 5.8 shows the R_{EM} distribution comparing data and MC samples for center-of-mass energy of $\sqrt{s} = 7$ TeV (left) and $\sqrt{s} = 900$ GeV (right). Data is slightly wider than MC, which is due to underling events are not modeled well in the generator. In the right plot, τ signal from $Z \rightarrow \tau\tau$ MC sample is overlaid, where the expected signal is narrower comparing the background.

- **The central energy fraction f_{cent}, or denoted as f_{core}**

  It is the transverse energy fraction in the central (core) region of τ_{had} candi-

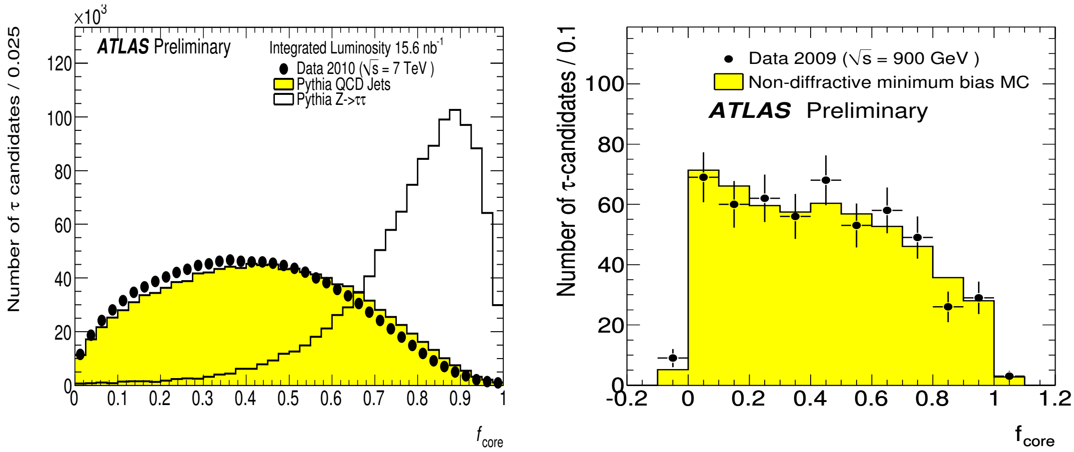

(a) (b)

Figure 5.9: Fraction of energy deposited in the core region of τ_{had} candidate commissioning with center-of-mass energy at a) 7 TeV and b) 900 GeV collision data.

dates. It is defined as:

$$f_{cent} = \frac{\sum_{i=1}^{\Delta R_i<0.1} E_{T,i}}{\sum_{j=1}^{\Delta R_j<0.4} E_{T,j}}, \tag{5.2}$$

where i, j runs over all the cells around the seed direction within distance $\Delta R < 0.1$ and $\Delta R < 0.4$ respectively in the calorimeters, $E_{T,i}$ and $E_{T,j}$ are the energy projected to transverse plane for cell i and j and $\Delta R_{i,}$ is the distance of cell i, j to the seed direction.

f_{cent} is larger for τ_{had} comparing to QCD jets. Figure 5.9 shows the f_{cent} distribution comparing data and MC samples at $\sqrt{s}$ =7 TeV (left) and 900 GeV (right). Data shows smaller value comparing to MC samples.

- **The transverse energy in the calorimeter over the leading track transverse momentum E_T/p_T:**

  Comparing to QCD jets, leading track in τ_{had} is more harder. Since π^0(s) are produced in most of the decay cases, E_T/p_T is larger than 1 in most of the cases but smaller than QCD jets. Figure 5.10 shows the E_T/p_T distribution comparing data and MC samples at center-of-mass energy 7 TeV (left) and 900 GeV (right). Data and Monte Carlo agree with each other very well especially for 7 TeV samples.

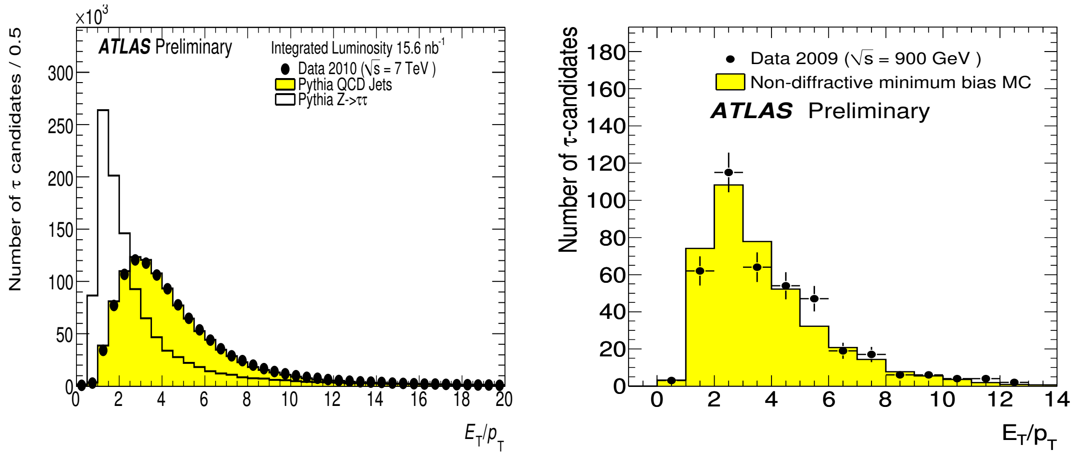

(a) (b)

Figure 5.10: τ_{had} candidate transverse energy over leading track p_T, compared at center-of-mass energy a) 7 TeV and b) 900GeV.

- **The cluster mass $m_{clusters}$:** The invariant mass of the τ_{had} candidate calculated from associated topo-clusters.

  It is smaller for τ_{had} candidates than QCD jets because QCD jets are from parton hadronization. Figure 5.11 shows the $m_{clusters}$ distribution comparing data and MC samples for center-of-mass energy at $\sqrt{s} = 7\ TeV$ (left) and $\sqrt{s} = 900\ GeV$ (right). Very small difference found between data and MC, where data shows slightly large mass from cluster.

- **Track Radius R_{track}:**

  It is transverse momentum weighted track width calculated from tracks system similar to R_{EM}. Its definition is illustrated in the equation below:

$$R_{track} = \frac{\sum_i^{\Delta R_i < 0.2} p_{T,i} \Delta R_i}{\sum_i^{\Delta R_i < 0.2} p_{T,i}}, \tag{5.3}$$

  where i runs over all tracks associated to the τ_{had} candidate, ΔR_i is referred to the seed jet direction and $p_{T,i}$ is the transverse momentum of the i^{th} associated track.

  τ_{had} candidates are narrower and less charged particle multiplicity comparing to QCD jets. Therefore, of R_{track} is smaller for τ_{had} candidate than QCD jet. Left

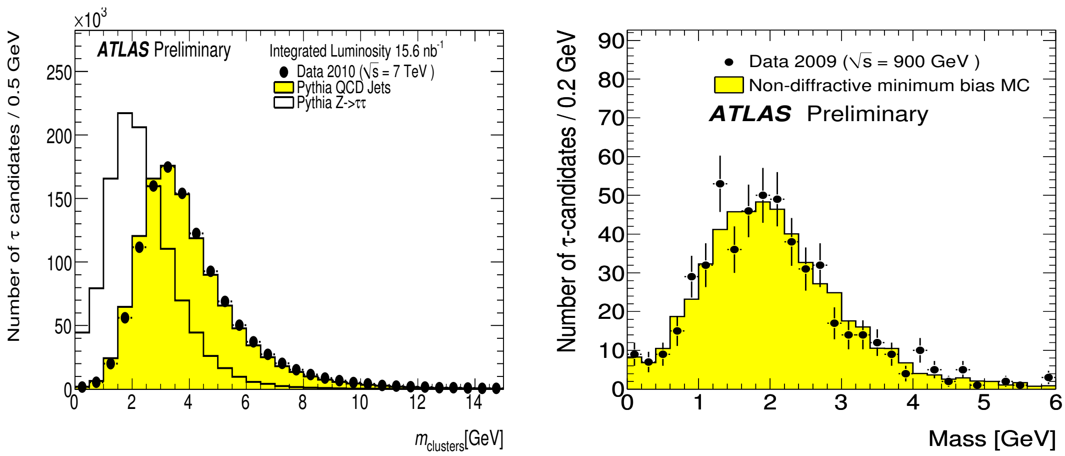

(a) (b)

Figure 5.11: Invariant mass of τ_{had} calculated from associated topoclusters for a) 7 TeV and b) 900 GeV data.

plot of figure 5.12 shows the R_{track} distribution comparing data and MC samples for center-of-mass energy at . Shape for Monte Carlo shows slightly narrower than data.

- **The track mass m_{tracks}:** The mass of the τ candidate reconstructed from associated tracks.

  The variable is the same as the $m_{clusters}$ but measured independently with track system, providing a cross-check to the calorimeter based mass and less effect by the pileup while only consider the tracks at one vertex. Figure 5.12 shows the m_{tracks} distribution comparing data and MC samples for $\sqrt{s} = 7$ TeV. Data and MC are found to agree with each other very well.

- **The Electromagnetic fraction f_{EM}:** The energy fraction of τ_{had} candidate deposited in electromagnetic calorimeter.

  The energy of the candidate is GCW (Global Cell-energy-density Weighting calibration scheme) calibrated. f_{EM} is defined as below:

$$f_{EM} = \frac{\sum_i^{\Delta R_i < 0.4} E_{T,i}^{GCW}}{\sum_j^{\Delta R_i < 0.4} E_{T,j}^{GCW}}, \tag{5.4}$$

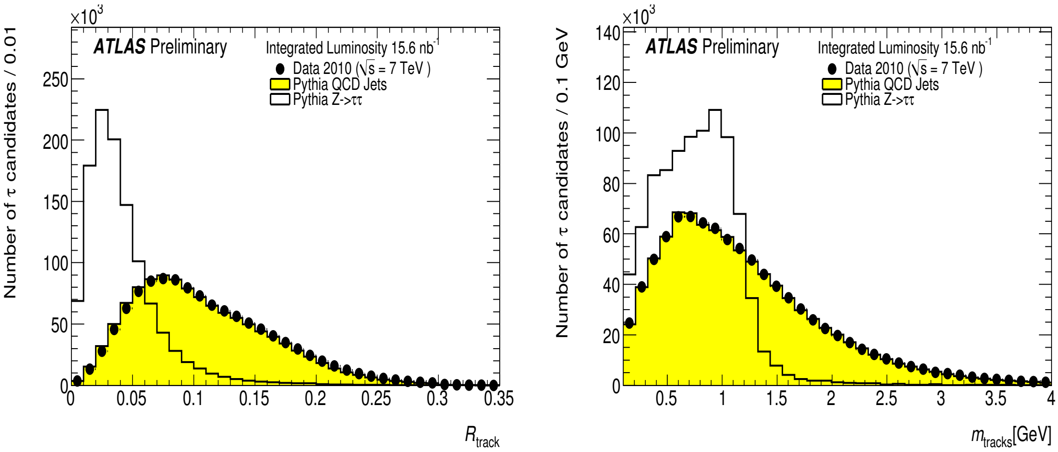

(a) (b)

Figure 5.12: Left plot shows the data and MC comparison for transverse momentum weighted radius from τ_{had} associated tacks system. Right plots shows the data MC comparison for invariant mass calculated from τ_{had} associated tacks system.

where i runs over all the cells in the electromagnetic calorimeter except the back layer, j runs over all the cells in the calorimeters including electromagnetic and hadronic ones. $E_{T,i}$ and $E_{T,j}$ are the transverse energy measured in cell i and j respectively.

QCD jets deposits its energy mainly in the hadronic calorimeter, while τ_{had} is companied by π^0(s) and deposit more energy in the EM calorimeter. Therefore, f_{EM} is expected larger for τ_{had}. Figure 5.13 shows the f_{EM} distribution comparing data and MC samples for center-of-mass energy $\sqrt{s} = 7$ TeV (left) and $\sqrt{s} = 900$ GeV (right). Slight different found between data and MC.

- **The hadronic radius R_{had}**

It is the energy weighted radius in the hadronic calorimeter (including the last layer of EM camlorimeter). It is defined as:

$$R_{had} = \frac{\sum_{i=1}^{\Delta R_i < 0.4} E_{T,i}^{had} \Delta R_i}{\sum_{i=1}^{\Delta R_i < 0.4} E_{T,i}^{had}}, \tag{5.5}$$

where i runs over all the cells around the seed direction within distance $\Delta R < 0.4$ in the hadronic calorimeter and the back layer of electromagnetic

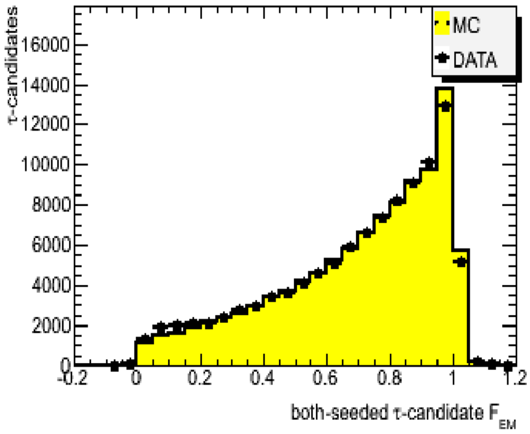

(a)

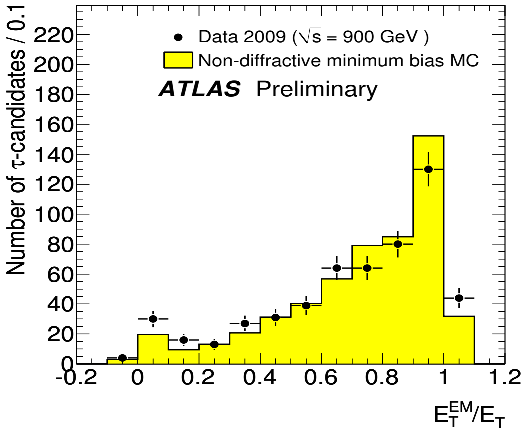

(b)

Figure 5.13: Left plot show the fraction of τ_{had} energy in the electromagnetic calorimeter at center-of-mass energy 7 TeV, calo-only-seeded candidates is shown only. Right plot shows the f_{EM} at center-of-mass energy 900 GeV for calo-seeded candidates.

calorimeter, $E_{T,i}$ is the energy projected to transverse plane for cell i and ΔR_i is the distance of cell i to the seed direction.

R_{had} is smaller for τ_{had} candidates comparing to QCD jets. Because the granulation of hadronic calorimeter are rougher than EM calorimeter, R_{had} is not used in τ_{had} identification for the data collected in 2010.

Figure 5.14 shows the R_{had} distribution comparing data and MC samples. Left is for center-of-mass energy $\sqrt{s}$ = 7 TeV and right is for 900 GeV.

- **The isolation fraction f_{ring}:**

It is the transverse energy fraction of τ_{had} in the isolation region (ring of $0.1 < \Delta R < 0.2$ around the seed direction). It is defined as:

$$f_{ring} = \frac{\sum_{i=1}^{0.1<\Delta R_i<0.2} E_{T,i}}{\sum_{j=1}^{\Delta R_j<0.4} E_{T,j}}, \tag{5.6}$$

where i, j runs over all the cells around the seed direction within distance $0.1 < \Delta R < 0.2$ and $\Delta R < 0.4$ for the numerator and dominator respectively in the calorimeters. $E_{T,i}$ and $E_{T,j}$ are the energy projected to transverse plane for cell i and j and ΔR_i is the distance of cell i to the seed direction.

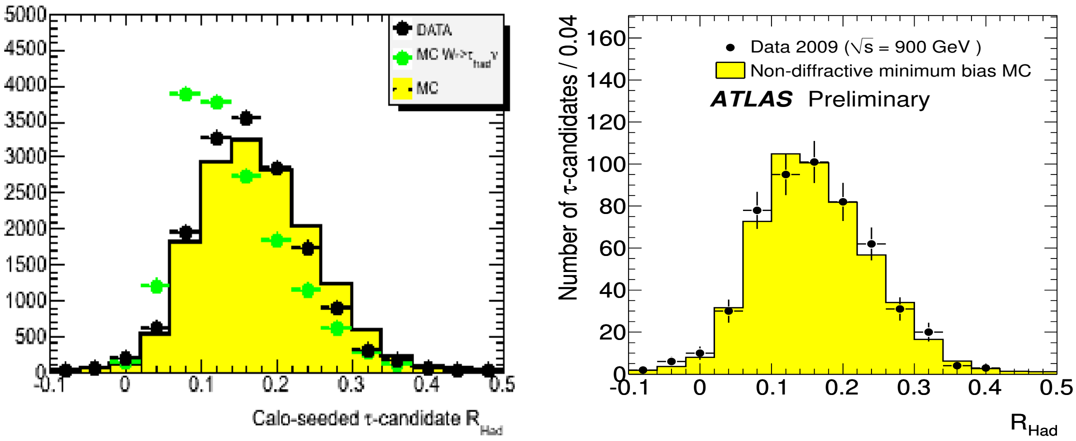

(a) (b)

Figure 5.14: Left plot shows the transverse energy weighted radias in the hadronic calorimeter. Green points illustrate the R_{had} for the τ_{had} from $W \rightarrow \tau_{had}\nu$ MC. The selection is a little different from the commissioning study, so the difference is a little larger comparing to other variables like R_{EM} in the 7 TeV samples. Right plot shows the R_{had} at 900 GeV. Both plots are for calo-seeded candidates.

Thanks to the collimation of τ_{had}, f_{ring} is expected to be smaller than QCD jets. It is less sensitive to cell noise, because the effect is weakened by cancelation between the dominator and numerator. Figure 5.15 shows the f_{ring} distribution comparing data and MC samples. Left is for center-of-mass energy $\sqrt{s} = 7\ TeV$ and right is for $\sqrt{s}$ = 900 GeV.

- **Number of hits in the η strip layer N_{strip}:** Finely segmented in η direction in the strip layer of electromagnetic calorimeter is utilized here to reconstruct a variable used for τ_{had} identification. N_{strip} is the number of cells with energy at least 200 MeV in η direction within cone size 0.4 around the seed jet direction.

  5.16 shows the N_{strip} distribution comparing data and MC samples. Here only the comparing for data and MC with $\sqrt{s} = 900\ GeV$ is shown. The selection is different from the commissioning study where more cleaning event selection was applied. Besides, at the early stage of data taking when the ATLAS detector was not understood, the difference between data and MC was acceptable.

  N_{strip} used to identify τ decay modes without neutral particles, such as $\tau \rightarrow \pi\nu$.

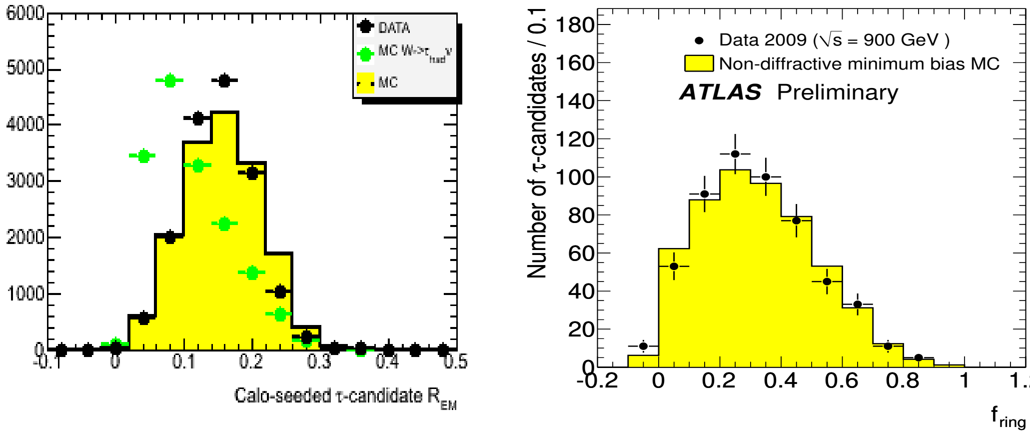

(a) (b)

Figure 5.15: Left plot shows isolation fraction in the calorimeter. Green points are R_{had} for the τ_{had} from $W \rightarrow \tau_{had}\nu$ MC. The selection is a little different from the commissioning study, so the difference is a little larger comparing to 900 GeV case. Right plot shows the R_{had} at 900 GeV. Both plots are for calo-seeded candidates.

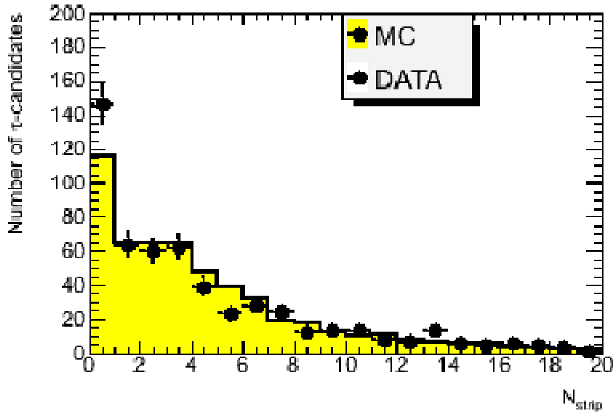

(a)

Figure 5.16: N_{strip} distribution of data and MC compared for 900 GeV collision data.

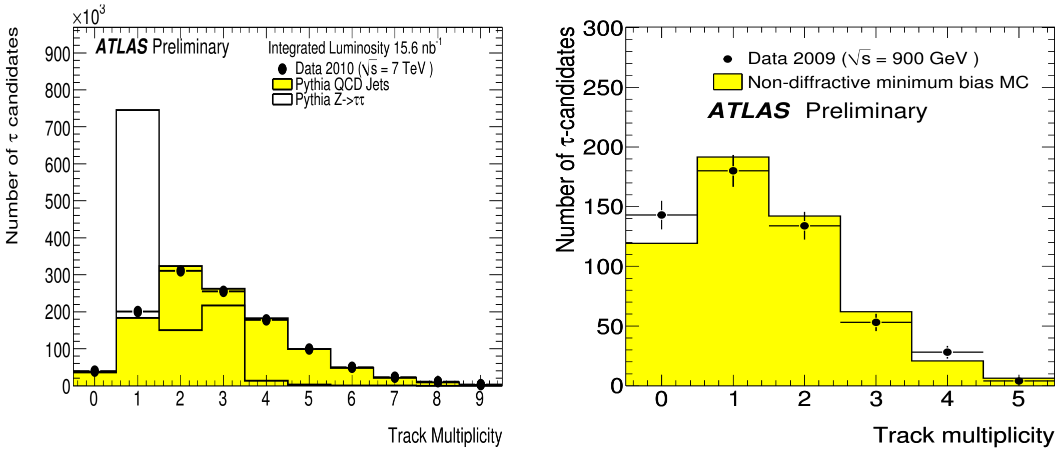

(a) (b)

Figure 5.17: Tracks multiplicity for τ_{had} candidates. Left shows the track multiplicity at 7 TeV with MC signal from MC overlaid. In the background sample more tracks associated to τ_{had} are found comparing the signal sample. Right plot shows the associated track multiplicity at 900 GeV, where 0-track bin discrepancy is found.

In these modes, very small number of cells in the strip layer pass the 200 MeV energy criteria.

- **Number of tracks associated to the τ_{had}: N_{trk}:** The typical number of tracks associated to τ_{had} (not QCD jets) is 1 or 3. It is an important parameter for τ_{had} identification. The tracks are counted around the seed within $\Delta R < 0.3$ (0.2) in the τ_{had} candidates without (with) seed track, where the tracks must pass the criteria listed in seciton 5.4.4. Please note, the track selection is different in Athena release 15 and 16.

  Figure 5.17 shows the number of associated tracks of τ_{had} candidates at $\sqrt{s} = 7\ TeV$ (left) and 900 GeV (right). MC agrees data within statistic uncertainty when center-of-mass energy is at 7 TeV. The discrepancy found in the 0-track bin for 900 GeV collision data is found.

  Due to track selection efficiency, τ candidates with 0, 2 or even more than 3 tracks are reconstructed as well.

If a τ candidate is calo-seeded, this means the candidate is a calo-only-seeded or double-seeded. More than 95% τ candidates are reconstructed with calo-seeded algorithm, where more than 50% are from calo-only-seeded ones, as studied in MC samples generated at $\sqrt{s} = 7\ TeV$ [69, 75].

5.4.2 Track-seeded reconstruction algorithm

This algorithm starts from a track with transverse momentum at least 6 GeV and passing the seed track criteria as illustrated in section 5.4.4. Tracks are found around the seed tracks with a tighter criteria, see section 5.4.4. The shape variables are calculated by combining calorimeter and tracker information or just based on tracks and clusters separately. Some variables that are important for identification are listed below:

- $\boldsymbol{R_{EM}}$:

  It is very similar as R_{EM} in calo-seeded candidates but only refers electromagnetic calorimeter cells around the seed track direction within cone size $\Delta R < 0.2$ (instead of 0.4 in calo-based algorithm). It is defined as equation:

  $$R_{EM} = \frac{\sum_{i=1}^{\Delta R_i < 0.2} E_{T,i}^{EM} \Delta R_i}{\sum_{i=1}^{\Delta R_i < 0.2} E_{T,i}}, \tag{5.7}$$

  where i runs over all the cells around the seed direction within distance $\Delta R < 0.2$ in the electromagnetic calorimeter except the back layer, $E_{T,i}$ is the uncalibrated energy projected to the transverse plane for cell i and ΔR_i is the distance of cell i to the seed direction.

  Figure 5.18 shows the R_{EM} distribution comparing data and MC samples for 7 TeV data. Since the cells for the reconstruction are collected around cone size 0.2, the width for track-based candidates is narrower than the calo-seeded ones. MC predicts data within the statistic uncertainty. The green points denote the τ_{had} candidates from MC $W \to \tau\nu$ sample.

- **The number of hits in strip layer in $\boldsymbol{\eta}$ direction $\boldsymbol{N_{strip}}$.**

  Same definition as in calo-seeded candidates but refers to the seed track direction.

- **The transverse energy weighted width in strip layer in $\boldsymbol{\eta}$ direction $\boldsymbol{\Delta\eta}$**

  Same definition as in calo-seeded candidates but cells are around seed within $\Delta R < 0.2$.

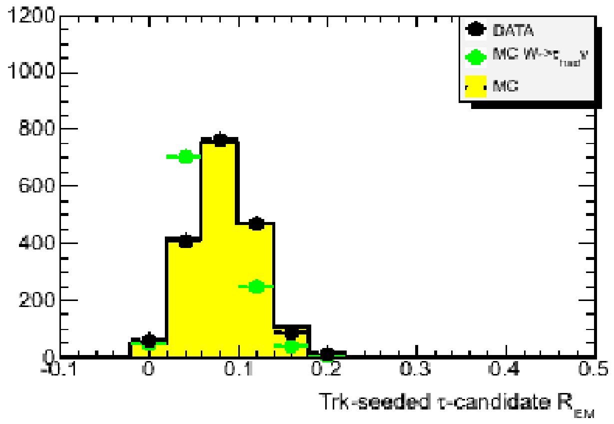

(a)

Figure 5.18: Transverse energy weighted radius for track-seeded candidates at 7 TeV.

- $\boldsymbol{f_{ring}}$:

  Isolation fraction is the same as in the calo-seeded algorithm but refers to the seed track instead of jet direction and the energy in the dominator is in the region $\Delta R < 0.2$. Energy is measured at EM scale.

- $\boldsymbol{f_{cent}}$:

  The same definition as in the calo-seeded algorithm except that the total transverse energy in the dominator are from cells around the seed track within $\Delta R < 0.2$.

- $\boldsymbol{R_{track}}$: Transverse momentum weighted width for the track system. It is the same as in the calo-seeded algorithm but refers to the seed track instead of jet direction.

- **The invariant mass of track system $\boldsymbol{m_{tracks}}$:** the same definition as in the calo-seeded algorithm but refers to the seed track instead of jet direction.

- **The number of tracks in the isolation cone:**

  The isolation cone region is defined as the ring with its center as the seed track and size $0.1 < \Delta R < 0.2$.

5.4.3 double-seeded τ_{had} candidates

Double-seeded candidates are expected to have better reconstruction performance comparing to the track-only-seeded and calo-only-seeded ones, because both good quality tracks and clusters appear. The shape variables are reconstructed separately for double-seeded candidates along the seeding jet or the seeding track for the calo-seeded or track-seeded algorithm. This means two sets of shape variables are reconstructed separately, but only the variables reconstructed referred to the seeding jet using calo-seeded algorithm are used for the identification.

5.4.4 Criteria of the tracks associated to τ_{had} candidates

This section summarizes the track criteria and how the selected tracks are saved for different reconstruction algorithms. The criteria used in Athena release 15 and 16 are different. To make things clear criteria of tracks for release 15 and 16 are described separately in sections.

5.4.4.1 Track criteria in Athena release 15

The tracks in the commissioning of the reconstruction algorithms shown in previous section is selected according to the criteria in Athena release 15 that is listed below:

- **The seed track.** It is the seed track in the track-seeded algorithm. Criteria: $p_T > 6\ GeV$, $|d_0| < 2mm$ and $nHitsSi \geq 7$, where nHitsSi is equal to number of Pixel Hits plus number of SCT Hits.

- **The default tracks.** They are the non-seeding tracks in the track-seeded algorithm, including the track-only-seeded and double-seeded candidates. Criteria:$p_T > 1\ GeV$, $|d_0| < 1mm$, $|z_0| \times \sin(\theta) < 1.5mm$, number of B-layer hits ≥ 1, number of Pixel hits ≥ 2 and $nHitsSi \geq 7$.

- **The loose tracks.** The are the tracks searched around the seeding jet axis in the calo-seeded candidates within distance $\Delta R < 0.3$, and around the seeding track axis in the trk-only seeded candidates within distance $\Delta R < 0.2$. Criteria $p_T > 1\ GeV$, $|d_0| < 2mm$, $|z_0| \times \sin(\theta) < 10mm$ and $nHitsSi \geq 7$.

To facilitate the identification, validation and analysis related to τ_{had}, tracks passing above criteria are divided into several categories according to their distance to the seed direction. For the calo-seeded, it is referring to the seeding jet direction, while in the track-only-seeded ones is referring to the seeding track direction. According to the distance to the seed, τ_{had} candidate is divided into "core" and "wide" regions. Calo-seeded and track-only-seeded candidates are slightly different on the divination.

- **Calo-only-seeded candidates:**

  Core region is within cone size $\Delta R < 0.3$ around the seeding jet direction. The tracks are required to pass the loose track criteria.

  Wide region, in principle it is defined as $0.3 < \Delta R < 0.4$, but no tracks in that region is saved into τ_{had} variables in release 15.

- **Track-only-seeded candidates:**

  Core region is within cone size $\Delta R < 0.2$ around the seeding track direction. The tracks are required to pass the default track criteria. Besides the default track, tracks that fail the default track criteria are saved also preparing for track validation.

  Wide region, same as calo-only-seeded, in principle it is defined as $0.2 < \Delta R < 0.4$, but no tracks in that region is saved into τ_{had} variables in release 15.

- **Double-seeded candidates:**

  Core region is defined as $\Delta R < 0.2$ for the default tracks around seeding track and $\Delta R < 0.3$ for the loose ones around seeding jet.

In release 15, the track selection is too complicated. To avoid the difficult situations, track criteria are changed in release 16.

5.4.4.2 Track criteria in Athena release 16

In release 16, tracks associated to the τ_{had} candidates do not include the loose ones. Also, for the track-only-seeded candidates that have no matched clusters in the calorimeter are not be considered in the identification methods (section 5.5). So the tracks refer to the calo-seeded candidates, except the leading track in the rack-only-seeded candidates. The criteria are listed:

- **The seed track.** It is the seed track in the double-seeded candidates. Criteria: $p_T > 6\ GeV$, $|d_0| < 1mm$, $|z_0| \times \sin(\theta) < 1.5mm$, number of B-layer hits ≥ 1, number of Pixel hits ≥ 2 and $nHitsSi \geq 7$, where nHitsSi is equal to number of Pixel Hits plus number of SCT Hits.

- **The default tracks.** The non-leading tracks pass default track criteria within $\Delta R < 0.2$ around the seeding-jet axis in calo-seeded candidates. Criteria: $p_T > 1\ GeV$, $|d_0| < 1mm$, $|z_0| \times \sin(\theta) < 1.5mm$, number of B-layer hits ≥ 1, number of Pixel hits ≥ 2 and $nHitsSi \geq 7$.

- **Other tracks.** Tracks fail the default track criteria are saved for possible validation study afterwards. Criteria: These tracks are referring all the tracks failing the default track selection around the seeding jet within $R < 0.4$.

- **The loose tracks.** This kind of tracks will be deprecated at last anyway, but just saved in release 16 for the transition from old track selection in release 15 to the new one afterwards. But they are not used in analysis. They are searched around the seeding-jet axis within distance $\Delta R < 0.3$. Criteria: $p_T > 1\ GeV$, $|d_0| < 2mm$, $|z_0| \times \sin(\theta) < 10mm$ and $nHitsSi \geq 7$.

The "core" region and "wide" region are defined in the calo-seeded candidates:

- **Core region** is within cone size $\Delta R < 0.2$ around the seeding jet direction. The tracks are required to pass the default track criteria.

- **Wide region** is defined as the ring $0.2 < \Delta R < 0.4$ around the seeding jet axis. Tracks passing default track criteria in this region are saved as wide-tracks.

5.5 Identification algorithms

Three identification methods for τ_{had} have been developed at ATLAS. They are cut-based, Boosted Decision Tree (BDT) and Likelihood (LLH) methods. BDT and LLH are Multi-variables methods (MV). At the first stage of data taking, due to lack of knowledge of the ATLAS detector, safe variables are used to identify τ_{had} from QCD jets in the methods. These variables are required to be powerful enough to reject backgrounds from QCD jets objects. At last, seven variables are chosen for this purpose.

Identification Level		$R_{EM} <$	R_{track}	$1/(E_T/p_T)$
Loose & $p_T^{\tau_{had}} < 80\ GeV$	$N_{trk} \leq 1$	$0.063 + \frac{0.663}{p_T}$ $-2.04 \cdot 10^{-4} p_T$	$0.134 + \frac{0.0328}{p_T}$ $-2.72 \cdot 10^{-4} p_T$	No cut
	$N_{trk} > 1$	$0.179 + \frac{0.0339}{p_T}$ $-5.17 \cdot 10^{-4} p_T$	$0.0565 + \frac{0.695}{p_T}$ $-1.44 \cdot 10^{-4} p_T$	4.55
Medium & & $p_T^{\tau_{had}} < 80\ GeV$	$N_{trk} \leq 1$	$0.0522 + \frac{0.715}{p_T}$ $-1.71 \cdot 10^{-4} p_T$	$0.134 + \frac{0.0328}{p_T}$ $-2.72 \cdot 10^{-4} p_T$	8.33
	$N_{trk} > 1$	$0.162 + \frac{0.447}{p_T}$ $-4.62 \cdot 10^{-4} p_T$	$0.0303 + \frac{0.810}{p_T}$ $-9.9 \cdot 10^{-5} p_T$	3.33
Tight & $p_T^{\tau_{had}} < 80\ GeV$	$N_{trk} \leq 1$	$0.0306 + \frac{0.819}{p_T}$ $-1.03 \cdot 10^{-4} p_T$	$0.134 + \frac{0.0328}{p_T}$ $-2.72 \cdot 10^{-4} p_T$	7.14
	$N_{trk} > 1$	$0.0833 + \frac{0.903}{p_T}$ $-2.15 \cdot 10^{-4} p_T$	$0.0146 + \frac{0.879}{p_T}$ $-7.21 \cdot 10^{-5} p_T$	2.5

Table 5.2: Cut value on identification variables validated in November 2010

They are $\boldsymbol{R_{EM}}$, $\boldsymbol{R_{track}}$, $\boldsymbol{E_T/p_T}$ **of the leading tracks**, **Cluster mass**, **Track mass**, **Central energy fraction** and **Electromagnetic fraction**. These variables are illustrated in section 5.4.

5.5.1 Cut-based method

By cutting on these variables with different thresholds, three criteria of τ identification ($\tau - ID$) levels are defined, denoted as loose, medium and tight with the signal selection efficiency lower successively. The cut values validated in November 2010 are illustrated in table 5.2.

Cut values shown in table 5.2 are only for τ_{had} with transverse momentum $15\ GeV < p_T < 80\ GeV$. τ_{had} in $W \to \tau\nu$ analysis has a upper-limit cut of 60 GeV on transverse momentum, as shown in chapter 6.

The performance of identification method can be reflected by two variables: signal efficiency and background efficiency. Signal efficiency is obtained from Monte Carlo before pure signal sample can be extracted from real collision data. It is the ratio of reconstructed τ_{had} candidates matched to generated hadronic decay τ leptons and passing the identification criteria ($N^{\tau_{had}}_{pass,match}$) to the total number of reconstructed τ_{had} candidates matched to generated hadronic decay τ leptons ($N^{\tau_{had}}_{pass,match}$). If the reconstructed τ_{had} and hadronical decaying τ lepton at generation level are overlapped within $\Delta R < 0.2$, they matched with each other. The τ_{had} candidate is required to have a transverse momentum threshold 15 GeV and reconstructed with correct number of associated tracks with respect to the matched true τ lepton. Larger value of signal efficiency refers to better algorithm performance. The signal efficiency is:

$$\epsilon_{sig} = \frac{N^{\tau_{had}}_{pass,match}}{N^{\tau_{had}}_{match}}, \tag{5.8}$$

The background efficiency can be obtained from data where the background samples are obtained by selecting QCD di-jets events. Contrary to signal efficiency, smaller value of background efficiency refers to better algorithm performance, that means less backgrounds are selected as signal. It is denoted as:

$$\epsilon_{bkg} = \frac{N^{bkgd}_{pass}}{N^{bkgd}_{total}}, \tag{5.9}$$

where N^{bkgd}_{pass} is the number of reconstructed τ_{had} candidates passing the identification criteria in the background sample, N^{bkgd}_{total} is the total number of reconstructed τ_{had} candidates.

The signal efficiencies of cut-based algorithm are 30%, 50% and 60% for tight, medium and loose respectively [70]. These results were obtained with athena release 15, means the old set of tracks criteria. Figure 5.19 shows the background efficiency and signal efficiency. Please note that for the cut-based algorithm, the cut values on identification variables are different in the table 5.2, where in the table the cut was optimized in November 2010 while this background and signal efficiency is studied in August 2010. For the $W \to \tau\nu$ analysis (will be illustrated in chapter 6) the identification with cut optimized in November 2010 will be used.

5.5.2 Multi-variables identification methods

All the seven safe variables are used in the BDT identification method, while six of them (except f_{cent} due to its correlation with other variables) are used in the LLH method.

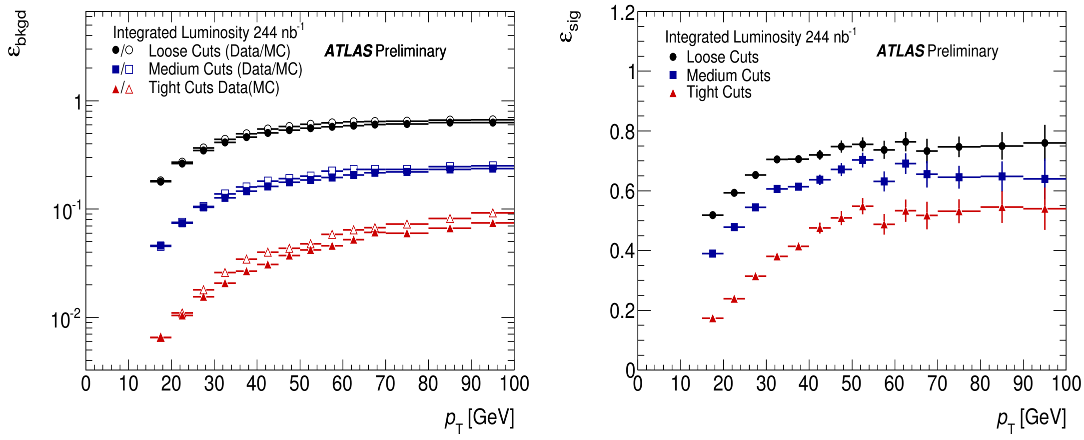

(a) a (b) b

Figure 5.19: Background efficiency obtained from data using integrated luminosity $\sim$ 244 nb^{-1} (left) and signal efficiency obtained from MC $Z \to \tau\tau$ sample (right).

5.6 Summary

The two reconstruction algorithms (calo-seeded and track-seeded) of τ_{had} developed and implemented at ATLAS have been illustrated in this chapter. With collision data collected at the starting of LHC at $\sqrt{s} = 900\ GeV$ and 7 TeV, both the two algorithms have been commisioned. The commissioning is important for the implementation of identification of τ_{had} and essential to the analysis related to τ lepton. In the commissioning using 7 TeV data, with the selected QCD jet events in the data and MC, MC signal of τ_{had} from $Z \to \tau\tau$ sample is overlaid. This has shown that the defined variables are powerful for the discrimination of τ_{had} from QCD jets as expected (like R_{EM}, f_{ring} and R_{track} etc.). Variables show good performance in data and MC comparison for the background events. This gives us the confidence to use them in the identification algorithms and then applied to the physics analysis related tau τ lepton(s).

Three identification methods (cut-based, BDT and LL) of τ_{had} have been developed and implemented at ATLAS. These algorithms have been studied and compared using the first data with about 244 nb^{-1} data collected at $\sqrt{s} = 7\ TeV$. The signal efficiencies of cut-based algorithm are 30%, 50% and 60% for tight, medium and loose respectively. Multi-variables algorithms (BDT and LLH) show better signal efficiency and higher background selection.

τ_{had} with the commissioned good and safe variables for identification will be applied to the analysis, like $W \to \tau\nu$ and $Higgs \to \tau\tau$.

6

Towards measurement of $W \to \tau\nu$ cross section at $\sqrt{s} = 7$ TeV

6.1 Introduction

This chapter is to select the $W \to \tau\nu$ events with the τ decaying hadronically ($W \to \tau_{had}\nu$ [1]). A very preliminary cross section measured at center-of-mass energy $\sqrt{s} = 7$ TeV is obtained as well.

When W boson decays leptonically, a neutrino is produced along with the lepton. Neutrinos are neutral and have negligible couplings to materials in detector. The escape the detector and hence measuring a missing momentum. At p-p collider, it is impossible to measure the momentum of the colliding quarks or (or gluons) event by event along the beam direction. But in the plane perpendicular to the beam line, quarks (or gluons) almost do not have momentum. According to the low of conservation of momentum, the vector sum of the momentum from neutrinos and the one from the visible particles are opposite to each other in the direction but the absolute value is the same. We call the measured missing momentum in the plane perpendicular to the beam direction as missing transverse momentum (E_T^{miss}) [72, 73, 74].

Theoretically, for the mode of W boson decaying into τ and ν_τ, τ and ν_τ take the

[1] In this chapter, $W \to \tau_{had}\nu$ denotes the $W \to \tau\nu$ process with τ decaying hadronically. Please note here the τ_{had} here in $W \to \tau_{had}\nu$ is different in chapter 5. In chapter 5, τ_{had} denotes the visible part of the hadronic decay τ lepton. In this chapter, when τ_{had} appears in $W \to \tau_{had}\nu$, it means the τ lepton decays hadronically, while the τ_{had} appears outside of $W \to \tau_{had}\nu$, it means the visible part of the hadronic decay τ lepton

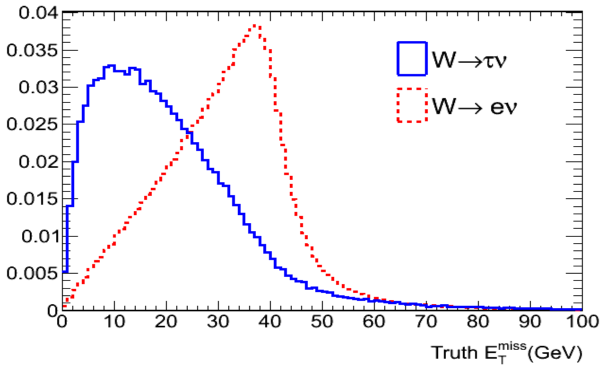

(a)

Figure 6.1: The solid blue line shows the E_T^{miss} distribution from $W \rightarrow \tau_{had}\nu$ at the generation level. It shifts to left comparing to the dashed red line, E_T^{miss} from $W \rightarrow e\nu$ at the generation level.

same momentum of their absolute values but the directions are opposite to each other in the transverse plane at ATLAS assuming the idea collision conditions. Considered the fluctuations of the measurements from detector, the directions of the two leptons are not exactly back-to-back in the transverse plane. But the angle between them is large (near to π).

τ's lifetime is short, that it cannot fly far enough for the detectors to detect it directly. However, τ lepton is boosted with a large Lorentz factor in most of the cases in the $W \rightarrow \tau\nu$ events, the secondary vertex can be reconstructed in the multi-prongs decay modes thanks to the precise measurement of the inner detector. Due to the large boosting, the decaying products from τ lepton are nearly collimated. Therefore, neutrino(s) from τ lepton decay balances, to some extent, the missing transverse momentum from neutrino produced along with τ. However, there is still large missing transverse momentum for these kinds of events. Figure 6.1 shows the missing transverse momentum at the generation level (from MC samples) for the $W \rightarrow \tau_{had}\nu$ overlaid with $W \rightarrow e\nu$ events. E_T^{miss} from $W \rightarrow \tau_{had}\nu$ shifts to a smaller value comparing to $W \rightarrow e\nu$ events due to the balance from the neutrino(s) produced by τ lepton decay.

Figure 6.2 shows, at the generation level, the p_T of the τ_{had} from $W \rightarrow \tau_{had}\nu$ overlaid with the τ lepton p_T (filled region); For comparison, the p_T of electron from $W \rightarrow e\nu$ events at the generation level is shown in the plot (dashed line). Same as the E_T^{miss}, p_T of the τ_{had} from $W \rightarrow \tau_{had}\nu$ shifts to left.

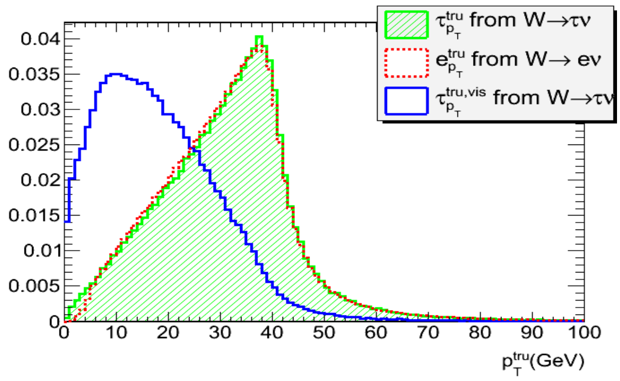

(a)

Figure 6.2: The solid line shows the p_T of the visible part of the hadronically decaying τ from $W \to \tau\nu$ at the generation level. It shifts to left comparing to the τ lepton (filled region) and p_T of electron from $W \to e\nu$ (dashed line) at the generation level.

In next sections, data samples, MC samples, trigger, cut flow and background estimation will be illustrated. Using track-based missing transverse momentum (p_T^{miss}), 50% backgrounds are reduced while saving 92% signal events as studied in data and MC samples. By applying another new method (new defined E_T^{miss} significance: $S^{new}_{E_T^{miss}}$) we manage to reduce the large pile up effects of the method used in previous $W \to \tau\nu$ analysis [71]. Track-based missing transverse momentum [76] combined with $S^{new}_{E_T^{miss}}$ will be used in the signal selection and cross section measurement.

6.2 Data samples

We use data at center-of-mass energy $\sqrt{s} = 7\ TeV$ collected from March 31 of 2010 to the end of the year. Under our trigger strategy (section 6.3), the integrated luminosity is 36.8 pb^{-1}.

Due to increasing of the luminosity from LHC during the year 2010, different trigger settings are used. Data is divided into different periods according to the data taking configuration, where within a single period, runs have the same conditions.

Seven data periods were collected in 2010. Some data periods are separated into several sub-periods, as shown in table 6.1. The structure and corresponding luminosity under the trigger we are using for the analysis will be illustrated in section 6.3.1.

Data periods	A	B	C	D	E	F	G	H	I
Number of sub-periods	1	2	2	6	7	2	6	2	2

Table 6.1: Number of sub-periods for each data period collected in 2010.

6.2.1 Data stream and format

Events passing a trigger chain (section 3.4.1) are written into a data stream corresponding to the trigger. At present, four different data streams for physics analysis have been established at ATLAS:

- **JetTauETmiss:** Consists of events passing jet, τ or E_T^{miss} trigger chain.
- **Egamma:** Consists of events passing electron or photon trigger chain.
- **MinBias:** Consists of events passing minimum bias trigger chain.
- **Muons:** Consists of events passing muon trigger chain.

For this analysis, JetTauETmiss data stream is used. D3PD (section 3.4.2) produced centrally by τ performance group with a tag 07-00-01-01 is utilized.

6.2.2 Data Quality and Good Runs List

Data Quality (DQ) is monitored both online and offline. The purpose of data quality monitoring is to select good runs having real collisions, all the related sub-detectors being well operated and the events processing systems working smoothly, etc.

Good Runs List (GRL) is a number of runs passing data quality criteria. It is obtained based on the DQ information taking the luminosity block as the unit to select the events good for the dedicated analysis.

For $W \to \tau\nu$ process, good E_T^{miss} and τ candidates are needed. This requires that all the sub-detectors are operational according to the expected status and the software of τ_{had} and E_T^{miss} are running smoothly. This requires that both the inner detector and calorimeters running in optional conditions.

6.2.3 Monte Carlo simulation samples

MC samples for signal and background events are listed in table 6.2. Signal sample ($W \to \tau_{had}\nu$) is obtained from inclusive $W \to \tau\nu$ sample by requiring the existing of at least one hadronically decaying τ at true level, while the $W \to \tau_{lep}\nu$ sample (treated as background) is composed of the rest events.

The processes are generated with cross section to the next-to-next-to-leading order (NNLO) [81, 82]. The cross section values of inclusive $W \to \tau\nu$, $W \to e\nu$ and $W \to \mu\nu$ are 10.46 nb, while $Z \to ee, \mu\mu$ and $\tau\tau$ are 0.99 nb. Pythia 6.4 [79] is used to generate the processes. The generated particles are then simulated with Geant4 [80]. The backgrounds from these processes are called EW backgrounds.

The samples that are simulated with **in-time** pile up setup (section 6.2.3.1) are used in this analysis.

6.2.3.1 Vertices re-weighting

Two kinds of pile up models have been developed for the MC samples. One is in-time pile up, the other one is bunch-train pile up.

Name	MC ID	Cross section (nb)	Production tag	Pile up
Signal and electromagnetic background samples				
$W \to \tau\nu$ Pythia (incl)	107054	10.46	e574_s934_s946_r1833_r1700	Bunch-train
			e574_s934_s946_r1660_r1700	In-time
$W \to e\nu$ Pythia (no filter)	106043	10.46	e574_s933_s946_r1831_r1700	Bunch-train
			e574_s933_s946_r1661_r1700	In-time
$W \to \mu\nu$ Pythia (no filter)	106044	10.46	e574_s933_s946_r1831_r1700	Bunch-train
			e574_s933_s946_r1659_r1700	In-time
$Z \to ee$ Pythia (no filter)	106046	0.99	e574_s933_s946_r1831_r1700	Bunch-train
			e574_s933_s946_r1661_r1700	In-time
$Z \to \mu\mu$ Pythia (no filter)	106047	0.99	e574_s933_s946_r1831_r1700	Bunch-train
			e574_s933_s946_r1659_r1700	In-time
$Z \to \tau\tau$ Pythia	106052	0.99	e574_s934_s946_r1833_r1700	Bunch-train
			e574_s934_s946_r1660_r1700	In-time

Table 6.2: Monte Carlo samples.

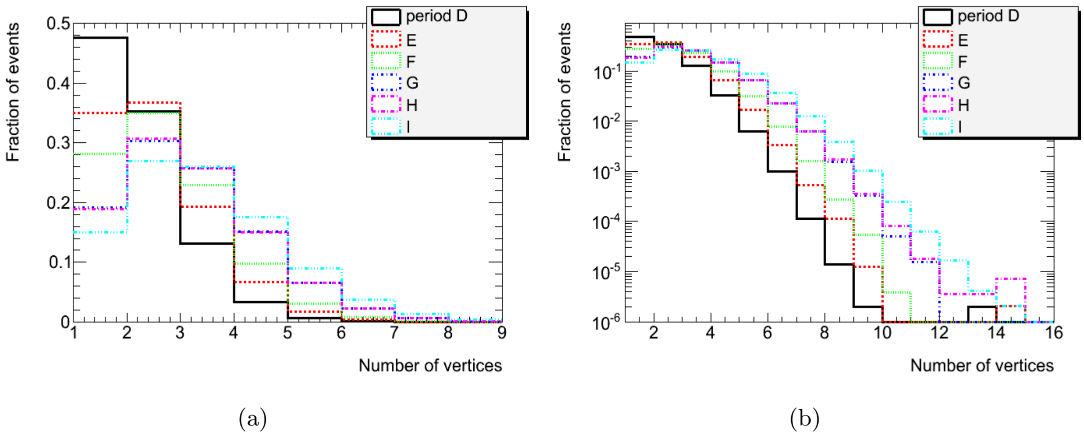

Figure 6.3: Number of vertices distribution for collision data in different data periods (from period D to period I), right plot shows the same distribution but with log scale of the y-axis. The distribution is obtained after the number of vertices requirement in the event selection flow (section 6.6.1).

- **in-time pile up:** In the early stage of data taking, bunches were far from each other. The pile up came from the collisions within the triggered bunch, it is called in-time pile up. To simulate the in-time pile up the hard collided events are overlaid with minimum-bias MC events, where the overlaid interactions is a Poissonian distribution with mean value $< n >= 2$ [83].

- **bunch-train pile up:** From period G until to end of the data taking in 2010, the number of bunches were increased in a "train". So that the space between bunches were shorten to ~ 75 ns while space between trains were long enough. Pile up was not only from the same triggered bunch, but also from near by bunches. We call the kind pile up from near by bunches as out-time pile up. In the simulation technique language, the simulation trying to translate the pile up due to short spaces between bunches (and also the pile up due to multi-collision from the single bunch) are called as bunch-train pile up.

The number of vertices distribution for data in different periods are different as shown in figure 6.3. In the later periods, e.g. period G, H and I, the pile up is not negligible any more. The distribution is obtained after the number of vertices requirement in the event selection flow (section 6.6.1).

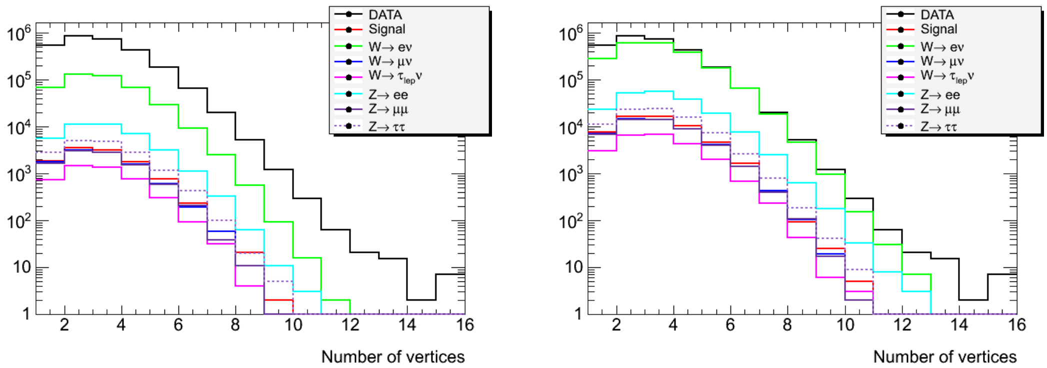

(a) (b)

Figure 6.4: Number of vertices distribution comparing data and MC for in-time pile up setup (left) and for bunch-train pile up setup (right). The data is from run 166786 (middle of period H1) to 167844 (the last run of period I) that is applied trigger tau16_medium_xe22_noMu (section 6.3), while the MC is applied the same trigger. The distribution is obtained after the number of vertices requirement in the event selection flow (section 6.6.1).

As the number of vertices in MC is not the same as in data, re-weighting of vertices distribution for MC according to the number of vertices distribution in data is necessary.

Figure 6.4 shows the number of vertices from in-time pile up MC samples comparing to data (left), and the number of vertices from bunch-train pile up MC samples comparing to data (right). The distributions are after the number of vertices requirement in the event selection flow (section 6.6.1). The bunch-train pile up model predicts the number of vertices distribution a little bit larger comparing to data.

Figure 6.5 shows the weight for in-time (left) and bunch-train pile up MC samples (right). To be consistent, the distributions are after the jet cleaning requirement in the event selection flow (section 6.6.1), since the analysis is done by re-weighting number of vertices in MC samples after the jet cleaning cut. However, the weights after the number of vertices requirement and after the jet cleaning has no difference, as shown in figure 6.6 of the number of vertices distribution for data (left) and MC signal sample (right) at different event selection levels.

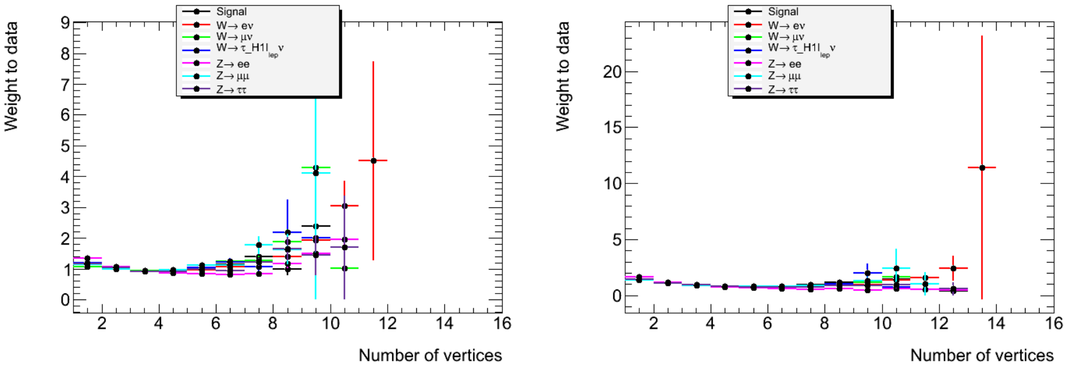

(a) (b)

Figure 6.5: Weight for in-time pile up (left) and bunch-train pile up MC samples obtained in release 16 (right). To be consistent, the distribution obtained is after the jet cleaning requirement in the event selection flow (section 6.6.1), since the analysis is done by re-weighting number of vertices in MC samples after the jet cleaning cut. The weight is for the MC samples applied with trigger tau16_medium_xe22_noMu.

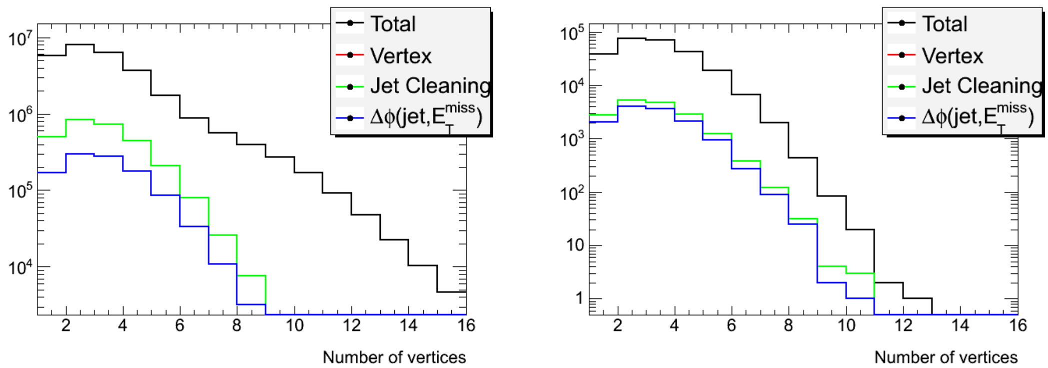

(a) (b)

Figure 6.6: Number of vertices distribution after different cuts (number of vertices requirement, jet cleaning and $|\Delta\phi(E_Y^{miss}, jet)| > 0.5$) for data is from run 166786 (middle of period H1) to 167844 (the last run of period I) that is applied trigger tau16_medium_xe22_noMu (left) and for the MC signal with in-time pile up set up that is applied the same trigger (right).

6.2.3.2 Vertices re-weighting strategy

The strategy for the vertices re-weighting is to re-weight period by period if the triggers among periods are different. Otherwise if the triggers are the same through several periods, the re-weighting is based on all the data through these periods. In section 6.3, trigger strategy will be illustrated, where all the periods collected in 2010 are separated into two parts with each part contains several periods. The re-weighting will be obtained separately for the two parts. Because different triggers provide different acceptances, we cannot combine the weight directly from different triggers.

6.3 Trigger

Two triggers, based on E_T^{miss} and τ_{had} candidate signatures, are used for the $W \to \tau\nu$ analysis (aiming to the cross section measurement) in the data samples collected in 2010. They are:

- **tau12_loose_xe20_noMu:** This trigger starts from narrow clusters with p_T threshold of 5 GeV and at least 10 GeV missing transverse momentum without muon correction (xeXX_noMu) at L1 [85]. The objects firing the L1 trigger are then passed to HLT triggers L2 and EF for further selection. At L2, the clusters passing the L1 trigger are required to have a p_T threshold of 7.55 GeV and passing the loose τ_{had} criteria at trigger level; The missing transverse momentum without muon correction is required to be larger than 12 GeV of its p_T. At EF, The objets from L2 are re-calculated again; The clusters p_T threshold is increased to 12 GeV; Loose criteria at EF level is applied again. Missing transverse momentum without muon correction at EF level is required to be at least 20 GeV for its p_T.

- **tau16_medium_xe22_noMu:** This trigger is very similar with **tau12_loose_xe20_noMu** but with different thresholds for the objects (clusters and missing transverse momentum without muon correction) and medium τ_{had} criteria instead of loose. The thresholds of the clusters at L1, L2 and EF are 6 GeV, 9 GeV and 16 GeV. The thresholds of the missing transverse momentum without muon correction are L1, L2 and EF are 10 GeV, 15 GeV and 22 GeV.

To be more clear, table 6.3 shows the criteria for trigger tau12_loose_xe20_noMu and tau16_medium_xe22_noMu. In the table, p_T^{isol}/p_T^{core} is the scalar sum of the tracks with $p_T > 1.5\ GeV$ in the isolation/core region ($0.1 < \Delta R < 0.3/\Delta R < 0.1$) around the reprocessed cluster at L2; loose track is the track with $p_T > 1\ GeV$.

6.3.1 Trigger strategy for the analysis

Actually, at the beginning of data taking, HLT was off until the first several runs in period D1 (run 158269). Trigger bit of tau12_loose_xe20_noMu was off until period D2(run 158582) [87]. The total integrated luminosity until tau12_loose_xe20_noMu turned on is about 100 nb^{-1}, which will not be considered in this analysis. From run 166786 (middle of H1 after run 166658) trigger tau12_loose_xe20_noMu is pre-scaled. Therefore, tau16_medium_xe22_noMu is used. The data samples are separated into two parts according to the trigger. We call the two parts as data periods D3H1 and H1I for simple denotation.

Table 6.4 shows the summary of the trigger strategy. Based on the trigger strategy, the vertex re-weighting values for in-time pile up MC samples are shown in table 6.5. The re-weighting is applied to one vertex, two vertices, three vertices, four vertices and more than or equal to five vertices events, where the events with more than four vertices are re-weighted together. In period H1I, events passing the trigger tau12_loose_xe20_noMu are used in the background control regions as will be illustrated in section 6.8.

6.3.2 Trigger turn-on curve

Figure 6.7 shows the efficiencies of E_T^{miss} (left) and τp_T (p_T^{τ}) (right) in the trigger bit tau16_medium_xe22_noMu. They are obtained from signal MC sample. The requirements on E_T^{miss} at least 30 GeV and p_T^{τ} between 20 and 60 GeV as shown in the figure will be illustrated in section 6.6. The p_T^{τ} goes through almost all the turn-on curve (right), which means the systematic from trigger would be large. On the other hand, requirement of E_T^{miss} at 30 GeV is at the middle of the turn-on curve (left).

		tau12_loose_xe20_noMu	**tau16_medium_xe22_noMu**
Levels	**objects**	**thresholds**	**thresholds**
L1	**cluster**	$> 5\ GeV$	$> 6\ GeV$
	xe_noMu	$> 10\ GeV$	$> 10\ GeV$
L2	**cluster**	$> 7.55\ GeV$ $R_{EM} \leq 0.0178$ $p_T^{isol}/p_T^{core} \leq 0.1$ $1 \leq N_{trk}^{core} \leq 10$	$> 9\ GeV$ $R_{EM} \leq 0.0124$ $p_T^{isol}/p_T^{core} \leq 0.1$ $1 \leq N_{trk}^{core} \leq 10$
	xe_noMu	$> 12\ GeV$	$> 15\ GeV$
EF	**cluster**	$> 12\ GeV$ $N_{trk}^{loose} = 1\ \&\ R_{EM} \leq 0.105$ $N_{trk}^{loose} > 1\ \&\ R_{EM} \leq 0.125$ $N_{trk}^{loose} = 1\ \&\ p_{T,leading}^{loose} \geq 2.5\ GeV$ $N_{trk}^{loose} > 1\ \&\ p_{T,leading}^{loose} \geq 2.5\ GeV$ $1 \leq N_{trk}^{core} \leq 10$	$> 16\ GeV$ $N_{trk}^{loose} = 1\ \&\ R_{EM} \leq 0.08$ $N_{trk}^{loose} = 1\ \&\ R_{EM} \leq 0.092$ $N_{trk}^{loose} = 1\ \&\ R_{dist}^{trk} \leq 0.076$ $N_{trk}^{loose} = 1\ \&\ R_{dist}^{trk} \leq 0.062$ $1 \leq N_{trk}^{loose} \leq 6$
	xe_noMu	$> 20\ GeV$	$> 22\ GeV$

Table 6.3: Trigger configuration for tau12_loose_xe20_noMu and tau16_medium_xe22_noMu.

Data periods	Runs range	trigger	Luminosity (pb^{-1})
D3H1	158632-166658	tau12_loose_xe20_noMu	12.27 pb^{-1}
H1I	166786-167844	tau16_medium_xe22_noMu	24.53 $pb{-}1$
		tau12_loose_xe20_noMu	5.80 pb^{-1} (pre-scaled)

Table 6.4: Trigger and corresponding luminosity for the analysis.

Vertices	Signal	$W \to e\nu$	$W \to \mu\nu$	$W \to \tau_{lep}\nu$	$Z \to ee$	$Z \to \mu\mu$	$Z \to \tau\tau$
Re-weighted to data from run 158632 to 166658							
=1	1.74	1.72	1.73	1.75	1.98	1.71	1.78
=2	1.11	1.12	1.09	1.13	1.21	1.13	1.15
=3	0.84	0.84	0.83	0.84	0.83	0.83	0.83
=4	0.68	0.69	0.68	0.67	0.63	0.70	0.67
≥ 5	0.57	0.57	0.58	0.56	0.46	0.57	0.54
Re-weighted to data from run 166786 to 167844							
=1	1.12	1.14	1.07	1.14	1.32	1.12	1.14
=2	0.97	0.99	0.95	1.00	1.07	0.98	1.02
=3	0.94	0.94	0.95	0.93	0.92	0.91	0.93
=4	0.97	0.95	0.98	0.93	0.87	0.98	0.94
≥ 5	1.11	1.07	1.20	1.07	0.87	1.16	1.03

Table 6.5: Vertex re-weighting values for in-time pile up MC samples. The re-weighting is applied to one vertice, two vertices, three vertices, four vertices and more than or equal to five vertices events, where the events with more than 4 vertices are re-weighted together.

6.4 Objects reconstruction

Several objets are needed in this analysis, including jet, E_T^{miss}, τ_{had}, electron, μ and tracks.

- **Jets** used in this analysis are reconstructed with anti-kt algorithm starting from topological clusters. Jet size of 0.4 is used.
- $\boldsymbol{E_T^{miss}}$ involved in this analysis is reconstructed using the full events and calibrated based on the physics objects. The tracks reconstructed but not reach the calorimeter (therefore no matched topo-clusters) are added back to the E_T^{miss} calculation. And if the track matched to the topo-cluster, the track momentum is used to the E_T^{miss} reconstruction [84]. $E_{T,x}^{miss}$ and $E_{T,y}^{miss}$ are reconstructed firstly

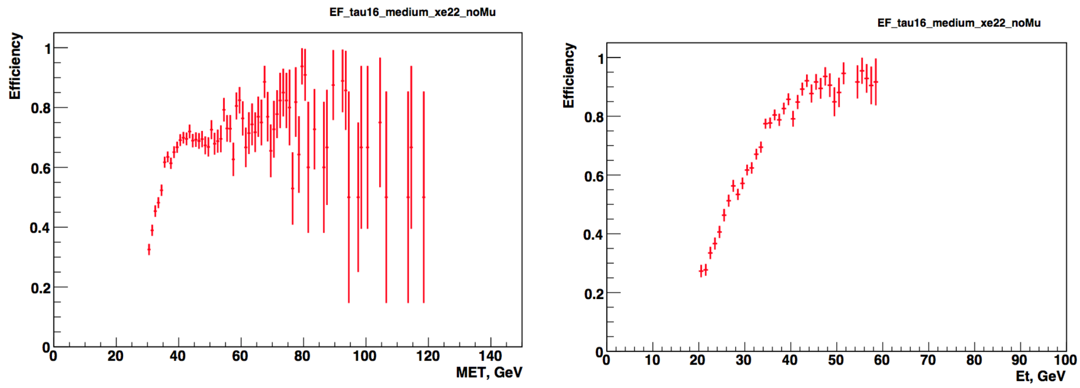

(a) (b)

Figure 6.7: Efficiencies of E_T^{miss} (left) and p_T^{τ} (right) in the trigger bit tau16_medium_xe22_noMu obtained in the signal MC sample.

by projecting the cells to x and y axis of the ATLAS coordinator. E_T^{miss} are calculated according to $\sqrt{(E_{T,x}^{miss})^2 + (E_{T,y}^{miss})^2}$ and calibrated with objects based calibration scheme (RefFinal). ΣE_T is the scalar sum of the transverse energies of the objets used to reconstruct E_T^{miss}.

- τ_{had} used in the analysis are reconstructed using calo-seeded algorithm (section 5.4.1).

- **Electron and muon** veto is to reduce backgrounds from processes producing electron or/and muon. Two schemes are involved:

  Electron and muon veto within τ_{had} reconstruction and identification algorithm: Electron veto has been illustrated in section 5.3.4, that it is implemented based on several variables to separate electron and τ_{had}. Based on this, medium and tight schemes have been developed. The medium veto gives a rejection factor of 50 by loosing $\sim 5\%$ of signal while the tight veto gives a rejection factor of 1000 while only $\sim 15\%$ of signal reduction. **Muon veto** is mainly based on the feature that muon deposits little energy in calorimeters (including electromagnetic and hadronic). Based on this, events with total deposited energy in calorimeters ≤ 5 GeV are rejected.

  Event based electron and muon veto: Here the electron and muon reconstruction are from the egamma and muon performance group.

- **Tracks** here are referring all the inner-detector tracks. In the analysis, track parameters used to select good quality tracks are required to be with respect to primary vertex.

6.5 Backgrounds processes

The main backgrounds considered in the $W \to \tau_{had}\nu$ analysis are listed:

- **QCD multi-jets:**

  When one of the jets in the event is mis-identified as τ_{had} and the E_T^{miss} is mis-measured due to its resolution and jets mis-measurement, QCD multi-jets becomes background events. It is the dominant background for $W \to \tau_{had}\nu$ because of large cross section (at an order of barn).

- **$W \to \tau_{lep}\nu$, $W \to e\nu$ and $W \to \mu\nu$:**

  When the electron or muon is mis-identified as τ_{had}, they become $W \to \tau\nu$ backgrounds. However, thanks to the powerful electron and muon veto both in and out of τ_{had} reconstruction algorithm, the backgrounds from $W \to e\nu$ and $W \to \mu\nu$ are not important. $W \to \tau_{lep}\nu$ is treated as background because it has very similar behavior as $W \to e\nu$ or $W \to \mu\nu$.

- **$Z \to ee$ and $Z \to \mu\mu$:**

  When one of the electrons/muons is mis-identified as τ_{had} and another one is missed, $Z \to ee$ and $Z \to \mu\mu$ become backgrounds. Cross section of $Z \to ee(\mu\mu)$ at the LHC is about 10 times smaller than $W \to \tau\nu$, and the electron and muon identification efficiency are high, the backgrounds from$Z \to ee$ and $Z \to \mu\mu$ are negligible.

- **$Z \to \tau\tau$:**

  When one of the τs decays hadronically, $Z \to \tau\tau$ becomes irreducible background. However, $Z \to \tau\tau$ cross section is 10 lifetimes less then $W \to \tau\nu$, background from $Z \to \tau\tau$ is small.

6.6 Event selection

6.6.1 The preselection

We need to clean events that are not cleaned up by DQ and trigger. After applying the GRL and trigger requirements, several cleaning cuts are implemented additionally.

First, make sure that the events are from collision by requiring at least one vertex with number of associated tracks ≥ 3. The associated tracks are the ones used to reconstruct and fit the vertex.

Second, clean up the events with badly reconstructed jets [77]. This is to avoid the τ_{had} coming from a bad reconstructed jet which may come from noise in the calorimeter or out-of-time cosmic rays. The jets are required to have $p_T > 20$ GeV when the cleaning criteria is checked.

Third, veto the events with at least one jet in the crack region ($1.3 < |\eta| < 1.7$) with $p_T > 20\ GeV$. This is to avoid mis-measured E_T^{miss} due to mis-measured jet p_T.

Fourth, veto the events with at least one reconstructed jet with $p_T > 20GeV$ near to E_T^{miss} in the ϕ direction (transverse plane), i.e. $|\Delta\phi| < 0.5$. This also is to avoid mis-measured E_T^{miss} due to mis-measured jet p_T.

6.6.2 The signal event selection

After preselection, further selections are implemented to select signal events according to the signal signature ($\tau_{had} + E_T^{miss}$). First we require the event has a large missing transverse momentum by cut on $E_T^{miss} > 30$ GeV. Events are then required to have at least one calo-based τ_{had} candidate passing the tight tau identification criteria. Here the tight tau identification is referring the cut-based algorithm. The leading one (with highest p_T) is treated as the τ_{had} from $W \to \tau_{had}\nu$ events, called leading-tight τ_{had} candidate. Then the leading-tight τ_{had} candidate is require to take p_T between 20 GeV and 60 GeV and not sit in the crack region ($1.3 < |\eta| < 1.7$). The purpose of cutting on p_T of the leading-tight τ_{had} candidate is to reduce the background from QCD multi-jets where the jets with large p_T pass the selection.

To reduce backgrounds form electroweak processes, $W \to e\nu, \mu\nu, \tau_{lep}\nu$, $Z \to ee$ and $Z \to \mu\mu$, electron and muon veto are applied. Here the electron and muon veto is implemented with the one developed by tau performance group (section 6.4). After that, event based lepton veto is applied for further cleaning of backgrounds from such processes: events are rejected if at least one loose electron or one combined muon with $p_T >$ 5 GeV is found.

After all the above cuts, QCD multi-jets background is still dominant. Two methods of $\Delta\phi(E_T^{miss}, p_T^{miss})$ combining with new defined E_T^{miss} significance are used to reduce the QCD background. These two methods are new comparing to previous study, like in the $W \rightarrow \tau_{had}\nu$ observation analysis [71]. New defined E_T^{miss} significance use the $\sum p_T$ in the dominator instead of $\sum E_T$. $\sum p_T$ is the scalar sum of the p_T of the tracks passing passing good quality criteria (section 6.7.2.1) associated to the primary vertex (by requiring the track impact parameters small). Therefore, the pile up dependence is reduced significantly. Its definition is:

$$S_{E_T^{miss}}^{new} = \frac{E_T^{miss}[GeV]}{0.5[GeV^{1/2}] \cdot \sqrt{\Sigma p_T[GeV]}}, \tag{6.1}$$

while the old one is defined as [71]:

$$S_{E_T^{miss}}^{old} = \frac{E_T^{miss}[GeV]}{0.5[GeV^{1/2}] \cdot \sqrt{\Sigma E_T[GeV]}}, \tag{6.2}$$

6.7 Track-based missing transverse momentum and new E_T^{miss} significance

6.7.1 Track-based missing transverse momentum

The motivation to define the p_T^{miss} [76] is to distinguish processes with real missing energy from backgrounds producing fake missing energy by utilizing the correlation between it and the E_T^{miss}. It takes an important role in suppressing QCD multi-jets background for $W \rightarrow \tau_{had}\nu$ signal selection.In QCD events, E_T^{miss} comes mainly from mis-measurement of jets p_T. The mis-measurement is random, so the direction of E_T^{miss}, e.g $\phi(E_T^{miss})$ is random. The case is similar to p_T^{miss} in the QCD multi-jets events. However, the case is different in $W \rightarrow \tau_{had}\nu$, where E_T^{miss} is due to neutrinos in the final states. Calorimeters measure the E_T^{miss} and provide the direction of real E_T^{miss}, which is not random. Similar to calorimeters, trackers detect the charged particles. The opposite vector sum of the charged particles gives p_T^{miss}. The direction of p_T^{miss} reflects the direction of the vector sum of the neutrinos p_T, e.g. E_T^{miss} direction. Therefore, in the events with real missing energy, p_T^{miss} and E_T^{miss} point to the same direction in the transverse plane.

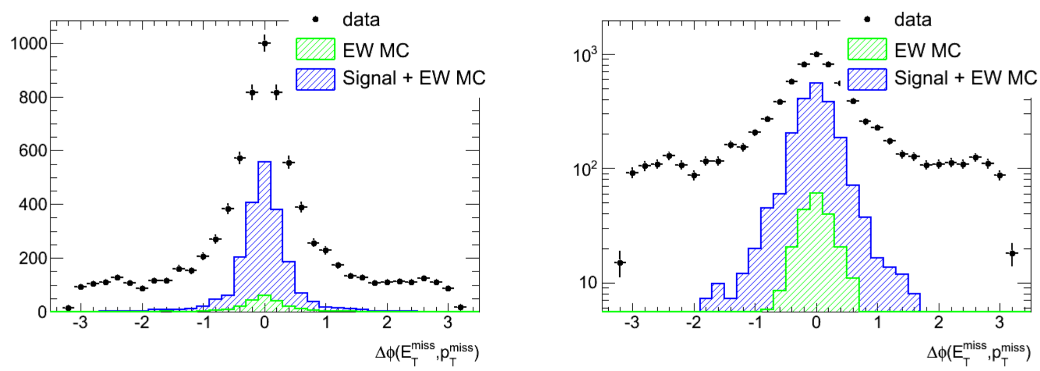

(a) (b)

Figure 6.8: Data and MC comparison for the difference between E_T^{miss} and p_T^{miss} in the azimuthal direction ($\Delta\phi(E_T^{miss}, p_T^{miss})$). a) is at the normal scale with Monte Carlo samples normalized to data luminosity and b) are the same but with log scale in the y-axis. The data is from data period H1-I2 and the plots are obtained after lepton veto.

Figure 6.8 shows the data and MC comparison for the difference between E_T^{miss} and p_T^{miss} in the azimuthal direction ($\Delta\phi(E_T^{miss}, p_T^{miss})$). The QCD multi-jets MC is not shown due to its less statistics that makes sharp peaks in the plots. However, according to the MC samples prediction, signal from $W \rightarrow \tau_{had}\nu$ shows the peak around zero where data have much more events in the regions with large —$\Delta\phi(E_T^{miss}, p_T^{miss})|$, where the events are taking fake E_T^{miss}. The tracks in p_T^{miss} are required to pass several track quality cuts: $p_T > 500\ MeV$, $|d_0| < 1.5\ mm$, $|z_0| \cdot \sin(\theta) < 1.5\ mm$, Number of Pixel hits ≥ 1 and Number of SCT hits ≥ 7.

To avoid the smearing of the correlation from p_T^{miss} and E_T^{miss} by the different track selections of tracks associated to τ_{had} and tracks used to calculate p_T^{miss}, tracks associated to τ_{had} candidates that fail criteria for p_T^{miss} calculation are added back to p_T^{miss} calculation. However, the effect is very small in this analysis because the τ_{had} associated track quality criteria is similar to the one in the p_T^{miss} calculation (section **??**).

6.7.2 New defined E_T^{miss} significance

Figure 6.9 shows the 2-dimensional distributions of E_T^{miss} versus Σp_T (left) and E_T^{miss} versus $0.5 \times \sqrt{\Sigma p_T}$ (right) of data overlaid with MC signal events, where E_T^{miss} and Σp_T are at the unit of GeV and the plots are obtained after lepton veto cut in the cut flow. Clearly, signal events mostly occupy the positions with relatively small Σp_T.

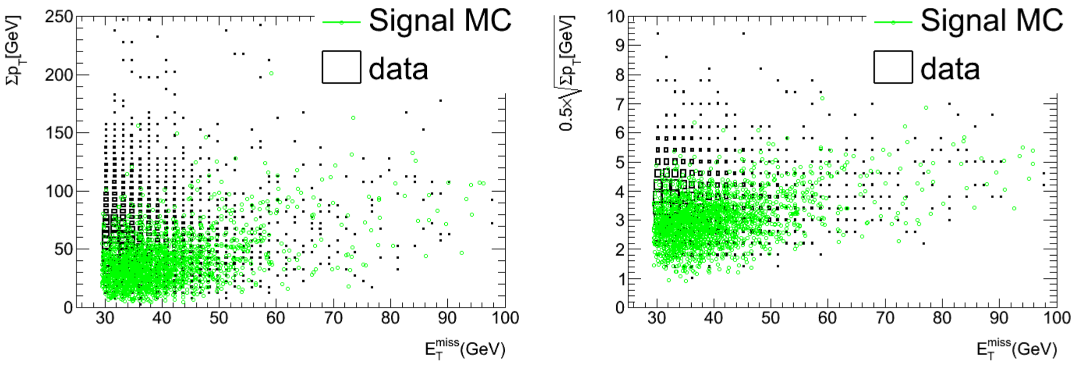

(a) (b)

Figure 6.9: 2-dimensional distributions of E_T^{miss} versus Σp_T (left) and E_T^{miss} versus $0.5 \times \sqrt{\Sigma p_T}$ (right) of data overlaid with MC signal events, where E_T^{miss} and Σp_T are at the unit of GeV and the plots are obtained after lepton veto cut in the cut flow.

Figure 6.10 shows the 1-dimensional distribution of $S^{new}_{E_T^{miss}}$ of data/MC comparison (left) and the 2-dimensional distribution of $S^{new}_{E_T^{miss}}$ versus transverse mass of W boson calculated from the leading-tight τ_{had} candidate and E_T^{miss} (right). In the left plot, QCD multi-jets background is not shown because of low statistics of the MC samples. However, QCD multi-jets background is not important in the region with large $S^{new}_{E_T^{miss}}$ where signal is dominated (e.g. regions with $S_{E_T^{miss}} > 13$).

6.7.2.1 Track selection for Σp_T calculation in the $S^{new}_{E_T^{miss}}$

To select tracks being from primary vertex, criteria are: $p_T > 1\ GeV$, $|d_0| < 1.5\ mm$, $|z_0| \cdot \sin(\theta) < 1.5\ mm$, Number of Pixel hits ≥ 1 and Number of SCT hits ≥ 7. Also, tracks associated to τ_{had} candidates failing previous criteria are added back to the $\sum p_T$ calculation. $p_T > 1\ GeV$ is required instead of $p_T > 500$ MeV in the p_T^{miss} to reduce the pile up dependence of Σp_T. Because position resolution for low p_T track is worse, involving low p_T tracks will involve tracks from near by pile up vertices, the pile up dependence of Σp_T will be increased. Figure 6.11 shows the resolution of parallel impact parameter z_0 versus track p_T (left) and its profile to the track p_T (right). Resolution of z_0 becomes worse quickly with decreasing of track p_T.

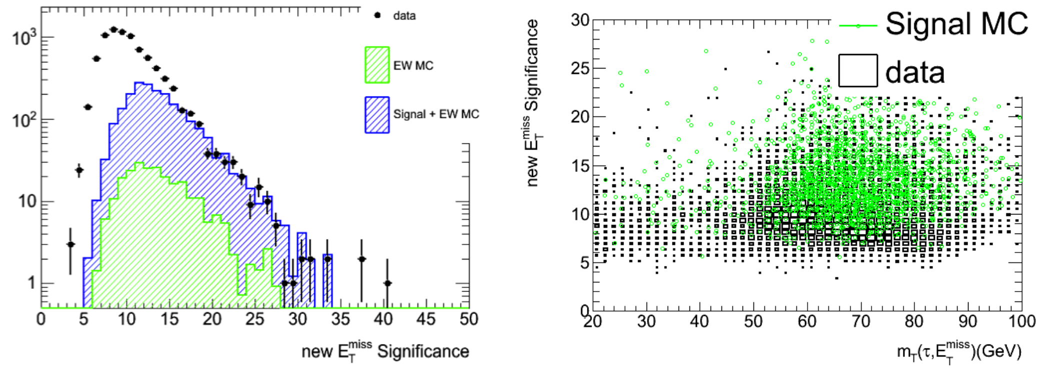

(a) (b)

Figure 6.10: $S^{new}_{E_T^{miss}}$ distribution comparing data and MC without QCD multi-jets MC samples being shown (left) and $S^{new}_{E_T^{miss}}$ versus transverse mass calculated from E_T^{miss} and the leading-tight τ_{had} for data and signal samples (right) after lepton veto.

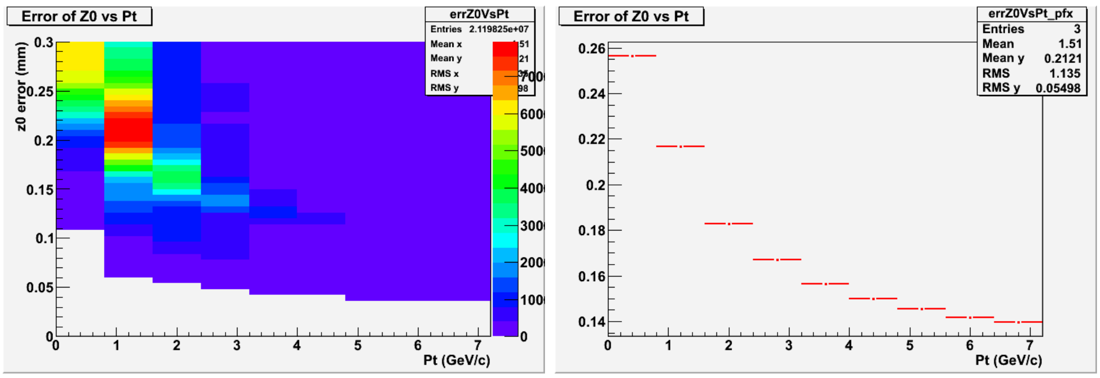

(a) (b)

Figure 6.11: The resolution of parallel impact parameter z_0 versus track p_T (left) and its profile to the track p_T (right).

6.7.3 Cut optimization of $\Delta\phi(E_T^{miss}, p_T^{miss})$ and $S^{new}_{E_T^{miss}}$ for $W \to \tau_{had}\nu$ signal selection

The cut optimization is studied using data period H1-I2 (runs from 166786 to 167844) and based on E_T^{miss} calibrated using Local Hadronic Calibration scheme [84]. To apply the $\Delta\phi(E_T^{miss}, p_T^{miss})$ and $S^{new}_{E_T^{miss}}$ into $W \to \tau_{had}\nu$ analysis, the optimized cut is $|\Delta\phi(E_T^{miss}, p_T^{miss})| < 0.6$ and $S^{new}_{E_T^{miss}} > 13$ for signal selection. The two cuts are optimized together. First, fix the $S^{new}_{E_T^{miss}}$ optimized cut and then scan $|\Delta\phi(E_T^{miss}, p_T^{miss})|$ cut value to get the most optimized cut for the variables.

Table 6.6 shows the numbers of data and signal by cutting on different values of $S^{new}_{E_T^{miss}}$ from 10 to 15 with 0.5 as one step. The background number equals to the counted data number subtracting the counted MC signal number. The optimization is done after lepton veto cut in the cut flow.

Cuts	Data	Signal	Background	S/B	$S/\sqrt{B}$
> 10	3773 ± 61	1666 ± 35	2111 ± 70	0.79 ± 0.03	36.3 ± 1.4
> 10.5	3217 ± 57	1576 ± 34	1641 ± 66	0.97 ± 0.04	38.9 ± 1.8
> 11	2753 ± 52	1485 ± 33	1268 ± 62	1.17 ± 0.06	41.7 ± 2.22747
> 11.5	2347 ± 48	1355 ± 31	992 ± 57	1.37 ± 0.08	43.0 ± 2.7
> 12	2050 ± 45	1232 ± 30	818 ± 54	1.51 ± 0.11	43.1 ± 3.0
> 12.5	1749 ± 42	1099 ± 28	650 ± 50	1.69 ± 0.14	43.1 ± 3.5
> 13	1491 ± 39	988 ± 27	303 ± 47	3.26 ± 0.52	56.8 ± 9.0
> 13.5	1271 ± 36	885 ± 25	386 ± 44	2.29 ± 0.27	45.0 ± 5.3
> 14	1081 ± 33	790 ± 24	291 ± 41	2.71 ± 0.39	46.3 ± 6.6
> 14.5	927 ± 30	693 ± 22	234 ± 37	2.96 ± 0.48	45.3 ± 7.3
> 15	773 ± 28	606 ± 21	167 ± 35	3.63 ± 0.77	46.9 ± 10.0

Table 6.6: Optimization of $S^{new}_{E_T^{miss}}$ cut for $W \to \tau_{had}\nu$ signal selection

$S^{new}_{E_T^{miss}} > 13$ gives the maximum $S/\sqrt{B}$ (S is the number of signal events from MC sample and B is the background number) and relative high S/B. Based on this, the cut on the $\Delta\phi(E_T^{miss}, p_T^{miss})$ is optimized by scanning its cut value from $|\Delta\phi(E_T^{miss}, p_T^{miss})| < 1.3$ to $|\Delta\phi(E_T^{miss}, p_T^{miss})| < 0.4$ with 0.1 as the step.

Table 6.7 shows the number corresponding to different cut on $|\Delta\phi(E_T^{miss}, p_T^{miss})|$. The background here is the same in table 6.6. The optimization is done with $S^{new}_{E_T^{miss}} > 13$. Even cut on $|\Delta\phi(E_T^{miss}, p_T^{miss})| < 0.5$ gives the highest $S/\sqrt{B}$ and S/B, we select 0.6 as the cut since we optimized again after the QCD background estimation (section 6.8).

Cuts	**Data**	**Signal**	**Background**	**S/B**	$S/\sqrt{B}$
$\|\Delta\phi(E_T^{miss}, p_T^{miss})\| < 1.3$	1317 ± 36	964 ± 26	353 ± 45	2.73 ± 0.35	51.3 ± 6.7
$\|\Delta\phi(E_T^{miss}, p_T^{miss})\| < 1.2$	1296 ± 36	959 ± 26	337 ± 45	2.85 ± 0.38	52.2 ± 7.1
$\|\Delta\phi(E_T^{miss}, p_T^{miss})\| < 1.1$	1278 ± 36	953 ± 26	325 ± 44	2.93 ± 0.41	52.9 ± 7.4
$\|\Delta\phi(E_T^{miss}, p_T^{miss})\| < 1.0$	1258 ± 35	945 ± 26	313 ± 44	3.02 ± 0.43	53.4 ± 7.7
$\|\Delta\phi(E_T^{miss}, p_T^{miss})\| < 0.9$	1223 ± 35	937 ± 26	286 ± 44	3.28 ± 0.51	55.4 ± 8.6
$\|\Delta\phi(E_T^{miss}, p_T^{miss})\| < 0.8$	1200 ± 35	920 ± 26	280 ± 43	3.29 ± 0.51	50.5 ± 8.6
$\|\Delta\phi(E_T^{miss}, p_T^{miss})\| < 0.7$	1162 ± 34	897 ± 25	265 ± 43	3.38 ± 0.55	55.1 ± 9.0
$\|\Delta\phi(E_T^{miss}, p_T^{miss})\| < 0.6$	1120 ± 33	873 ± 25	247 ± 42	3.53 ± 0.61	55.5 ± 9.5
$\|\Delta\phi(E_T^{miss}, p_T^{miss})\| < 0.5$	1063 ± 33	843 ± 25	220 ± 41	3.83 ± 0.72	56.8 ± 10.7
$\|\Delta\phi(E_T^{miss}, p_T^{miss})\| < 0.4$	956 ± 31	753 ± 23	203 ± 39	3.71 ± 0.72	52.9 ± 10.2

Table 6.7: Optimization of $\Delta\phi(E_T^{miss}, p_T^{miss})$ cut for $W \to \tau_{had}\nu$ signal selection

6.7.4 Cut flow

Tables 6.8, 6.9 and 6.10 show the cut flow for all the data used in the analysis. Cut flow for EW backgrounds and signal are also shown in the same table, where the MC numbers are after vertices re-weighting (section 6.2.3.1). Table 6.8 is for period D3H1, table 6.9 if period H1I and table 6.10 is for all the data by adding the numbers from periods D3H1 and H1I.

Cuts	**Data**	$\boldsymbol{W \rightarrow \tau_{lep}\nu}$	$\boldsymbol{W \rightarrow e\nu}$	$W \rightarrow \mu\nu$	$W \rightarrow \tau_{lep}\nu$	$Z \rightarrow ee$	$Z \rightarrow \mu\mu$	$Z \rightarrow \tau\tau$
Total	170804046	83044	127977	127679	45332	12625	12098	12245
GRL	148550544	83944	127977	127679	45332	12625	12098	12245
Trigger	4503441	10577 ± 31	67807 ± 16	3285 ± 5	3588 ± 18	1022 ± 0.4	404 ± 0.2	1317 ± 1
Vertex requirement	4503417	10577 ± 31	67807 ± 16	3285 ± 5	3588 ± 18	1022 ± 0.4	404 ± 0.2	1317 ± 1
Jet Cleaning	4499393	10577 ± 31	67807 ± 16	3285 ± 5	3588 ± 18	1022 ± 0.4	404 ± 0.2	1317 ± 1
Jet Veto	3293302	8578 ± 28	55194 ± 16	2638 ± 5	2921 ± 16	653 ± 0.3	326 ± 0.2	1031 ± 1
$\Delta\phi(Jet, E_T^{miss})$	1838752	8123 ± 28	53396 ± 16	2386 ± 4	2758 ± 16	360 ± 0.2	258 ± 0.2	823 ± 1
E_T^{miss}	291887	6759 ± 26	38403 ± 15	1863 ± 4	1698 ± 13	8 ± 0.03	52 ± 0.1	442 ± 1
τ-ID	73565	2422 ± 16	24700 ± 13	413 ± 2	894 ± 9	5 ± 0.03	13 ± 0.04	195 ± 0.4
$\tau - E_T$	34957	1890 ± 14	23002 ± 13	209 ± 1	632 ± 8	4 ± 0.02	6.5 ± 0.03	119 ± 0.3
$\tau - \eta$	34957	1890 ± 14	23002 ± 13	209 ± 1	632 ± 8	4 ± 0.02	4 ± 0.02	119 ± 0.3
τ lepton veto	10648	1590 ± 13	208 ± 1	158 ± 1	40 ± 2	0.05 ± 0.003	1 ± 0.01	86 ± 0.3
Lepton veto	8999	1442 ± 12	71 ± 1	37 ± 1	16 ± 1	0 ± 0	0.6 ± 0.01	55 ± 0.2
$\Delta\phi(E_T^{miss}, p_T^{miss})$	3825	1258 ± 11	49 ± 0.6	30 ± 1	12 ± 1	0 ± 0	0.6 ± 0.01	46 ± 0.2
$S^{new}_{E_T^{miss}}$	1007	723 ± 9	30 ± 0.5	17 ± 0.3	8 ± 1	0 ± 0	0.3 ± 0.01	18 ± 0.1

Table 6.8: Cut flow for data, signal and EW MC background samples corresponding to period D3H1 (run 158632 to 166658).

Cuts	**Data**	$\boldsymbol{W \to \tau_{lep}\nu}$	$\boldsymbol{W \to e\nu}$	$W \to \mu\nu$	$W \to \tau_{lep}\nu$	$Z \to ee$	$Z \to \mu\mu$	$Z \to \tau\tau$
Total	29091369	166164	256404	257070	90300	24546	24320	24269
GRL	26721160	166164	256404	257070	90300	24546	24319.6	24268.9
Trigger	2849976	11360 ± 67	121342 ± 46	2853 ± 10	4580 ± 41	1472 ± 1	367 ± 0.5	1603 ± 2
Vertex requirement	2849950	11360 ± 67	121342 ± 46	2853 ± 10	4580 ± 41	1472 ± 1	367 ± 0.5	1603 ± 2
Jet Cleaning	2847652	11360 ± 67	121342 ± 46	2853 ± 10	4580 ± 41	1472 ± 1	367 ± 0.5	1603 ± 2
Jet Veto	2017106	9199 ± 60	98941 ± 45	2284 ± 9	3744 ± 38	926 ± 1	295 ± 0.4	1249 ± 2
$\Delta\phi(Jet, E_T^{miss})$	1051035	8609 ± 59	95635 ± 45	2054 ± 8	3523 ± 37	499 ± 0.5	230 ± 0.4	990 ± 2
E_T^{miss}	198030	7388 ± 55	71577 ± 42	1594 ± 7	2254 ± 29	15 ± 0.1	47 ± 0.2	553 ± 1
τ-ID	75916	2936 ± 35	46378 ± 36	430 ± 4	1324 ± 23	10 ± 0.1	14 ± 0.1	256 ± 1
$\tau - E_T$	56900	2487 ± 32	43803 ± 35	257 ± 3	1096 ± 21	7 ± 0.1	9 ± 0.1	179 ± 1
$\tau - \eta$	56900	2487 ± 32	43803 ± 35	257 ± 3	1096 ± 21	7 ± 0.1	9 ± 0.1	179 ± 1
τ lepton veto	10734	2094 ± 29	357 ± 3	187 ± 3	39 ± 4	0.1 ± 0.01	5 ± 0.05	123 ± 0.7
Lepton veto	9023	1905 ± 28	111 ± 2	44 ± 1	15 ± 2	0 ± 0	1 ± 0.02	78 ± 0.5
$\Delta\phi(E_T^{miss}, p_T^{miss})$	4112	1673 ± 26	81 ± 2	35 ± 1	12 ± 2	0 ± 0	0.7 ± 0.02	64 ± 0.5
$S^{new}_{E_T^{miss}}$	1336	1008 ± 21	52 ± 1	21 ± 0.8	8 ± 2	0 ± 0	0.4 ± 0.01	26 ± 0.3

Table 6.9: Cut flow for data, signal and EW MC background samples corresponding to period H1I (run 166786 to 167844).

Cuts	**Data**	$\boldsymbol{W \to \tau_{lep}\nu}$	$\boldsymbol{W \to e\nu}$	$W \to \mu\nu$	$W \to \tau_{lep}\nu$	$Z \to ee$	$Z \to \mu\mu$	$Z \to \tau\tau$
Total	199895415	249208	384381	384749	135632	37171	36418	36514
GRL	175271704	249208	384381	384749	135632	37171	36418	36514
Trigger	7353417	21937 ± 74	189149 ± 49	6138 ± 11	8168 ± 45	2494 ± 1	771 ± 1	2920 ± 2
Vertex requirement	7353367	21937 ± 74	189149 ± 49	6138 ± 11	8168 ± 45	2494 ± 1	771 ± 1	2920 ± 2
Jet Cleaning	7347045	21937 ± 74	189149 ± 49	6138 ± 11	8168 ± 45	2494 ± 1	771 ± 1	2920 ± 2
Jet Veto	5310408	17777 ± 66	154135 ± 48	4922 ± 10	6665 ± 41	1579 ± 1	621 ± 0.4	2280 ± 2
$\Delta\phi(Jet, E_T^{miss})$	2889787	16732 ± 65	149031 ± 48	4440 ± 9	6281 ± 40	859 ± 1	488 ± 0.4	1813 ± 2
E_T^{miss}	489917	14147 ± 61	109980 ± 45	3457 ± 8	3952 ± 32	23 ± 0.1	99 ± 0.2	995 ± 1
τ-ID	149481	5358 ± 38	71078 ± 38	843 ± 4	2218 ± 25	15 ± 0.1	27 ± 0.1	451 ± 1
$\tau - E_T$	91857	4377 ± 35	66805 ± 37	466 ± 3	1728 ± 22	11 ± 0.1	16 ± 0.1	298 ± 1
$\tau - \eta$	91857	4377 ± 35	66805 ± 37	466 ± 3	1728 ± 22	11 ± 0.1	13 ± 0.1	298 ± 1
τ lepton veto	21382	3684 ± 32	565 ± 3	345 ± 3	79 ± 4	0.2 ± 0.01	6 ± 0.1	209 ± 1
Lepton veto	18022	3347 ± 30	182 ± 2	81 ± 1	31 ± 2	0	2 ± 0.02	133 ± 1
$\Delta\phi(E_T^{miss}, p_T^{miss})$	7937	2931 ± 28	130 ± 2	65 ± 1	24 ± 2	0	1 ± 0.02	110 ± 1
$S^{new}_{E_T^{miss}}$	2343	1731 ± 23	82 ± 1	38 ± 1	16 ± 2	0	0.7 ± 0.01	44 ± 0.3

Table 6.10: Cut flow for data, signal and EW MC background samples corresponding to all the data (run 158632 to 167844).

6.7.5 Performance of the new methods

The increasing of the LHC instantaneous luminosity makes the pile up effects on this analysis non-negligible. It is reflected on the variables distribution under different number of vertices in the events. Figure 6.12 shows the distributions of $E^{old}_{T^{miss}}$, ΣE_T and E_T^{miss} dependence on number of vertices in data sample. The vertices are all required to have ≥ 3 associated tracks. Large dependence on pile up is found for $E^{old}_{T^{miss}}$ and ΣE_T, while E_T^{miss} shows less dependence. That is because collisions from pile up mainly produce particles with low p_T and E_T. ΣE_T adds every particles that deposit energy in the calorimeter, even the particles are from pile up collisions. E_T^{miss} is less effected because it is the vector sum of the particles E_T and small E_T^{miss} value is expected from pile up collisions.

p_T^{miss} has similar behavior as E_T^{miss} because it is vector sum of the tracks. Therefore, the pile up dependence is small for p_T^{miss}. Figure 6.13 shows the p_T^{miss} for events with different number of vertices in data sample.

Using the $S^{new}_{E_T^{miss}}$, the pile up effects are reduced very much. Figure 6.14 shows a) $E^{new}_{T^{miss}}$ and b) Σp_T dependence on different number of vertices in data sample. Comparing to figure 6.12, the shapes of $S^{new}_{E_T^{miss}}$ and Σp_T have no much difference under different number of vertices.

Table 6.11 shows the fraction of selected events number after to before applying $S^{old}_{E_T^{miss}}$ ($S^{new}_{E_T^{miss}}$) under different number of vertices. In the single vertex events, $S^{old}_{E_T^{miss}}$ save about 45% percent of events before applying it, while in the high pile up events, only 2% of events are saved in the data sample. The signal selection efficiency for $S_{E_T^{miss}}$ goes down to 14% from 76%. While the selection efficiency for $S^{new}_{E_T^{miss}}$ shows stable ratio both for data and signal MC samples, especially for the signal selection efficiencies are around 60% for different number of vertices.

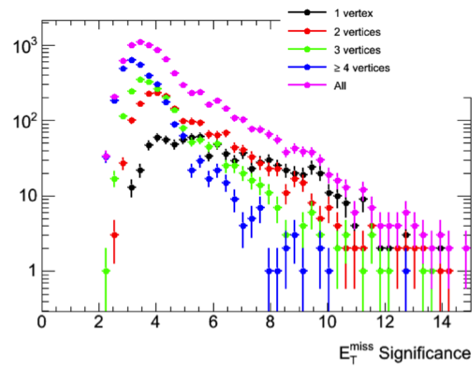

(a)

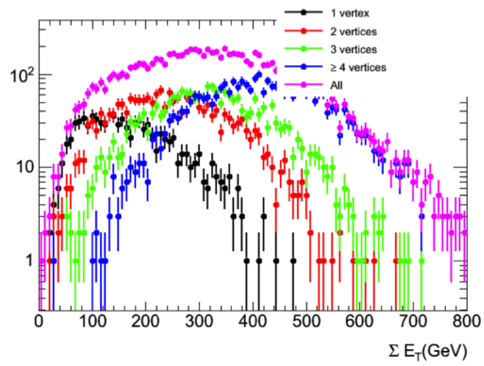

(b)

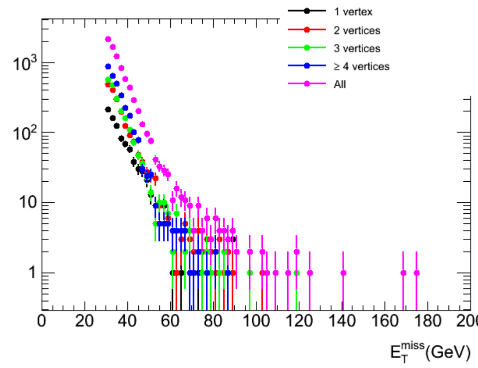

(c)

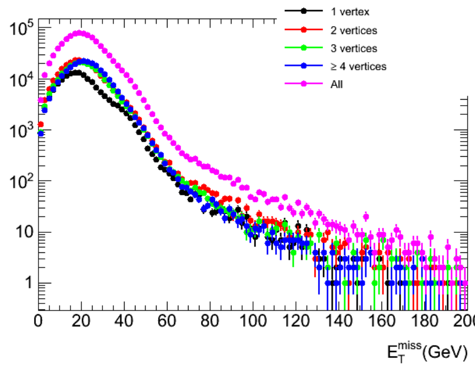

(d)

Figure 6.12: Pile up dependence of $E_{T miss}^{old}$, ΣE_T and E_T^{miss}, which is checked by plotting the variables distribution with different number of vertices in data sample. The a) $E_{T miss}^{old}$, b) ΣE_T and c) E_T^{miss} pile up dependence are obtained after lepton veto but before $E_{T miss}^{old}$ cut. The d) E_T^{miss} pile up dependence after pre-selection but before E_T^{miss} cut. These pile up dependence distributions are obtained from data and without normalization.

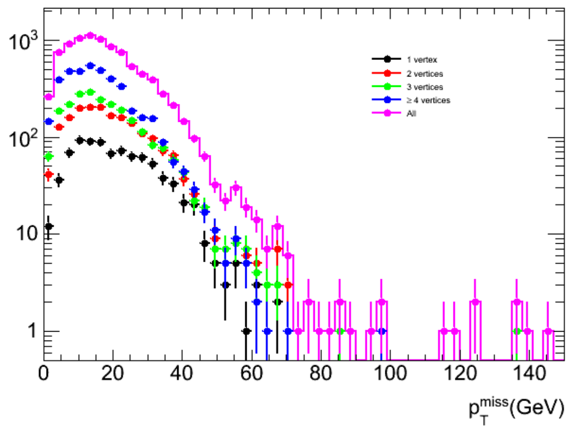

(a)

Figure 6.13: The p_T^{miss} distributions for events with different number of vertices in data sample.

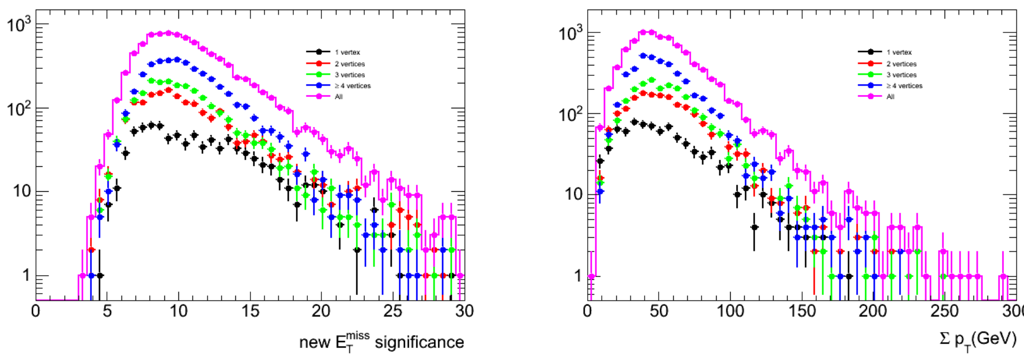

(a) (b)

Figure 6.14: a) $S^{new}_{E_T^{miss}}$ and b) Σp_T dependence on different number of vertices in data sample.

Number of vertices	Ratio after/before		
		data	**Signal**
1 vertex	$\boldsymbol{S^{new}_{E_T^{miss}}}$	0.34	0.57
	$S_{E_T^{miss}}$	0.45	0.76
2 vertices	$\boldsymbol{S^{new}_{E_T^{miss}}}$	0.24	0.58
	$S_{E_T^{miss}}$	0.21	0.49
3 vertices	$\boldsymbol{S^{new}_{E_T^{miss}}}$	0.19	0.59
	$S_{E_T^{miss}}$	0.08	0.31
$\geq$ 4 vertices	$\boldsymbol{S^{new}_{E_T^{miss}}}$	0.20	0.63
	$S_{E_T^{miss}}$	0.02	0.14

Table 6.11: Pile up dependence of the cuts efficiency of $S^{old}_{E_T^{miss}}$ and $S^{new}_{E_T^{miss}}$.

6.8 QCD multi-jets background estimation

A QCD multi-jets background estimation algorithm called "ABCD method" is implemented in this analysis. The method estimates QCD multi-jets background in the signal region from background control regions. The background control regions and signal region are established by dividing a 2-dimensional plot into four regions (denoted as A, B, C and D region respectively). The x and y axises of the 2-dimensional plot are from two of the variables for signal selection in the cut flow.

Figure 6.15 shows a sketch of the 2-dimensional plot, where we define region A as signal region, while regions B, C and D as QCD multi-jets background dominated regions. Line 2 and 4 are movable to change the signal contamination in B, C and D regions.

To use the ABCD method, two conditions need to be satisfied. First, the two variables establishing the 2-dimensional plot should not have correlation between them for the background events. Second, background control regions B, C and D should have negligible signal and other non-QCD backgrounds contamination [71]. Then the QCD

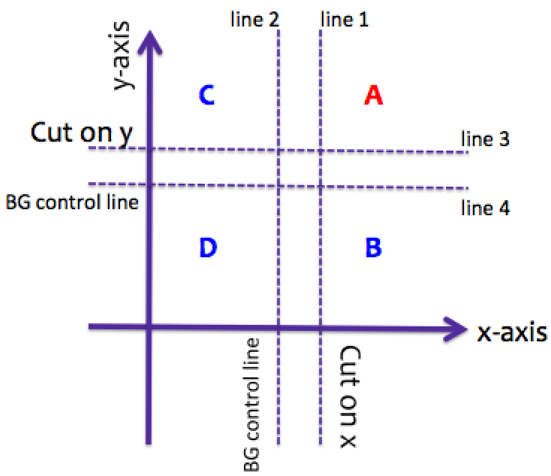

(a) a

Figure 6.15: A sketch of 2-dimensional plot showing the regions deviation. Where region A is signal region, while region B, C and D are background regions.

background in signal region (region A) is estimated based on this formula:

$$N_A = \frac{N_B \cdot N_C}{N_D}, \tag{6.3}$$

The first condition can be checked by comparing one of the variables shapes requiring the other variable pass or fail the signal selection cut. But if signal contamination in background region is not negligible, correction for this contamination need to be considered into formula 6.3. Assuming signal events from MC in region A, B, C and D are S_A, S_B, S_C and S_D, respectively (Same assumption for non-QCD background (EW): EW_A, EW_B, EW_C and EW_D). Ratios of non-QCD events (including signal and EW) in the background regions to the signal region are denoted as:

$$c_i = \frac{S_i + EW_i}{S_A + EW_A}, \tag{6.4}$$

where i denotes background regions B, C and D.

QCD multi-jets background numbers in each background region after non-QCD contamination correction are:

$$N_B^{corr} = N_B - c_B \cdot N_A^{non-QCD}, N_C^{corr} = N_C - c_C \cdot N_A^{non-QCD}, N_D^{corr} = N_D - c_D \cdot N_A^{non-QCD}, \tag{6.5}$$

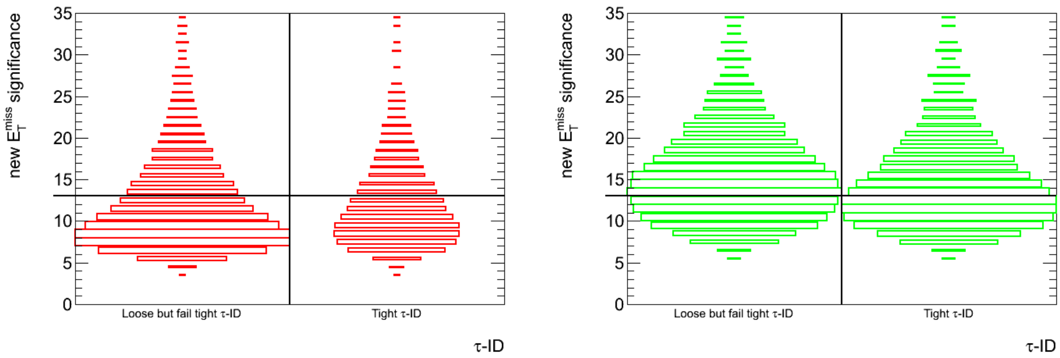

(a) (b)

Figure 6.16: 2-dimensional plot of $\tau_{had} - ID$ and $S^{new}_{E_T^{miss}}$, where x-axis is $\tau_{had} - ID$ and y-axis is $S^{new}_{E_T^{miss}}$. Left plot is for data sample and right plot is for signal sample.

where $N_A^{non-QCD}$ is non-QCD events in region A from MC. It is $S_A + EW_A$. Formula 6.3 is changed to:

$$N_A^{QCD} = \frac{(N_B - c_B \cdot N_A^{non-QCD}) \cdot (N_C - c_c \cdot N_A^{non-QCD})}{N_D - c_D \cdot N_A^{non-QCD}}, \quad (6.6)$$

where N_A^{QCD} is the estimated QCD background in signal region A.

In this analysis the two variables used in the ABCD method are $\tau_{had} - ID$ vs $S^{new}_{E_T^{miss}}$. $\tau_{had} - ID$ and $S^{new}_{E_T^{miss}}$ are both variables used in the cut flow and powerfully distinguish QCD mult-jets background and signal. 2-dimensional plot from these two variables is show in figure 6.16. Left plot is the $\tau - ID$ versus $S^{new}_{E_T^{miss}}$ for data sample and right plot is the $\tau - ID$ versus $S^{new}_{E_T^{miss}}$ for the MC signal sample.

The A, B, C and D regions are defined as (all the regions have passed the event selection criteria except the two):

- **Region A:** Signal region with events passing tight $\tau_{had} - ID$ and $S^{new}_{E_T^{miss}} > 13$.
- **Region B:** Background region with events passing tight $\tau_{had} - ID$ but $S^{new}_{E_T^{miss}} < 13$.
- **Region C:** Background region with events passing loose but fail tight $\tau_{had} - ID$ and $S^{new}_{E_T^{miss}} > 13$.

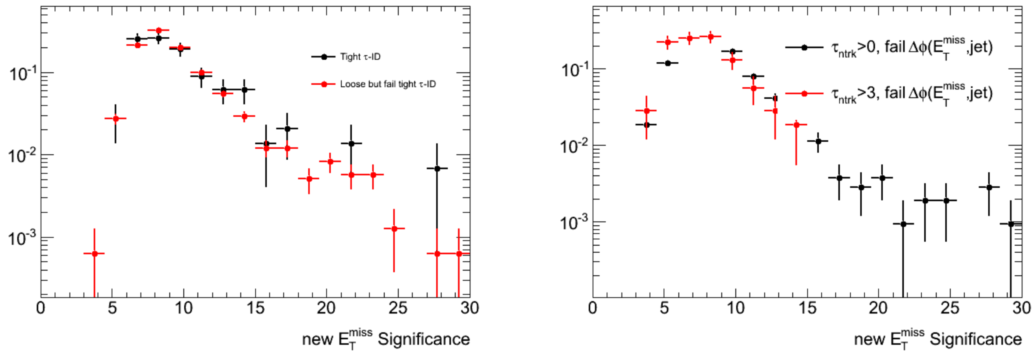

(a) (b)

Figure 6.17: Correlation check of the two variables used in the ABCD method. Left plot is he $S^{new}_{E_T^{miss}}$ distributions comparing background sample with loose but fail tight $\tau_{had} - ID$ and tight $\tau_{had} - ID$, where the background sample is obtained from data by requiring tracks number associated to τ_{had} larger than 3 and right plots is the $S^{new}_{E_T^{miss}}$ shapes in the background region with τ associated number > 4 and > 0, where the background control sample is obtained in the data sample by reversing the $\Delta\phi(jet, E_T^{miss})$ cut.

- **Region D:** Background region with events passing loose but fail tight $\tau_{had} - ID$ and $S^{new}_{E_T^{miss}} < 13$.

The correlation between these two variables is checked by comparing the shapes of $S^{new}_{E_T^{miss}}$ under different $\tau_{had} - ID$ requirements. Figure 6.17 shows the $S^{new}_{E_T^{miss}}$ distributions comparing background sample with loose but fail tight $\tau_{had} - ID$ and tight $\tau_{had} - ID$ (left). The background sample is obtained from data by requiring the tracks number associated to τ_{had} larger than 3. The right plot shows the $S^{new}_{E_T^{miss}}$ shapes in the background control sample with τ associated number > 4 and > 0. The background control sample is obtained in the data by reversing the $\Delta\phi(jet, E_T^{miss})$ cut (events that are having $|\Delta\phi(jet, E_T^{miss}| < 0.5$ with jet $p_T > 20$ GeV). The shapes are consistent with each other within statistical uncertainties.

Table 6.12, 6.13 and 6.14 provide the numbers in different control regions of data and MC samples for period D3H1, H1I and all the data.

	A	B	C	D
data	1007 ± 32	2818 ± 53	2766 ± 53	11904 ± 109
signal	723 ± 9	534 ± 7	1131 ± 11	492 ± 7
EW	70 ± 1	62 ± 0.8	214 ± 2	73 ± 1
ci		0.75 ± 0.07	1.70 ± 0.15	0.71 ± 0.06

Table 6.12: Events number in different regions for data and MC using $\tau_{had} - ID$ and $S^{new}_{E_T^{miss}}$ as the variables to estimate QCD background for data period D3H1 (run 158632 to 166658).

	A	B	C	D
Data	1336 ± 37	2776 ± 53	1421 ± 38	5782 ± 76
Signal (MC)	1008 ± 20	665 ± 16	536 ± 3	232 ± 2
EW (MC)	105 ± 2	85 ± 1	100 ± 0.3	33 ± 0.2
c_i		0.67 ± 0.07	0.57 ± 0.06	0.2 ± 0.02

Table 6.13: Events number in different regions for data and MC using $\tau_{had} - ID$ and $S^{new}_{E_T^{miss}}$ as the variables to estimate QCD background for data period H1I (run 166786 to 167844).

	A	B	C	D
Data	2343 ± 49	5594 ± 75	4187 ± 65	17686 ± 133
Signal (MC)	1731 ± 22	1199 ± 17	1667 ± 11	724 ± 7
EW (MC)	175 ± 2	147 ± 1	314 ± 2	106 ± 1

Table 6.14: Events number in different regions for data and MC using $\tau_{had} - ID$ and $S^{new}_{E_T^{miss}}$ as the variables to estimate QCD background for all the data (run 158632 to 167844). The numbers are the sum of period D3H1 and H1I and the uncertainties are only statistical calculated using error propagation.

Signal and EW contamination is not negligible in background control region B, C and D (especially in B and C). The QCD background is obtained by solving formula 6.6.

The estimated QCD multi-jets background, signal and EW background number in region A is listed in table 6.15. The numbers are the sum of period D3H1 and H1I and the uncertainties are only statistical calculated using error propagation. At last we get 624 ± 45 QCD background in signal region.

Period	Signal	QCD	EW
D3H1	621 ± 55	326 ± 34	60 ± 6
H1I	924 ± 53	316 ± 30	96 ± 6
All	1545 ± 76	642 ± 45	156 ± 8

Table 6.15: Estimated QCD background in signal region A using $\tau_{had} - ID$ and $S^{new}_{E_T^{miss}}$ as the variables to estimate QCD background.

Figures 6.18, 6.19 and 6.20 show the data and MC comparison for the variables used in the analysis. The QCD multi-jets events are extracted from the background regions and normalized to the estimated QCD multi-jets background in signal region. The non-QCD backgrounds are from MC sample in region A. The data and MC comparisons are implemented on period D3H1 and H1I separately. Figure 6.18 includes the τ_{had} related variables: the p_T, R_{track}, number of associated tracks and charge distribution. Figures 6.19 and 6.20 include the missing transverse momentum variables: $S^{new}_{E_T^{miss}}$, E_T^{miss}, p_T^{miss}, $\Delta\phi(E_T^{miss}, p_T^{miss})$ and ΣE_T. These plots show the data and MC comparison for period H1I.

6.9 Preliminary results of cross section

The cross section is calculated according to the formula [88]:

$$\sigma_W = \frac{N_{obs} - N_{bkg}}{Acc \cdot \int \mathcal{L} dt}, \tag{6.7}$$

where N_{obs} is the observed events in the data, N_{bkg} is the estimated backgrounds events, Acc is the acceptance of the signal and $\int \mathcal{L} dt$ is the integrated luminosity collected by ATLAS after the trigger selection.

The acceptance is defined as:

$$Acc = \frac{N_{MCsignal,reconstruction,selection}}{N_{MCsignal,generation,all}}, \tag{6.8}$$

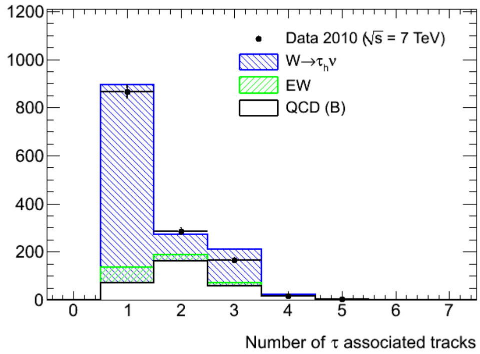

(a)

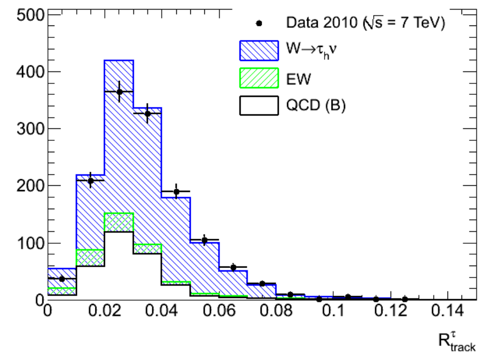

(b)

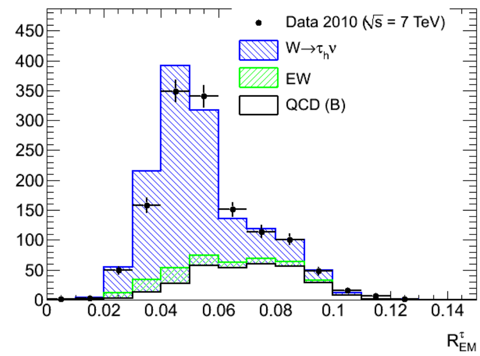

(c)

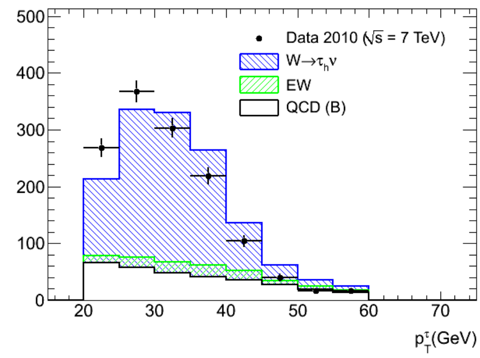

(d)

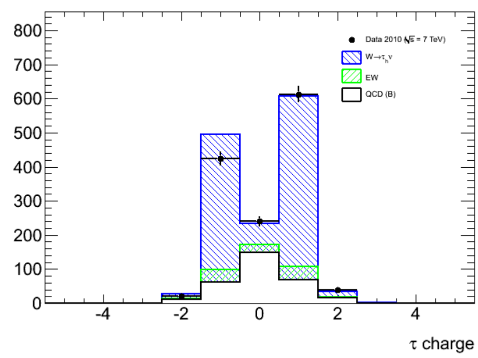

(e)

Figure 6.18: Data and MC comparison for τ variables, where the QCD background is extracted from region B. a) Number of associated tracks to the τ, b) R^{τ}_{track}, c) R^{τ}_{EM}, d) p^{τ}_{T} and e) τ_{charge}.

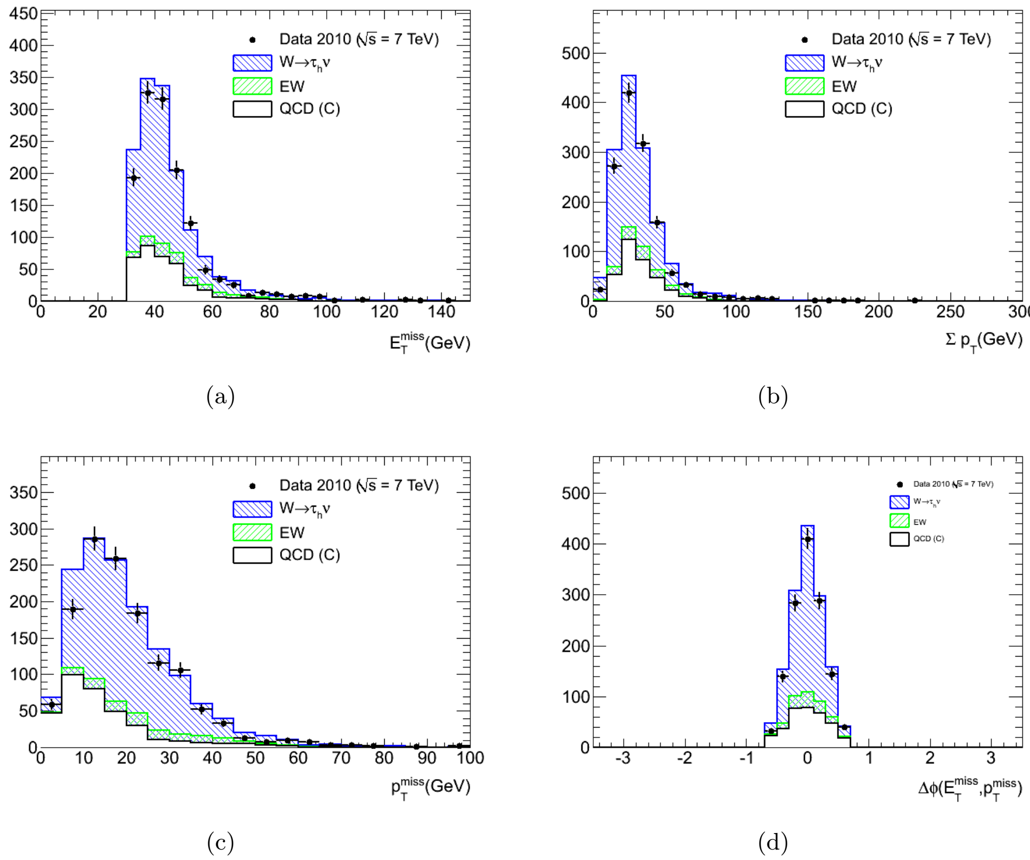

Figure 6.19: Data and MC comparison for event selection related variables, where the QCD background is extracted from region C. a) E_T^{miss}, b) Σp_T, c) p_T^{miss} and d) $\Delta\phi(E_T^{miss}, p_T^{miss})$.

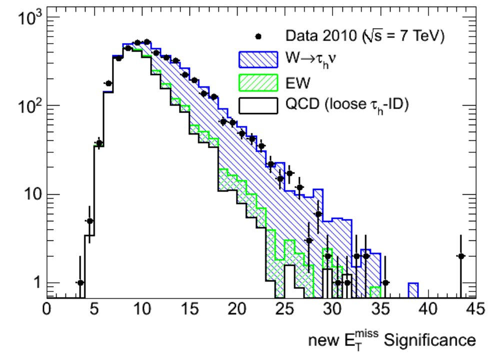

(a)

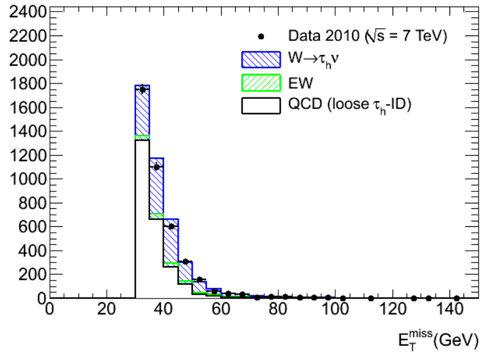

(b)

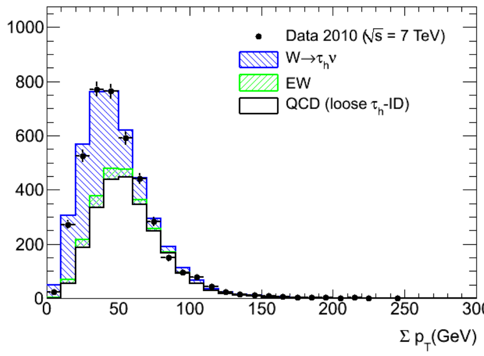

(c)

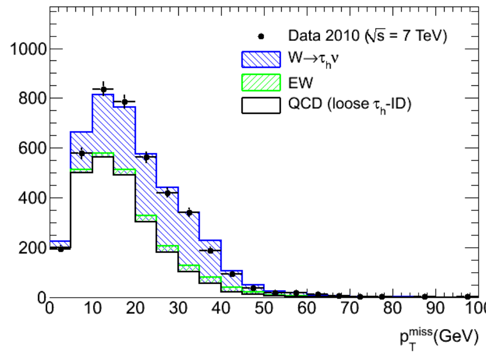

(d)

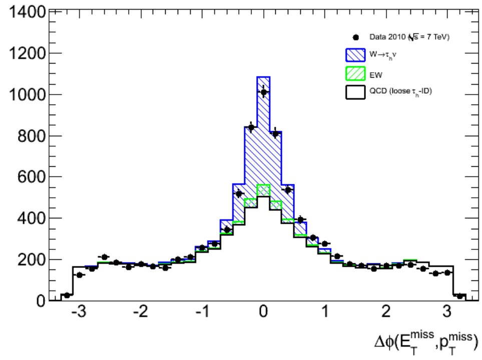

(e)

Figure 6.20: Data and MC comparison for event selection related variables, where the QCD background is extracted from region C and D. a) Number of associated tracks to the $S^{new}_{E_T^{miss}}$, b) E_T^{miss}, c) Σp_T, d) p_T^{miss} and e) $\Delta\phi(E_T^{miss}, p_T^{miss})$ (not cut on it just have an idea how it looks like).

where $N_{MCsignal,generation,all}$ is the number of all the generated events in signal sample and $N_{MCsignal,reconstruction,selection}$ is the total number of events after reconstruction and event selection (section 6.6).

The acceptance can be written into two parts. The two parts are defined as [17]:

$$A_W = \frac{N_{MCsignal,generation,cut}}{N_{MCsignal,generation,all}} \tag{6.9}$$

$$C_W = \frac{N_{MCsignal,reconstruction,selection}}{N_{MCsignal,generation,cut}} \tag{6.10}$$

where

- A_W is the fiducial acceptance, C_W is the factorized correction between data and MC of any discrepancy in trigger efficiency, reconstruction and selection.
- $N_{MCsignal,generation,cut}$ is the number of signals after the fiducial cuts at the generation level in the signal MC sample.

Since we are using different trigger in the analysis for different period of data, the cross section is calculated period by period and combine together at last. Table 6.16 shows the cross section for different periods and the combined results. In the table only statistic uncertainty is shown. In this table, the acceptance is calculated according to equation 6.8. For the final results the cross section and systematic uncertainties will be obtained according to equation 6.10.

	Acc	$\boldsymbol{\sigma_{W\to\tau\nu}}$ (nb)	Remarks
D3H1	0.0087 ± 0.0002	5.82 ± 0.44	Statistic uncertainty only
H1I	0.0061 ± 0.0002	6.22 ± 0.32	Statistic uncertainty only
All	0.0075 ± 0.0001	5.96 ± 0.26	Statistic uncertainty only

Table 6.16: The cross section measured period by period and the combined results. Only statistic uncertainty is shown.

6.9.1 Systematic uncertainties

Systematic uncertainties come from all the systems in equations 6.8 to 6.10. Table 6.17 shows the systematic uncertainties list, that will be considered in the cross section measurement.

Factor	Source
N_{bkg}	Correlation of the two variables in ABCD method
	Signal contamination in background region of the ABCD method
	Background regions definition
A_W	Parton Distribution Functions (PDFs) [87]
	Geometry cut (η)
	Kinematic cut (E_T^{miss})
	Kinematic cut (τp_T)
C_W	Trigger efficiency
	Jet fake as τ_{had} rate
	Electron fake as τ_{had} rate
	τ_{had} reconstruction efficiency
	τ_{had} identification ($\tau_{had} - ID$) efficiency
	τ_{had} energy scale
	E_T^{miss} energy scale
	Jet cleaning
	MC tune
	Vertex reweighting weight
	Track efficiency
	Track resolution
	Vertex resolution
	Pile up

Table 6.17: List of the systematic uncertainties need to be measured in the cross section measurement.

Several systematic uncertainties have been studied:

- The systematic uncertainty from the background regions definition of the ABCD method. This systematic uncertainty is obtained by changing line 4 (figure 6.15) to smaller values than the signal cut 13 on $S^{new}_{E_T^{miss}}$. The change is required to be within the resolution of $S^{new}_{E_T^{miss}}$. To be safe, line 4 is changed to $S^{new}_{E_T^{miss}} = 9$. Therefore, regions A and C in figure 6.16 is not changed but region B and D is changed that the $S^{new}_{E_T^{miss}}$ is smaller than 9. The systematic uncertainty is found to be around 1%.

- The systematic uncertainty from MC vertex re-weighting. This systematic is obtained by re-weighting the MC samples at different event selection level: after jet cleaning (default) and after lepton veto. After jet cleaning cut, the events from data include all the physics processes, while the signal fraction is largely increased after lepton veto. The systematic uncertainty obtained this way is around 1%.
- The systematic uncertainty from luminosity measurement is 3.4% [89].
- The systematic uncertainty from τ_{had} energy scale is 10% at most [90]. It is provided by the tau performance work group. The systematic uncertainties are applied according to the τ_{had} p_T, η and number of associated tracks. p_T between 20 and 30GeV, $|\eta| < 1.3$ and multi-prongs of τ_{had} gives the largest uncertainty 10%.

The cross section measurement is undergoing. Therefore, not all the the systematic uncertainties listed in table 6.17 are obtained.

6.10 Summary

In this analysis, the importance of $W \to \tau\nu$ has been illustrated that it is not only for many new particles predicted in theory but also important for checking SM at high energy scale, as well important for checking the performance of τ_{had} identification.

Two new methods have been introduced aiming to measure the cross section of $W \to \tau\nu$ at ATLAS. The the correlation track-based missing transverse momentum (p_T^{miss}) and calorimeter-based missing transverse momentum (p_T^{miss}) is used to reject the background with fake E_T^{miss} (like QCD multi-jets events). It utilizes that, in the events with real E_T^{miss}, the independent measurements from tracks and calorimeter objects have strong correlation. The new defined E_T^{miss} significance is to reduce the pile up effects (pile up effects are important at LHC with such high instantaneous luminosity) that the old E_T^{miss} significance faces. Its principle is that the $\sum p_T$ can be reconstructed vertex-based that the pile up vertices do not effect that much to the collision vertex with interesting physics. Using ABCD method the estimated QCD multi-jets background has proved to be 642 ± 45 (statistical error only) with the estimated signal number1545 ± 76 (statistical error only). The cross section of $W \rightarrow \tau\nu \rightarrow \tau_{had}\nu$ has been preliminarily estimated to be 5.96 ± 0.26 nb (statistical error only).

7

Summary and outlook

The work presented in this thesis has shown the ATLAS calorimeter performance, as well as the hadronic τ lepton reconstruction and identification, its (τ lepton) application to the selection of the $W \rightarrow \tau\nu$ signal using collision data at center-of-mass energy 7 TeV and preliminary measurement of the cross section using the data collected in the 2010 with an integrated luminosity 36.8 pb^{-1}.

The calorimeters response and resolution to pions using test beam data collected in 2004 have been discussed in chapter 4. The noise of the calorimeter cells has been studied. The average noise value of each layer has been found to be: 12 MeV in the presampler, 12 MeV in the first layer, 28 MeV in the second layer and 22 MeV in the third layer of the LAr, 30 MeV in the first layer, 30 MeV in the second layer and 25 MeV in the third layer of the tile calorimeter. Timing of the LAr calorimeter is studied and found to be within 5 ns for good runs. Calorimeter response and resolution to both VLE and HE pions have been studied. Low energy resolution has been improved using topo-clusters. In addition, calorimeter response to HE pions increases with the injection energy and slightly different from their η positions. The resolution is linear with respect to the $1/\sqrt{E_{beam}}$.

τ_{had} reconstruction and identification algorithms have been studied and optimized with MC and data events. τ_{had} signal efficiencies of cut-based identification method have been proved to be 30%, 50% and 60% for tight, medium and loose identification level respectively and background rejection factor in an order of hundred for the tight level. Multi-variable identification algorithms (BDT and LLH) have also been studied and shown a higher efficiency and larger background rejection.

The analysis of $W \to \tau\nu \to \tau_{had}\nu$ has been performed and a preliminary cross section has been extracted. Track-based missing transverse momentum (p_T^{miss}) has been optimized and leading to QCD multi-jets background rejection of 60% with the requirement of $|\Delta\phi E_T^{miss}, p_T^{miss}| < 0.6$. The new defined E_T^{miss} significance has been used to estimate remnant QCD multi-jets background in the observed events and has proved to be less dependent on high pile up events. The total number of estimated signal events is 1545 ± 76 (statistical error only) while the estimated QCD multi-jets background is 642 ± 45 (statistical error only). Using the data collected in 2010 with integrated luminosity 36.8 pb^{-1}, a preliminary cross section has been estimated to 5.96 ± 0.26 nb with statistical uncertainty only.

In the $W \to \tau\nu$ events or processes related to τ lepton in the final states where τ decay hadorniacally, the possibly produced neutral particles (π^0 mainly) can not be reconstructed to p_T^{miss}. This would smear the correlation between p_T^{miss} and E_T^{miss}. To avoid or reduce the smearing effects, correction on reconstructed π^0 candidates in the τ_{had} is needed. Also, the p_T^{miss} can be reconstructed vertex by vertex, therefore the pile up effects on p_T^{miss} is small comparing to E_T^{miss}.

The pile up issue would take a major role for almost all the physics analysis in 2011 as the LHC will increase the instantaneous luminosity. Therefore new defined E_T^{miss} significance and related ideas will be very useful. To reduce the pile up effects the tracks p_T is required to be at least 1 GeV, this is not the best choice since it requires a kinematic cut. To improve the case, all the reconstructed tracks will be used but with tighter impact parameter (z_0) requirements to make sure the tracks are from a certain vertex.

The year 2011 is expected to be the Higgs boson year. The delivered data should be enough to exclude or give enough evidence of the significance over a large mass range. Besides, due to rare backgrounds for particles predicted in the Supersymmetry and exotic models, exciting results could be obtained as well. τ is important for Higgs in the low mass region ($<$ 140 GeV) and new particles search, which is not the case in electrons and muons. Therefore, τ would take a more important role in the next years. $W \to \tau_{had}\nu$ process need to be measured precisely again for the purpose of understanding τ_{had} performance at ATLAS and the background for the new phenomena. With the knowledge related to τ lepton and detector of ATLAS, search for Higgs boson with the final state as $\tau^+\tau^-$ will be implemented.

Bibliography

[1] PDG work group **The PDG live page** *http://pdglive.lbl.gov/Rsummary.brl?nodein=S035&exp=Y&sub=Yr&return=S003,S004,S0* 2, 59

[2] ATLAS Collaboration: G. Aad, et al., **The ATLAS Experiment at the CERN Large Hadron Collider**, *J. Instrum.*, 3 (2008) S08003. 2, 14, 17

[3] 'LHC white book', **LHC Conceptual Design Report**, *CERN-ARCH-LHC-3-089; CERN-AC-93-03*, 1993. 2, 17

[4] Bruning, Oliver Sim; Collier, Paul; Lebrun, P; Myers, Stephen; Ostojic, Ranko; Poole, John; Proudlock, Paul (editors), **LHC Design Report**, *CERN-2004-003-v1*, 2004. 2

[5] Radoslaw Ofierzynski, **W boson mass and properties at LEP**, *Journal of Physics: Conference Series 110 (2008) 042019, doi:10.1088/1742-6596/110/4/042019*. 2

[6] P. Roudeau, **Charm, Beauty and Tau Physics at LEP**, *http://delphiwww.cern.ch/talks/general/Roudeau.varenna1997/proceedings.ps.gz*, 1997. 2

[7] John Ellison, **W BOSON PHYSICS AT THE FERMILAB TEVATRON**, *Fermilab-Pub-97/079-E, D0-Conf-97-6, UCR/D0/97-07, http://arxiv.org/pdf/hep-ex/9704001v1*, 2008. 2

[8] Stephen Levy (on behalf of the CDF and D0 collaborations), **Tau Identification at the Tevatron**, *Springer Proceedings in Physics, 2006, Volume 108, Part 4, 102-106, DOI: 10.1007/978-3-540-32841-4_20*. 2

[9] Henry Semat, John R. **Introduction to atomic and nuclear physics**. newblock *Chapman and Hall. ISBN 0-412-15670-9. Albright (1984)*. 9

[10] M. Carena, S. Heinemeyer, C.E.M. Wagner and G. Weiglein, **MSSM Higgs Boson Searches at the Tevetron and the LHC: Impact of Different Benchmark Scenarios**, *ANL-HEP-PR-05-109 DCPT/05/128 FERMILAB-Pub-05-370-T, CERN-PH-TH/2005-158 EFI-05-19 IPPP/05/64, http://arxiv.org/pdf/hep-ph/0511023v1*, 2005. 12

[11] ALEPH, DELPHI, L3 and OPAL Collaborations, The LEP Working Group for Higgs Boson Searches, **Search for Neutral MSSM Higgs Bosons at LEP**, *PhD thesis*, 2010. 12

[12] Wan-Ching Yang, **Search for MSSM Higgs Bosons in Tau Final States with the D0 Detector**, *CERN-PH-EP/2006-001*, 17 January 2006. 12

[13] S. Heinemeyer, W. Hollik and G. Weiglein, **Constraints on** $tan(\beta)$ **in the MSSM from the Upper Bound on the Mass of the Lightest Higgs boson**, *DESY 99-120, KA-TP-12-1999, http://arxiv.org/abs/hep-ph/9909540*, 1999. 12

[14] Marcela Carena, Howard E. Haber, Heather E. Logan and Stephen Mrenna, **Distinguishing a MSSM Higgs Boson from the SM Higgs Boson at a Linear Collider**, FERMILAB-Pub-00/334-T SCIPP-01/25 UCD-01-23, http://arxiv.org/pdf/hep-ph/0106116v3, 2000. 12

[15] J. Smith, W. L. van Neerven, and J. A. M. Vermaseren, **Transverse Mass and Width of the W Boson**, Physical Review Letters, Volume 50, Number 22, 30 May 1983. 13

[16] Bruno Lenzi on behalf of ATLAS and CMS collaborations, **MSSM Higgs searches at the LHC**, *MCTP Spring Symposium on Higgs Boson Physics*, May 14, 2010. 12

[17] The ATLAS Collaboration, G. Aad et al., **Measurement of the** $W \to l\nu$ **production cross-section and observation of** $Z \to ll$ **production in proton-proton collisions at** $\sqrt{s}$ = **7TeV with the ATLAS detector**, *ATLAS conference note: ATLAS-CONF-2010-051*, 2010. 14, 126

[18] Alexei N. Safonov and CDF collaboration, **Physics with Taus at CDF**, *Nuclear Physics B, Volume 144*, July, 2005. 3

[19] Michel Davier, **LEPTON UNIVERSALITY**, *PhD thesis*, 1997. 3

[20] NA48 Collaboration, V. Fanti, **A new measurement of direct CP violation in two pion decays of the neutral kaon**, *Physics Letters B, Volume 465, Issues 1-4, pages 335-348*, 21 October 1999. 3, 4

[21] The Super-Kamiokande Collaboration, **Measurement of a small atmospheric ν_μ/ν_e ratio**, *Phys. Lett. B433 (1998), http://arXiv.org/pdf/hep-ex/9803006*, 1998. 3, 4, 12

[22] Yuichi Oyama, for K2K collaboration, **K2K (KEK to Kamioka) neutrino-oscillation experiment at KEK-PS**, *, http://arxiv.org/pdf/hep-ex/9803014, Talk at the YITP workshop on flavor physics, Kyoto, January 28-30*, 1998. 12

[23] D.P. Roy, **Basic Constituents of Matter and their Interactions A Progress Report**, *TIFR/TH/99-59, http://arxiv.org/pdf/hep-ph/9912523v1*, 28 December 1999. 4

[24] Joseph Hucks, **Global structure of the standard model, anomalies, and charge quantization**, *Phys. Rev. D 43, 2709-2717*, 1991. 9

[25] J. R. Christman, **THE STRONG INTERACTION**, *MISN-0-280*,2001. 8

[26] G. S. Guralnik, C. R. Hagen and T. W. B. Kibble, **Global Conservation Laws and Massless Particles**, *Phys. Rev. Lett. 13, 585-587*, 1964. 8

[27] Peter W. Higgs, **Broken Symmetries and the Masses of Gauge Bosons**, *Phys. Rev. Lett. 13, 508-509*, 1964. 8

[28] F. Englert and R. Brout, **Broken Symmetry and the Mass of Gauge Vector Mesons**, *Phys. Rev. Lett. 13, 321-323*, 1964. 8

[29] R. Brout and F. Englert, **Spontaneous Symmetry Breaking in Gauge Theories: a Historical Survey**, *ULB-TH-98/03, http://arxiv.org/pdf/hep-th/9802142v2*, 1998. 8

[30] GERALD S. GURALNIK, **THE HISTORY OF THE GURALNIK, HAGEN AND KIBBLE DEVELOPMENT OF THE THEORY OF SPONTANEOUS SYMMETRY BREAKING AND GAUGE PARTICLES**, *International Journal of Modern Physics A (IJMPA)*, Volume: 24, Issue: 14(2009) pp. 2601-2627. 8

[31] D0 collaboration, V.M. Abazov, **Search for Neutral Higgs Bosons Decaying to Tau Pairs in pp Collisions at s = 1.96 TeV**, *Fermilab-Pub-06/092-E, http://arxiv.org/pdf/hep-ex/0605009v2*, 21 December 2006. 14

[32] ATLAS Collaboration, **ATLAS detector and physics performance : Technical Design Report, Volume I and Volume II**, *ATLAS-TDR-014; CERN-LHCC-99-014*, 1999. 14, 19, 29, 35, 44

[33] ATLAS Collaboration: G. Aad, et al., **Expected Performance of the ATLAS Experiment: Detector, Trigger and Physics**, *arXiv:0901.0512*, 2008. 59, 62, 63, 68, 71

[34] CMS Collaboration, **CMS Technical Design Report**, *CERN-LHCC-2006-001 ; CMS-TDR-008-1*, 2006. 17

[35] ALICE Collaboration, **ALICE - Technical Design Reports**, *CERN/LHCC 2001-021*, 2001. 17

[36] LHCb Collaboration., **LHCb - Technical proposal**, *CERN-LHCC-98-004*, Feb 20 1998. 17

[37] LHCf Collaboration, **LHCf - Measrument of Photons and Neutral Pions in the Very Forward Region of LHC**, *CERN-LHCC-2006-004*, 7 February 2006. 17

[38] TOTEM Collaboration, **TOTEM - Total Cross Section, Elastic Scattering and Diffraction Dissociation at the Large Hadron Collider at CERN**, *CERN/LHCC 2004-002*, 7 January 2004. 17

[39] ATLAS Collaboration, **Inner Detector Technical Design Report, Volume 1**, *CERN/LHCC/97-16*, 30 April 1997. 19

[40] ATLAS Collaboration, **Inner Detector Technical Design Report, Volume 2**, *CERN/LHCC/97-17*, 30 April 1997. 24, 26

[41] ATLAS Collaboration, **Pixel Detector Technical Design Report**, *CERN/LHCC/98-13*, 31 May 1998. 22

[42] The ATLAS TRT collaboration: E. Abt et al., **The ATLAS TRT Barrel Detector**, *JINST 3 P02014*, 2008. 26

[43] ATLAS Collaboration, **Conceptual Design Report of ATLAS Solenoid**, *TECH-No-020*, 15 August 1996. 26

[44] M Aleksa, F Bergsma, L Chevalier, P-A Ciudici, J C Hart, A Kehrli, M Losasso, P S Miyagawa, X Pons, H Sandaker and S W Snow, **Results of the ATLAS solenoid magnetic field map**, *2008 J. Phys.* , Conf. Ser. 110 092018. 26

[45] ATLAS Collaboration, **Calorimeter Performance Technical Design Report**, *CERN/LHCC/96-40*, 15 December 1996. 26

[46] P. Puzo, **ATLAS Calorimetry**, *Nuclear Instruments and Methods in Physics Research A*, 494 (2002) 340-345. 19

[47] ATLAS Collaboration, **Liquid Argon Calorimeter Technical Design Report**, *CERN/LHCC/96-41*, 15 December 1996. 28, 33, 35

[48] Gaston Parrour, Pierre Petroff, Laurent Serin and Vincent Tisserand, **Performance of the ATLAS electromagnetic calorimeter filled with liquid Krypton: Higgs mass resolution in the $H^0 \to \gamma\gamma$ and $H^0 \to ZZ^* \to 4e^{\pm}$**, *ATLAS Internal Note, CAL-NO-077*, 5 October 1995.

[49] John S. White, **Spatial Reconstruction of ELectrons with an Accordion Geometry Electromagnetic Calorimeter**, *PhD thesis*, 1993. 29

[50] M. Aleksa et al., **ATLAS combined testbeam: Computation and validation of the electronic calibration constants for the electromagnetic calorimeter**, *Tech. Rep. ATL-LARG-PUB-2006-003, CERN, Geneva (Switzerland)*, Apr 2006. 44

[51] The ATLAS collaboration: Z. Meng on behalf of the ATLAS Liquid Argon Calorimeter Group, **Performance of the ATLAS Liquid Argon Calorimeter**, *ATL-LARG-PROC-2010-017* Conference of Physics at LHC, 2010. 43, 46

[52] The ATLAS Collaboration: G. Aad et al., newblock **Readiness of the ATLAS Liquid Argon Calorimeter for LHC Collisions**, *Eur. Phys. J. C* 2010 70: 723-753. 31, 43, 46

[53] The ATLAS Collaboration: G. Aad et al., newblock **Drift Time Measurement in the ATLAS Liquid Argon Electromagnetic Calorimeter using Cosmic Muons**, *EPJC* 2010. 29, 42

[54] The ATLAS collaboration: Z. Meng on behalf of the ATLAS Liquid Argon Calorimeter Group, **Performance of the ATLAS Liquid Argon Calorimeter**, *ATL-LARG-SLIDE-2010-118* Conference of Physics at LHC, 2010. 46

[55] RD–34 collaboration: E. Berger, et al., **Construction and Performance of an Iron–Scintillator Hadron Calorimeter with Longitudinal Tile Configuration**, *CERN/LHCC 95-44*, 16 August 1995. 33

[56] J.A. Budagov, Y.A. Kulchitsky, M.V. Kuzmin, V.B. Vinogradov, **The e/h ratio of the ATLAS Hadronic Tile Calorimeter**, *hep-ex/0104046*, 27 Jan 1999. 44

[57] Y.A. Kulchitsky, V.B. Vinogradov, **Non-Compensation of the ATLAS Barrel Tile Hadron Module-0 Calorimeter**, 09 Jul 2009. *ATL-TILECAL-99-002*. 44

[58] Julian Budagov and Jemal Khubua, **ATLAS Hadron Tile Calorimeter: Modules Development and Mass Production Experience**, *BULLETIN OF THE GEORGIAN NATIONAL ACADEMY OF SCIENCES, vol. 175, no. 4, 2007*. 44

[59] V. Guarino, N. Hill, E. Petereit, F. Skrzecz, K. Wood, J. Proudfoot, S. Anderson, A. Caird, F. Franchini, C. Keyser, L. Kocenko, Z. Matijas, T. Nephew, R. Stanek, **Production Summary for Extended Barrel Module Fabrication at Argonne for the ATLAS Tile Calorimeter**, *ANL-HEP-TR-07-68*, October 207. 33

[60] ATLAS Collaboration: G. Ada, et al., **Readiness of the ATLAS Tile Calorimeter for LHC collisions**, *The European Physics Journal C*, (2010) 70: 1193-1236, DOI 10.1140/epjc/s10052-010-1508-y. 33

[61] ATLAS Collaboration, **Trigger performance, in ATLAS Detecotr and Physics Performance Technical Design Report**, *pp. 347-400. CERN/LHCC/99-14/15, CERN, Geneva*, 1999. 37

[62] The ROOT team, **An Object Oriented Data Analysis Framework**, *Paper presented at the AIHENP conference in Laussanne*, 1996. 37

[63] The ATLAS Collaboration: E. Abat, et al., **Response and shower Topology of 2 to 180 GeV Pions measure with the ATLAS Barrel Calorimeter at the CERN Test-beam and Comparison to Monte Carlo Simulations**, *ATL-CAL-PUB-2010-001*, 2010. 40, 42, 43, 44, 67

[64] The ATLAS Collaboration: E. Abat, et al., **Study of the response of the ATLAS central calorimeter to pions of energies from 3 to 9 GeV**, *Nuclear Instruments and Methods in Physics Research A*, 607 (2009) 372-386. 40, 46

[65] The ATLAS Collaboration: E. Abat, et al., **Measurement of the response of the ATLAS liquid argon barrel calorimeter to electrons at the 2004 combined test-beam**, *Nuclear Instruments and Methods in Physics Research A*, 614 (2010) 400-432.

[66] The ATLAS Collaboration: M. Aleksa, M. Delmastro, M. Fanti, R. Lafaye, W. Lampl, S. Laplace, D. Prieur, F. Tarrade, I. Wingerter-Seez, **2004 ATLAS Combined Testbeam: Computation and Validation of the Electronic Calibration Constants for the Electromagnetic Calorimeter**, *ATL-LARG-PUB-2006-003*, 2006. 43

[67] ATLAS Collaboration: Bechtle. P, Brunet. S, Czyczula. Z, Dingfelder. J, Hellgartner. D, Janus. M, Klupp. S, Kroseberg. J, Mazini. R, Meng. Z, O'Neil. D, Saavedra. A, Schwindt. T, Tsuno. S, Uhlenbrock. M, Wang. T, **Commissioning of the ATLAS Tau-Lepton Reconstruction Using 900 GeV Minimum-Bias Data**, *ATLAS-CONF-2010-012*, 2010. 68, 70

[68] ATLAS Collaboration: Bechtle. P, Coadou. Y, Czyczula. Z, Dam. M, Dell'Asta. L, Godfrey. J, Gosdzik. B, Griffiths. J, Janus. M, Kaczmarska. A, Kroseberg. J, Kuehn. S, Lai. S, Mazini. R, Meng. Z, Nakamura. K, Nunes Hanninger. G, O'Neil. DC, Reece. R, Rosati. S, Tsuno. S, Vickey. T, Wang. T, **Commissioning of hadronic tau candidates in QCD events at**

ATLAS with 7 TeV proton-proton collisions, *ATLAS-CONF-2010-059*, 2010. 70

[69] S. Lai on behalf of the ATLAS Collaboration, **Tau physics at the LHC with ATLAS**, *arXiv:0910.4727v1*, 25 October 2009. 80

[70] The ATLAS Collaboration: Bechtle. P, et al., **Tau Reconstruction and Identification Performance in ATLAS**, *ATLAS-CONF-2010-086*, 2010. 86

[71] The ATLAS Collaboration: Bechtle. P, et al., **Observation of $W \to \tau\nu_\tau$ Decays with the ATLAS Experiment**, *ATLAS-CONF-2010-097*, 2010. 91, 105, 117

[72] The ATLAS Collaboration, **Performance of the missing transverse energy reconstruction in minimum bias events at $\sqrt{s}$ of 900 GeV and 2.36 TeV with the ATLAS detector**, *ATLAS-CONF-2010-008*, 2010. 89

[73] The ATLAS Collaboration, **Performance of the missing transverse energy reconstruction in proton-proton collisions at center-of-mass energy of $\sqrt{s}$ = 7 TeV with the ATLAS detector**, *ATLAS-CONF-2010-039*, 2010. 89

[74] The ATLAS Collaboration, **Performance of the Missing Transverse Energy Reconstruction and Calibration in Proton-Proton Collisions at a Center-of-Mass Energy of 7 TeV with the ATLAS Detector**, *ATLAS-CONF-2010-057*, 2010. 89

[75] Michel Janus, **Tau Reconstruction at ATLAS**, *KIP Journal Club Heidelberg*, Wednesday 6th of May 2009. 80

[76] The ATLAS Collaboration, **Measurement of the missing transverse momentum based on tracks in proton-proton collisions at $sqrts =$ 900 GeV centre-of-mass energy with the ATLAS detector**, *ATLAS-CONF-2010-020*, 2010. 91, 105

[77] The ATLAS Collaboration, **Data-Quality Requirements and Event Cleaning for Jets and Missing Transverse Energy Reconstruction with the ATLAS Detector in Proton-Proton Collisions at a Center-of-Mass Energy of $sqrts =$ 7 TeV**, *ATLAS-CONF-2010-038*, 2010. 104

[78] Brigid Blakeslee, Cristobal Cuenca Almenar, Sarah Demers, Soshi Tsuno, **Tau Data Quality GRL for ICHEP 2010**, *ATL-COM-PHYS-2010-405*, 2010. 99, 127

[79] T. Sjoestrand, S. Mrenna and P. Skands, **PYTHIA 6.4 physics and manual**, *JHEP 05 (2006) 026*. 93

[80] A. Agostinelli et al., **GEANT4: A simulation toolkit**, *Nucl. Inst. Meth. A506 (2003) 250*. 93

[81] C. Anastasiou and L. Dixon and K. Melnikov and F. Petriello, **High-precision QCD at hadron colliders: electroweak gauge boson rapidity distributions at NNLO**, *Phys. Rev. D69 (2004) 094008*. 93

[82] A. D. Martin, W. J. Stirling, R. S. Thorne, and G. Watt, **Parton distributions for the LHC**, *Eur. Phys. J. C63 (2009) 189*. 93

[83] M. Bellomo, A. Belloni, E. Berglund, J.B. Blanchard, J. Ferrando, D. Fournier, J. Guimaraes da Costa, C. Issever, M. Kagan, A. Kapliy, K. Kessoku, T. Kishimoto, J. Kretzschmar, T. Kubota, K. Lohwasser, V. Martinez Outschoorn, T. Matsushita, T. Nishiyama, P. Onyisi, E. Petit, S. Prasad, M. Schott, M. Shochet, H. Skottowe, Y. Suzuki, S. Whitehead, **Measurement of $W \to l\nu$ charge asymmetry in proton-proton collisions at $\sqrt{s} =$ 7 TeV with the ATLAS detector**, *ATLAS Note draft v1.0*, 10 Dec 2010. 95

[84] The ATLAS Collaboration, **Performance of the Missing Transverse Energy Reconstruction and Calibration in W and Z events in ATLAS Proton-Proton Collisions at $\sqrt{s}$ =7 TeV**, *ATLAS-COM-CONF-2011-035*, 2011. 101, 109

[85] J. Garvey et al., **Use of an FPGA to identify electromagnetic clusters and isolated hadrons in the ATLAS level-1 calorimeter trigger**, *Nucl. Inst. Meth. A512 (2003) 506516*. 98

[86] B. Blakeslee, C. Cuenca Almenar, S. Demers, and S. Tsuno, **Tau Data Quality Good Run Lists for ICHEP 2010, Tech. Rep.**, *ATL-COM-PHYS-2010-405, CERN, Geneva*, Jun, 2010. 99, 127

[87] A.D. Martin, W.J. Stirling, R.S. Thorne and G. Watt, **Parton distributions for the LHC**, *IPPP/08/95, DCPT/08/190, Cavendish-HEP-08/16*, 11 June 2009. 99, 127

[88] The D0 Collaboration, **Measurement of t$\bar{t}$ Production Cross Section in the Lepton + Tau + b-jet(s) + E_T^{miss} Channel Using 1.2 fb^{-1} of Run IIb Data** *D0 note 5607-CONF, URL: http://www-d0.fnal.gov*, July 9, 2008. 122

[89] The ATLAS Collaboration, **Luminosity Determination in pp Collisions at sqrt(s)=7 TeV Using the ATLAS Detector at the LHC**, *arXiv:1101.2185 [hep-ex]*, 2011. 128

[90] E. Coniavitis, M. Dam, E.N. Dawe, S. Dhaliwal, M. Flechl, M. Janus, A. Kaczmarska, S. Lai, K. Nakamura, D.C. ONeil, R. Reece, S. Rosati, F. Seifert1, M. Trottier-McDonald, S. Tsuno, H.H. Williams, on behalf of the Tau Combined Performance Group, **Reconstruction, Energy Calibration, and Identification of Hadronic Tau Decays for Winter 2011** *ATL-COM-PHYS-2011-217*, 2011 128

Acknowledgements

First and most important, I would like to acknowledge, very much, to Prof. Zhang Xueyao and Prof. Lee Shih-Chang. They are my supervisor in Shandong University and CERN. Their useful guidance and supervisions on my work make me go onto higher and higher level of the research abilities. Prof. Zhang taught me how to take a correct attitude on studies. He taught me the basic but essential courses related to the high energy researches. His supervisions throughout my PhD periods benefit all my life. He provides me the opportunity of learning at CERN where I gained many useful and important experiences in my life. He provides me the opportunity that I met Prof. Lee, with proud. During studies at CERN, Prof. Lee supervised me the researches with strict demands. His serious attitude expresses me and teaches me how to treat the researches even on a likely trial detail. He suggested the tau related topic for the PhD thesis. Through the studies on tau, I learned very much both for the researches and the collaborating skills with other people.

I would like to acknowledge Prof. Feng Cunfeng, who actually introduced me the first time of how high energy experiments work by assigning me a job about the ARGO cosmic ray experiment before I came to CERN. I would like to acknowledge him, that he pushed me and give me the opportunity learning at CERN.

I would like to acknowledge Prof. Ren Zhongliang for his help in my common life and supervisions at CERN on the work.

I would like to acknowledge Prof. Claudio Santoni, he supervised me for the test beam analysis and I learned very much about the basic analysis skills and analysis methods from him.

I would like to acknowledge Rachid Mazini. During the collaboration with him about the tau performance and W to taunu cross section measurement, His detailed supervisions on the analysis make me learn very much from him. His encouragements in the analysis works make me have confidence that was lost in the first years coming to CERN.

I would like to acknowledge Song-Ming Wang who owns the very nice personality, spread knowledge and conscientious work let me find myself's drawbacks. His many helps in my work let me learned many things about how to analyze data.

I would like to acknowledge Stefania Xella and Mansoora Shamin who are the conveners of the tau trigger groups and provide me many help on the tau trigger study. Especially to Stefania Xella who agrees to write letters of reference for me.

I would like to acknowledge Jiahang Zhong, Ashfaq Ahamad and Jike Wang who are my officemates at CERN. Thanks to Jiahang who discusses with me on the work and shares information on everything. Thanks to Ashfaq and Jike for the discussions on the work and chats about everything. Thanks to you all make our office the best both on the work environment and concerning of each other.

I would like to acknowledge Suijian Zhou, Dong Liu, Daxian Su, Zhili Weng, Zhijun Liang and Horng-Liang Shih who are sitting in the opposite door of my office. Thank you all for the discussions and helps of works.

I would like to acknowledge my friends who are not my colleagues, Zhou Ning, Guo Jun, Deng Jianrong, Zhu Jianlin, Huang Jin, Wang Hulin, Zhang Dongliang, Xie Si, Yang Yong, Li Zhe, Zhou Yue, Zhang Jinghui, Fan Guiju and Cheng Jie. Thank you all for playing with me in the weekends or holidays and more important on the help of everything both on work and common life.

I would like to acknowledge the collaborators Stan Lai, Soshi Tsuno, Yann Caodou, Juergen Kroseberg, Jana Kraus, Lidia Dell'Asta, Sebastian Johnert, Noel Dawe, Attilio Andreazza, Cigdem Isserver, Todd Hoffman, Alexandre Gerardin and Tancredi Carli.

At last, I would like to acknowledge my parents who have been supporting me selflessly without complaining the difficulties they met for my study from primary school to the highest level of degree in China. I would like to acknowledge my husband, Wei Wei, who always comforts me when I met dilemmas and gives me confidence when I loose the courage to face difficulties both in the common life and work.

I would like to acknowledge every one helps me at CERN and my friends made before I came to CERN.

Thank you all for everything !

8

List of published papers

1. Performance of the ATLAS Liquid Argon Calorimeter. Poster presented on physics at LHC 2010 (pLHC 2010), Jun. 12 2010 - Jun 17 2010, ATL-LARG-PROC-2010-017, DESY-PROC-2010-01, Dec 2010. 3pp. Published in *Hamburg 2010, Physics at the LHC 2010* 406-408.

2. Study of the response of the ATLAS central calorimeter to pions of energies from 3 to 9GeV. Nuclear Instruments and Methods in Physics Research A 607 (2009) 372386.

3. The versatile link, a common project for super-LHC. Journal of Instrumentation, 2009 4 P12003. L.

4. Commissioning of the ATLAS TauLepton Reconstruction Using 900 GeV MinimumBias Data. ATLAS-CONF-2010-012, March 16 2010.

5. Reconstruction of hadronic tau candidates in QCD events at ATLAS with 7 TeV proton-proton collisions. ATLAS-CONF-2010-059, 10 July 2010.

6. Response and Shower Topology of 2 to 180 GeV Pions Measured with the ATLAS Barrel Calorimeter at the CERN Testbeam and Comparison to Monte Carlo Simulations. ATL-CAL-PUB-2010-001, 6 May 2010.

7. Measurement of the response of the ATLAS liquid argon barrel calorimeter to electrons at the 2004 combined test-beam. Nuclear Instruments and Methods in Physics Research A 614 (2010) 400432.

8. A Layer Correlation technique for pion energy calibration at the 2004 ATLAS Combined Beam Test. ATL-COM-CAL-2010-006, Dec 2010.

9. Combined performance studies for electrons at the 2004 ATLAS combined test-beam. Journal of Instrumentation, 2010 5: P11006.

10. Study of energy response and resolution of the ATLAS barrel calorimeter to hadrons of energies from 20-GeV to 350-GeV. Nucl. Instrum. Meth. A 621:134-150,2010.

11. Measurement of the W$\rightarrow$ $l\nu$ and Z/gamma $\rightarrow$ ll production cross sections in proton-proton collisions at sqrt(s) = 7 TeV with the ATLAS detector. JHEP 1012:060,2010

12. Luminosity Determination in pp Collisions at sqrt(s)=7 TeV Using the ATLAS Detector at the LHC. arXiv:1101.2185 [hep-ex].

13. Study of Jet Shapes in Inclusive Jet Production in pp Collisions at sqrt(s) = 7 TeV using the ATLAS Detector. CERN-PH-EP-2010-077, Jan 2011.

14. Measurement of the centrality dependence of J/ψ yields and observation of Z production in lead-lead collisions with the ATLAS detector at the LHC. Phys.Lett.B 697:294-312,2011.

15. Measurement of the production cross section for W-bosons in association with jets in pp collisions at sqrt(s) = 7 TeV with the ATLAS detector. CERN-PH-EP-2010-081, Dec 2010. Submitted to Phys.Lett.B.

16. Measurement of the inclusive isolated prompt photon cross section in pp collisions at sqrt(s) = 7 TeV with the ATLAS detector. arXiv:1012.4389 [hep-ex].

17. Measurement of the top quark-pair production cross section with ATLAS in pp collisions at $\sqrt{s}$ = 7 TeV. arXiv:1012.1792 [hep-ex].

18. Measurement of underlying event characteristics using charged particles in pp collisions at $\sqrt{s} = 900$ GeV and 7 TeV with the ATLAS detector. arXiv:1012.0791 [hep-ex].

19. Observation of a Centrality-Dependent Dijet Asymmetry in Lead-Lead Collisions at sqrt(S(NN))= 2.76 TeV with the ATLAS Detector at the LHC. Phys.Rev.Lett. 105:252303,2010.

20. Measurement of inclusive jet and dijet cross sections in proton-proton collisions at 7 TeV centre-of-mass energy with the ATLAS detector. Eur.Phys.J.C71:1512,2011.

21. Search for New Particles in Two-Jet Final States in 7 TeV Proton-Proton Collisions with the ATLAS Detector at the LHC. Phys.Rev.Lett.105:161801,2010.

22. Readiness of the ATLAS Tile Calorimeter for LHC collisions. Eur.Phys.J.C70: 1193-1236, 2010.

23. Commissioning of the ATLAS Muon Spectrometer with Cosmic Rays. Eur.Phys.J.C70:875-916,2010.

24. Performance of the ATLAS Detector using First Collision Data. JHEP 1009:056,2010.

25. The ATLAS Simulation Infrastructure. Eur.Phys.J.C70:823-874,2010.

26. The ATLAS Inner Detector commissioning and calibration. Eur.Phys.J.C70:787-821,2010.

27. Charged-particle multiplicities in pp interactions at sqrt(s) = 900 GeV measured with the ATLAS detector at the LHC. Phys.Lett.B688: 21-42,2010.

28. Drift Time Measurement in the ATLAS Liquid Argon Electromagnetic Calorimeter using Cosmic Muons. Eur.Phys.J.C70:755-785,2010.

29. Readiness of the ATLAS Liquid Argon Calorimeter for LHC Collisions. Eur.Phys.J.C70: 723-753,2010.

Declaration

I herewith declare that I have produced this paper without the prohibited assistance of third parties and without making use of aids other than those specified; notions taken over directly or indirectly from other sources have been identified as such. This paper has not previously been presented in identical or similar form to any other Chinese or foreign examination board.

The thesis work was conducted from June 2007 to June 2011 under the supervision of Prof. Zhang Xueyao at Shandong University and Prof. Lee Shih-Chang at Academia Sinica.

Jinan, Shandong, P. R. China.